GAS-GRAIN CHEMICAL MODELS: INCLUSION OF A GRAIN SIZE DISTRIBUTION AND A STUDY OF YOUNG STELLAR OBJECTS IN THE MAGELLANIC CLOUDS

A Dissertation

Presented to the Faculty of the Graduate School

of Cornell University

in Partial Fulfillment of the Requirements for the Degree of

Doctor of Philosophy

by

Tyler Andrew Pauly

December 2017

GAS-GRAIN CHEMICAL MODELS: INCLUSION OF A GRAIN SIZE DISTRIBUTION AND A STUDY OF YOUNG STELLAR OBJECTS IN THE MAGELLANIC CLOUDS

Tyler Andrew Pauly, Ph.D.

Cornell University 2017

Computational models of interstellar gas-grain chemistry have aided in our understanding of star-forming regions. Chemical kinetics models rely on a network of chemical reactions and a set of physical conditions in which atomic and molecular species are allowed to form and react. We replace the canonical single grain-size in our chemical model MAGICKAL with a grain size distribution and analyze the effects on the chemical composition of the gas and grain surface in quiescent and collapsing dark cloud models. We find that a grain size distribution coupled with a temperature distribution across grain sizes can significantly affect the bulk ice composition when dust temperatures fall near critical values related to the surface binding energies of common interstellar chemical species.

We then apply the updated model to a study of ice formation in the cold envelopes surrounding massive young stellar objects in the Magellanic Clouds. The Magellanic Clouds are local satellite galaxies of the Milky Way, and they provide nearby environments to study star formation at low metallicity. We expand the model calculation of dust temperature to include a treatment for increased interstellar radiation field intensity; we vary the radiation field to model the elevated dust temperatures observed in the Magellanic Clouds. We also adjust the initial elemental abundances used in the model, guided by observations of Magellanic Cloud HII regions. We are able to reproduce the relative ice frac-

tions observed, indicating that metal depletion and elevated grain temperature are important drivers of the envelope ice composition. The observed shortfall in CO in Small Magellanic Cloud sources can be explained by a combination of reduced carbon abundance and increased grain temperatures. The models indicate that a large variation in radiation field strength is required to match the range of observed LMC abundances. CH_3OH abundance is found to be enhanced (relative to total carbon abundance) in low-metallicity models, providing seed material for complex organic molecule formation.

We conclude with a preliminary study of the recently discovered hot core in the Large Magellanic Cloud; we create a grid of models to simulate hot core formation in Magellanic Cloud environments, comparing them to models and observations of well-characterized galactic counterparts.

BIOGRAPHICAL SKETCH

Tyler was born in Indiana and grew up in Iowa, first in Des Moines but moving to rural Winterset at age eight. He spent his formative years on his family's farm, with two of his grandparents living next door. When not at school, he could often be found fishing the farm pond or playing with his younger sister Erin.

Tyler loved school from day one, particularly math, science and reading. He credits a series of great teachers for keeping him engaged, especially when he would have rather just read his book. He enjoyed extracurriculars in high school, participating in soccer, concert and jazz band (as a trumpet player), and starting the engineering club.

Tyler went on to study chemical engineering at Iowa State University; he changed majors in his sophomore year after a visit to the job fair left him lacking enthusiasm for the career paths on offer. He switched focus to physics, adding a minor in astronomy after a particularly enjoyable course taught by Professor Lee Anne Willson. In the summer following his junior year he visited Cornell University as an REU student (Research Experiences for Undergraduates), where he worked with his future graduate advisor, Dr. Robin Garrod, on the problem of CO_2 ice formation in dark clouds in the interstellar medium (ISM). The Cornell astronomy graduate admissions committee saw fit to allow this pairing to continue, and he began his graduate studies in the fall of 2011.

While at Cornell, Tyler worked primarily on computational models of chemical evolution in astronomical environments, typically cold and dense regions of the ISM. After Dr. Garrod accepted an assistant professorship at the University of Virginia, Tyler began additional projects on infrared observations of young stellar objects and evolved stars in the Magellanic Clouds with Dr. Gregory

Sloan. Through this work, he gained valuable experience in data reduction and analysis methods of infrared spectra. These projects merged to form the body of this thesis, a chemical evolution study of young stellar objects in the Magellanic Clouds.

After completion of his doctoral work, Tyler looks forward to beginning work with Klaus Pontoppidan at the Space Telescope Science Institute on LIME, a 3D non-LTE radiative transfer code with applications for protoplanetary disks.

This dissertation is dedicated to my parents, my sister and my grandparents.

Without their guidance and support, I would not have made it this far.

ACKNOWLEDGEMENTS

- Rob – After our work during my time as an REU student, he took me on as his first graduate student. I'm glad I had the opportunity; despite some additional work created by the lack of a Cornell faculty appointment, Rob was always available to help when I was lost, either in a research problem or in FORTRAN code. Even through his transition to the University of Virginia and the addition of many new responsibilities, Rob remained communicative and supportive. If his patience was tested by my knack for mistyping model parameters, he never showed it.
- Greg (Sloan) – In addition to providing an endless source of lunch table discussion topics, Greg took me on for research work for fifteen months. He taught me how to analyze infrared spectroscopy and helped me develop a proper sense of data skepticism. I was able to investigate an exciting dataset on Magellanic cloud YSOs that prompted a good chunk of this work.
- Mike, Dan and Greg (Booth) – Through Dan and Mike, I was able to participate in a local Ithaca soccer league which kept me ambulatory through my otherwise desk-ridden graduate years. Greg also let me play with his team when my old team fell apart. I'm grateful to the Ithaca United Soccer Club for providing a competitive but friendly environment for the weekend warriors like me.
- Ryan and Mike – Besides soccer, I spent more time in graduate school than I should have on side projects, hobbies, and being generally unproductive. These activities were sometimes spurred by and often shared with these two, and they put up with my nonsense for five or six years.

- Ryan, Kassandra, Sam, Michelle, Paul and Maryame – This group formed a consistent weekly gathering at a local watering hole. Some weeks required additional gatherings, but letting out research frustration with them made the past few years more manageable.
- Larry, Dan, Jim, Will, Andy, Sam, Michelle, Paul, Curran – Beginning in my REU summer, this group got me into board games, starting with Vlaada Chvatil's classic *Through the Ages: A Story of Civilization*. Though my participation has varied significantly year-to-year, the weekly board game night provided yet another distraction that I credit with keeping my spirits high.
- Katy, Shanna and Maggie – I found this group of Cornell veterinary students through a chance friendship via a teaching assistantship, and their pets provided plenty of therapy and entertainment over the four years I've known them. I learned from them that I might prefer FORTRAN woes to bovine palpation.
- Jim, Becky, Greg, Carolyn, and Alfonso – This great group of people are all relatives of Mike, and they welcomed me into their home on many occasions to celebrate the Kentucky Derby and Guy Fawkes Day. I have many memories of belting out tunes to acoustic guitar next to their fire pit.

TABLE OF CONTENTS

LIST OF TABLES

LIST OF FIGURES

CHAPTER 1

INTRODUCTION

1.1 Overview of Astrochemistry

Astrochemistry is the study of chemical processes and species present throughout the diverse environments in the extraterrestrial universe. The field is quite interdisciplinary, including research on astronomical observations, laboratory experiments of chemical processes, and numerical modeling of chemical interactions and rate kinetics. In many astronomical environments, chemical processes are closely coupled to physical processes: diffuse and dense clouds in star-forming regions, molecular ejecta from aging stars, cometary nuclei and comae, and (exo-)planetary atmospheres. The interaction between chemical and physical processes creates astronomical "laboratories" where we are able to explore reactions at temperatures, densities and timescales not easily replicated on Earth.

Astrochemistry gained prominence in the late 1960s with the discovery of ammonia and water rotational emission lines towards the galactic center by Cheung et al. (1968), Cheung et al. (1969), and Cheung, Rank & Townes (1969). These transitions are found at radio wavelengths; the findings were made possible through advances in millimeter and centimeter telescope technologies, and construction of these telescopes opened a new observational window to the universe.

The next decade saw a multitude of new molecular detections through rotational line emission, mostly toward dense clouds of gas in interstellar and

circumstellar space. The rotational line spectrum holds a wealth of information on its source species: the amplitudes of its lines determine its abundance, line ratios constrain the molecule's temperature and density, and the line profiles can tell us of the local kinematics. With additional discoveries through ro-vibrational transitions in the infrared and electronic transitions in ultraviolet and visible wavelengths, the tally of confirmed molecules in the interstellar medium (ISM) has surpassed 200. Table 1.1 lists all detected interstellar and circumstellar molecules as of July 2017; many of the detected molecules are organic in nature and range from diatomic species up to 12 or more atoms, with some outliers such as the soot-like fullerenes C_{60} and C_{70}.

Molecules detected in the infrared via ro-vibrational transitions have been found both in emission and in absorption against a background source. Infrared absorption studies have been used to characterize species found in solid form towards dense and cold regions of the interstellar medium. Early infrared observations from the ground had low spectral resolution, with typical $\lambda/\Delta\lambda \sim 50 - 100$; however, this was sufficient for characterization of some prominent molecular absorption bands. Gillett & Forrest (1973) observed the Becklin-Neugebauer object with the UM/UCSD 60-inch infrared telescope atop Mount Lemmon, finding the first evidence of H_2O ice infrared absorption bands at 3.1 μm and confirming deep silicate absorption at 10 μm. Merrill, Russell & Soifer (1976) found a consistent absorption feature at 3.1 μm towards a heterogeneous sample of infrared sources associated with molecular clouds, and they attributed the absorption band to a mixture of H_2O and NH_3 ices.

The following generations of infrared space observatories provided more detailed observations of solid-state absorption in dense interstellar regions.

2 Atoms		3 Atoms		4 Atoms	5 Atoms	6-7 Atoms	8-9 Atoms
CH	CN	H_2O	HCO^+	NH_3	HC_3N	CH_3OH	$HCOOCH_3$
CH^+	OH	HCN	OCS	H_2CO	HCOOH	CH_3CN	CH_3C_3N
CO	H_2	HNC	H_2S	HNCO	CH_2NH	NH_2CHO	C_7H
SiO	CS	N_2H^+	C_2H	H_2CS	NH_2CN	CH_3SH	CH_3COOH
SO	SiS	SO_2	HCO	C_2H_2	H_2CCO	C_2H_4	CH_3COOH
NS	C_2	HNO	OCN^-	C_3N	C_4H	C_5H	H_2C_6
NO	HCl	HCS^+	HOC^+	HNCS	SiH_4	CH_3NC	CH_2OHCHO
NaCl	AlCl	c-SiC_2	MgNC	$HOCO^+$	c-C_3H_2	HC_2CHO	C_6H_2
KCl	AlF	C_2S	C_3	C_3O	CH_2CN	H_2CCCC	C_2H_5N
PN	SiC	CO_2	CH_2	C_3H	C_5	HC_3NH^+	CH_2CHCHO
CP	NH	C_2O	NH_2	$HCNH^+$	SiC_4	C_5N	CH_2CCHCN
SiN	SO^+	NaCN		H_3O^+	H_2CCC	C_4H_2	NH_2CH_2CN
CO^+		N_2O		C_3S	CH_4	HC_4N	CH_3CHNH
HF		MgCN		c-C_3H	HCCNC	c-H_2C_3O	$(NH_2)_2CO$
FeO		H_3^+		HC_2N	HNCCC	CH_2CNH	CH_3OCH_3
N_2		SiCN		H_2CN	H_2COH^+	C_5N^-	CH_3CH_2OH
CF^+		AlNC		SiC_3	C_4H^-	HNCHCN	CH_3CH_2
PO		SiNC		CH_3	CNCHO	C_5S	HC_7N
AlO		HCP		C_3N^-	HNCNH	SiH_3CN	CH_3C_4H
CN^-		CCP		PH_3	CH_3O	CH_3CHO	C_8H
OH^+		AlOH		HCNO	NH_3O^+	CH_3CCH	CH_3CONH_2
SH^+		H_2O^+		HOCN	H_2NCO^+	CH_3NH_2	C_8H^-
O_2		H_2Cl^+		HSCN	$HCCNH^+$	CH_2CHCN	CH_2CHCH_3
HCl^+		KCN		HOOH		HC_5N	CH_3CH_2SH
SH		FeCN		l-C_3H^+		C_6H	CH_3NHCHO
TiO		HO_2		HMgNC		c-C_2H_4O	
ArH^+		TiO_2		MgCCH		CH_2CHOH	
NO^+		CCN		NCCP		C_6N^-	
CrO		SiCSi		HCCO		CH_3NCHO	

10+ Atoms			
HC_9N	$(CH_3)_2CO$	n-C_3H_7CN	$HOCH_2CH_2OH$
CH_3C_6H	$C_{14}H_{10}^+$	iso-C_3H_7CN	CH_3CH_2CHO
C_{60}	C_6H_6	$C_2H_5OCH_3$	CH_3CHCH_2O
C_{60}^+	C_6H_5OH	CH_3C_5N	CH_3COOCH_3
C_{70}		C_2H_5OCHO	

Table 1.1: Detected molecules in the ISM. (ref. astrochymist.org)

D'Hendecourt & Jourdain de Muizon (1989) searched data from the low resolution slit-less spectrometer onboard the Infrared Astronomical Satellite (IRAS) and found the ν_2 absorption band of CO_2 ice at 15.2 μm. The Spitzer Space Telescope and the Akari satellite have provided even more detailed views of infrared absorption sources in the near- and mid-infrared, increasing the known ice species to H_2O, CO, CO_2, CH_4, NH_3, CH_3OH, OCS and "XCN" (a C≡N stretch possibly attributed to OCN^- Gibb et al. (2004).)

1.2 History of Astrochemical Models

The library of detected astronomical species is indicative of the chemical complexity present in the ISM. A complete picture of the formation of chemical complexity requires understanding the interplay between chemical and physical processes influencing the ISM via photon absorption and emission processes, ionization processes, and solid-phase material growth via gas depletion onto dust grains. To this end, numerical simulations are used to model the evolution of chemical abundances.

The rapid influx of new molecular detections in the early 1970s spurred many theoretical investigations into possible formation scenarios. Herbst & Klemperer (1973) constructed a model including over 100 gas-phase reactions for roughly 35 species in dense cloud environments where density is high, $n_H \sim 10^{4-6}$ cm^{-3}. This model assumed sufficient extinction was present such that the effects of the external radiation field are negligible, and the primary energetic input to drive ion-molecule reactions was provided by cosmic ray ionization. The model ignored condensation onto grains, and found a steady-state solution

was physical as long as cloud lifetimes were greater than $\approx 10^5$ years. The authors concluded in follow-up work that their model found a sufficient column of HCO^+ was present to match the strength of the unidentified line detected by Buhl & Snyder (1970) (Herbst & Klemperer, 1974).

Early models considering grain-surface chemistry were constructed to model the formation of molecular hydrogen (Gould & Salpeter, 1963; Hollenbach & Salpeter, 1971). The grain surface serves as a collection site for gas-phase species and as an energy sink to stabilize the energetic reaction products that may result from surface interaction of reactive adsorbates. Watson & Salpeter (1972) constructed a model to investigate the many uncertainties present in grain-surface formation of interstellar molecules. They found that weakly physisorbed heavy atoms such as C or O on top of either a grain surface or a monolayer of strongly chemisorbed species can react with abundant hydrogen to form simple molecules. Whether radicals (CH, OH) or fully saturated molecules (H_2O, CH_4) should be most abundant was unclear; the efficiency of product ejection via formation energy was not known.

Tielens & Hagen (1982) modeled the evolution of a grain surface chemical reaction network to determine the composition of grain mantles embedded in a steady-state gas-phase model. Due to the success of gas-phase models in reproducing observed abundances of gas species, they chose to ignore the influence of grain processes on gas phase abundances. They found grain mantles are formed primarily of H_2O, H_2CO, N_2, CO_2 and NH_3, with the relative abundances strongly depending on environmental parameters.

Later rate kinetics models would consider a coupled gas-grain chemistry. Models of interstellar environments that consider accretion of gas-phase species

onto grain surfaces have typical dust temperatures $\lesssim$ 20 K, such that heavy atoms and molecules (generally, anything more massive than H_2) will be unable to desorb. This depletion pathway will lead to total freeze-out if non-thermal desorption is weak, removing the possibility of a steady-state solution.

Hasegawa, Herbst & Leung (1992) used an extensive gas-phase network and added a grain surface network, solving the time-dependent system to constrain the highly uncertain surface system. They found that setting their initial hydrogen abundance in the molecular phase reduced the synthesis of complex molecules; additionally, the reaction CO + O $\rightarrow$ CO_2 was removed due to the rapid depletion of surface CO.

Later models have made gains in accuracy due in large part to efforts in the laboratory, constraining the multitude of unknown parameters required for a reaction network. Millar et al. (1991), Millar, Farquhar & Willacy (1997) and Le Teuff, Millar & Markwick (2000) detail the increasing complexity of the public UMIST database of gas-phase chemical reactions. Studies of surface binding energies via thermal desorption of ices have constrained the mobility and desorption capabilities of prominent astrophysical species (Sandford & Allamandola, 1988; Collings et al., 2003a, 2004).

1.3 Current State of Astrochemistry

In 2017, astrochemical models have increased in complexity to make use of the exceedingly large datasets produced by state-of-the-art facilities. The Atacama Large Millimeter Array (ALMA) has further expanded our knowledge of astrochemistry in star-forming environments by combining high spatial resolution

with both high spectral resolution and a large spectral bandwidth.

The EMoCA (Exploring Molecular Complexity with ALMA) survey performed a spectral line survey toward Sgr B2(N), a massive star-forming region near the galactic center, covering 84.1 to 114.4 GHz at a resolution of ~ 1.5 km s^{-1}. Belloche et al. (2015) and Garrod et al. (2017) detected the first branched alkyl molecule, isopropyl cyanide (C_3H_7CN), and via chemical models predict a high abundance of sec-butyl cyanide, a branched configuration of the next largest alkyl cyanide.

The ALMA-Protostellar Interferometric Line Survey (PILS) is an unbiased line survey of the nearby low-mass protostellar binary IRAS 16293-2422. The survey covers the complete frequency band from 329 to 363 GHz with spectral resolution of 0.2 km/s and imaging with spatial resolution of 0.5", or 60 AU physical scale (Jørgensen et al., 2016). PILS has provided many new detections towards the protostar, and the large bandwidth provided by ALMA allows for the abundances of many chemical species to be obtained in relatively short time.

ALMA's sensitivity also enables observations of molecular abundances in distant environments. The abundant CO molecule has been detected to a redshift of z≈6.9 (Venemans et al., 2017), while more complex species have been found in star-forming regions of nearby galaxies (Costagliola et al., 2015).

In this work we will be exploring the formation of molecules in the Magellanic Clouds, satellite dwarf galaxies of the Milky Way. The low metallicity and increased dust temperature present in the Magellanic Clouds provide a possible proxy for the interstellar medium of main sequence galaxies at moderate redshift; studying the Magellanic Clouds may be our best opportunity to un-

derstand how stars formed in Milky Way-like galaxies at z~2.

In Chapter 2 we cover the details of the three-phase gas-grain chemical kinetics code MAGICKAL. In Chapter 3, we update MAGICKAL to include multiple grain sizes according to a grain size distribution and separately track each grain population's temperature and surface chemistry. In Chapter 4 we apply the updated model to a study of icy envelopes surrounding massive young stellar objects in the Magellanic Clouds. We conclude in Chapter 5 and detail a current project under way to extend our investigation of Magellanic Cloud sources to hot cores, the most chemically complex regions known in interstellar space.

CHAPTER 2

MAGICKAL - MODEL FOR ASTROPHYSICAL GAS AND ICE CHEMICAL KINETICS AND LAYERING

The MAGICKAL chemical code was first introduced by Garrod (2013) and is based on prior work by Garrod (2008), Belloche et al. (2009) and Garrod & Pauly (2011). MAGICKAL utilizes a modified rate equation approach to solve a coupled network of gas phase, grain surface and ice mantle chemical reactions. This section will detail the theory and components of the model.

2.1 Rate Kinetics

The solution procedure of a rate equation network involves numerical integration of many time-dependent ordinary differential equations. For a typical bimolecular reaction:

$$aA + bB \rightarrow cC + dD \tag{2.1}$$

where A and B are reactants, C and D are products, and a, b, c, and d are the stoichiometric coefficients. The astrophysical regions of interest for this work span densities from 10^3 to 10^7 cm^{-3} and temperatures from 8 to 300 K. At densities below $\sim 10^{12}$ cm^{-3}, gas-phase collision reactions involving more than two reactants have negligible rates, leading to a value of unity for all stoichiometric coefficients for bimolecular reactions of interest. The rate of formation for a product is:

$$\frac{dn[C]}{dt} = k \cdot n[B] \cdot n[A] \tag{2.2}$$

where $n[i]$ is the number density of species i and k is the reaction rate coefficient. The number density of species in astrochemical simulations are typically ex-

pressed in relation to the local hydrogen density, n_H. The fractional abundance is written as $X_i = n_i/n_H$, and we can rewrite equation 2.2 as:

$$\frac{dX[C]}{dt} = k \cdot X[B] \cdot X[A] \cdot n_H \tag{2.3}$$

This formulation highlights the linear dependence on total gas density for bimolecular reaction rates. The reaction rate coefficient k can be determined through a variety of methods. Direct measurements of production rates can be measured in the laboratory, though scaling is required to apply measured values to astrophysical environments with lower densities than what is currently feasible in laboratory experiments. Quantum-classical rate theory can also provide reasonable estimates for computationally tractable reactions. For many reactions in modern chemical networks, however, no value has been measured; in this case, extrapolations are often made from reactions with similar functional groups. The use of chemical modelling can itself constrain reaction rates by providing abundances for comparison with observations.

2.2 Reaction Network

The reaction network used in conjunction with MAGICKAL is sourced primarily from the *osu.2005* chemical network, with updates from Garrod, Wakelam & Herbst (2007), Belloche et al. (2009), Garrod & Pauly (2011), and Garrod (2013). The basic model follows the approach of Hasegawa, Herbst & Leung (1992), with many incremental updates from e.g. Garrod (2008), Garrod & Pauly (2011), and Garrod (2013).

2.2.1 Gas Phase Reactions

In cold dark clouds, reactions in the gas phase are driven by ionized species, produced primarily by cosmic rays and partly by the photons that penetrate to the visual extinctions ($A_V \gtrsim 3$) of these regions. Photo-ionization and photo-dissociation reactions have coefficients parametrized as:

$$k = k_0 \exp(-\alpha A_V) \tag{2.4}$$

where k_0 is the rate coefficient in the unshielded interstellar radiation field (ISRF), k is the rate inside a cloud at an extinction A_V, and α is a factor that gives the relative importance of ultraviolet wavelengths in the photo-process, with larger values indicating high UV dependence. k_0 depends on the strength of the ISRF at the wavelengths relevant for absorption and the photo-disocciation cross-section of the species. Typical values for k_0 are 10^{-9} to 10^{-11}, while α typically falls between 1.5 and 3.0.

The most common molecules found in dark clouds, H_2 and CO, have reduced values of k in diffuse clouds due to self-shielding. Self-shielding occurs when the optical depth is $\gtrsim 1$ within individual transitions for a given species due to high column density of foreground material. The Lyman-Werner bands describe the discrete energy levels of H_2 transitions caused by absorption of a ultraviolet photon with energy 11.2–13.6 eV, while CO has similar discrete transitions and negligible continuum absorption channels. Many of the CO transition lines coincide with H_2 transitions, such that the self-shielding value for CO must account for H_2 column density. The reverse is not required, as CO columns are not large enough to affect the H_2 self-shielding. For models that begin at an A_V of 3, we set the exterior columns to $N_{H_2} = 1.6 \times 10^{21}$ cm^{-2} and $N_{CO} = 8.0 \times 10^{16}$ cm^{-2}.

Cosmic rays are assumed to be isotropic, though some environments require a more detailed treatment (see e.g. Cleeves, Adams & Bergin, 2013). We assume a canonical interstellar medium (ISM) CR ionization rate of 1.3×10^{-17} s^{-1}. The cosmic ray ionization rate of a given species depends only on its abundance and not on gas density; the rate is small, but becomes the primary ionizing source at dark cloud values of dust extinction.

Reaction Type	General Form			Typical k
Cosmic Ray Ionization	X + c.r.	$\rightarrow$	$X^+ + e^-$	10^{-17} s^{-1}
Photo-dissociation	$XY + h\nu$	$\rightarrow$	X + Y	$k_0 \sim 10^{-10}$ s^{-1}
Dissociative Recombination	$XY^+ + e^-$	$\rightarrow$	X + Y	10^{-6} cm^3 s^{-1}
Radiative Recombination	$XY^+ + e^-$	$\rightarrow$	$XY + h\nu$	10^{-12} cm^3 s^{-1}
Ion-Molecule Reaction	$X^+ + YZ$	$\rightarrow$	$XY^+ + Z$	10^{-9} cm^3 s^{-1}
Charge Transfer Reaction	$X^+ + YZ$	$\rightarrow$	$X + YZ^+$	10^{-9} cm^3 s^{-1}
Neutral Exchange Reaction	X + YZ	$\rightarrow$	XY + Z	10^{-11} cm^3 s^{-1}
Radiative Association	$X^+ + Y$	$\rightarrow$	$XY^+ + h\nu$	10^{-17} cm^3 s^{-1} -^{a}
				10^{-9} cm^3 s^{-1} -^{b}
Associative Detachment	$X^- + Y$	$\rightarrow$	$XY + e^-$	10^{-9} cm^3 s^{-1}

Table 2.1: Gas phase reaction types, with general forms shown and typical values for the reaction rate coefficient k.^{a}: For diatomic products; ^{b}: For polyatomic products.

Other reactions in the gas phase fall into either bond formation, destruction or rearrangement. The general reaction classes are shown in Table 2.1, along with typical values of rate coefficients. The growth of molecules occurs primarily through ion-molecule reactions; the temperature-dependent reaction rate coefficient is parametrized using the modified Arrhenius' equation:

$$k = \alpha \left(\frac{T_K}{300} \right)^{\beta} \exp\left(-\frac{\gamma}{T_K} \right) \tag{2.5}$$

The β term accounts for temperature-dependent component of the collision cross-section and reaction probability, while the final term represents an activation barrier, where present.

Many processes present in reaction networks currently used do not have laboratory measurements; for example, radiative recombination rate measurements are difficult to measure due to collisions occurring even at the lowest densities attainable in terrestrial lab settings. The collisions de-excite the recombined complex, competing with the radiative process and making the rates difficult to disentangle. In these cases, extrapolations are done from those reactions with measured values; these values can be further constrained by use of the chemical models, as extreme over- or under-production implies incorrect assumptions.

2.2.2 Grain Surface Reactions

Grain surface reactions occur when reactive species adsorb onto the grain surface and the dust temperature is low enough to permit long residence times, such that reactants can meet and interact on the surface. This occurs frequently in molecular cloud environments and is the primary source of molecular hydrogen (Gould & Salpeter, 1963; Hollenbach & Salpeter, 1971; Cohen, 1976).

The standard version of MAGICKAL considers classical dust grains, characterized by a radius of 0.1 μm, a density of 3 g cm$-$3, and 10^6 surface sites for adsorption. The gas-to-dust ratio by mass is typically set to 100 for galactic studies, or 7.568×10^{11} by number. Gas kinetic temperature T_k and dust temperature T_d values are chosen for the environment being studied (typically both temperatures are set to 10 K for models of quiescent dark clouds). We assume a sticking probability of 0.5 for neutral species that strike a grain surface, and 0.0 for all charged species. The accretion rate for a given species i, in units of cm

cm^{-3} s^{-1}, can then be calculated as:

$$R_{\rm acc}(i) = \sigma_d \langle v(i) \rangle n(i) n_d \tag{2.6}$$

where σ_d is the spherical dust grain cross-sectional area, $\langle v(i) \rangle$ is the thermal velocity of the gas-phase species i, $n(i)$ is the number density of i, and n_d is the dust number density.

We consider adsorption of neutral atoms and molecules via physisorption, caused by the van der Waals force. The typical binding energy ($E_{\rm des}$) is weak, of order 1000 K or 0.1 eV. Physisorption preserves the electronic character of both the surface and the adsorbed species, in contrast to the strong bonding of chemisorption, which is not considered in this model. The values used are set individually for each surface species, e.g. 450 K for atomic hydrogen, 800 K for atomic oxygen, and 5700 K for H_2O. These values assume a surface composed primarily of amorphous water ice. Once adsorbed, surface species may diffuse across binding sites on the dust surface. The barrier to diffusion ($E_{\rm dif}$) is uniformly set to a fraction of the desorption barrier $E_{\rm des}$. Values from 0.3 to 0.8 have been used in past work (Tielens & Hagen, 1982; Ruffle & Herbst, 2000; Cuppen et al., 2009; Garrod & Pauly, 2011); the default value used for models in this work is 0.35.

Values of $E_{\rm des}$ should change as the surface composition evolves over the course of the model. The strongest effect from changing composition is due to adsorbed H_2; at dust temperatures $\lesssim$ 8 K and when H_2 is abundant in the gas phase, model solutions find significant freeze-out of hydrogen. This result is non-physical, as the binding energy used in the calculation of H_2 accretion assumes adsorption onto an amorphous water ice surface. We instead calculate an effective binding energy which scales with the surface coverage of molecular

hydrogen. Cuppen et al. (2009) estimate that the binding energy to an H_2 surface is roughly 10 times weaker than a CO surface, leading to an effective binding energy calculation for species *i*:

$$E_{\rm des,eff}(i) = E_{\rm des}(i)\ [1 - \theta({\rm H_2})] + 0.1 E_{\rm des}(i)\ \theta({\rm H_2}) \tag{2.7}$$

where $\theta(H_2)$ is the fractional surface coverage of H_2, with the same relationship for $E_{\rm dif,eff}$. H_2 is the only chemical species expected to reach significant surface abundances and also have a significant effect on surface binding strengths; we only follow H_2 fraction for this type of modification to the binding energies.

Once on the grain surface, exothermic surface reactions can occur between mobile reactants. The time scale $t_{\rm hop}$ for surface species to "hop" from one surface site to an adjacent site via thermal motion is given by:

$$t_{\rm hop} = \nu_0^{-1}\ \exp\left(E_{dif}/T_d\right) \tag{2.8}$$

where ν_0 is the characteristic vibration frequency for the adsorbed species, assumed to be isotropic, and E_{dif} is given in Kelvin. We follow the method of Hasegawa, Herbst & Leung (1992) and calculate the vibration frequency for each adsorbate using the harmonic oscillator relation

$$\nu_0 = \left(\frac{2 n_s E_{des}}{\pi^2 m}\right)^{1/2} \tag{2.9}$$

where n_s is the surface density of sites ($\sim 1 \times 10^{15}$ cm^{-2}) and m is the mass of the adsorbed species. Typical values of ν_0 are in the range $10^{11} - 10^{13}$ s^{-1}.

Surface reactions are assumed to take place via the Langmuir-Hinshelwood mechanism, which requires the reactants to diffuse across the surface until they meet in the same binding site. The diffusion time scale $t_{\rm diff}$ describes the time required for the reactant to traverse a number of surface sites equivalent to the

entire dust grain surface. It is given simply as

$$t_{\rm diff} = N_s \, t_{\rm hop} \tag{2.10}$$

where N_s is the total number of surface sites on the grain (10^6 for a canonical 0.1 μm grain). Note that due to the random walk nature of surface diffusion, the time scale to visit every surface binding site and not just a number of sites equal to the total number would require an additional back-diffusion factor (see Willis & Garrod, 2017).

We define the diffusion rate $R_{\rm diff}$ as the inverse of $t_{\rm diff}$; then, the surface reaction rate R_{ij} in cm^{-3} s^{-1} between surface reactants i and j can be expressed as

$$R_{ij} = \kappa_{ij} \left(R_{{\rm diff},i} + R_{{\rm diff},j} \right) N_i \, N_j \, n_d \tag{2.11}$$

where N_i is the is total number of molecules (or atoms) of reactant i on a representative grain, n_d is the dust number density, and κ_{ij} is the probability of reaction upon an encounter of the reactants in a binding site. Equation 2.11 is typically implemented in rate equation networks by expressing it in terms of a rate coefficient k_{ij}, with units of cm^3 s^{-1}, as in gas-phase reactions:

$$R_{ij} = k_{ij} \, n_s(i) \, n_s(j) \tag{2.12}$$

where $n_s(i)$, the concentration of species i, is defined as

$$n_s(i) = N_i \, n_d \tag{2.13}$$

The rate coefficient is then expressed as

$$k_{ij} = \frac{\kappa_{ij} \left(R_{{\rm diff},i} + R_{{\rm diff},j} \right)}{n_d} \tag{2.14}$$

For exothermic reactions with no activation energy barrier, κ_{ij} is unity. For reactions with an activation barrier E_A, the probability of reaction upon a single

collision between reactants can be expressed as a Boltzmann factor

$$\kappa_{ij} = \exp\left(-E_A/T\right) \tag{2.15}$$

However, when reactants meet in a binding site, there can be many more than one interaction between reactants; the number of interactions increases as the reactants vibrate in the binding site, until either the reaction occurs or a reactant migrates to an adjacent binding site. Desorption is ignored, as $E_{des} > E_{dif}$, and migration rates are much faster than desorption rates. The reaction rate requires a calculation of the competition between the rate of reaction and the rates of surface migration for the two reactants. This competition is given by

$$k_{ij} = \frac{\nu\kappa_{ij}\left[k_{\rm hop}(i) + k_{\rm hop}(j)\right]}{\left[\nu\kappa_{ij} + k_{\rm hop}(i) + k_{\rm hop}(j)\right]N_s} \tag{2.16}$$

where ν is the frequency of collision between the two reactants and $k_{\rm hop}(i) = t_{\rm hop}(i)^{-1}$. We set ν to the larger of the the two ν_0 values for the two reactants. Equation 2.16 has two limits: when migration is much faster than the barrier-mediated reaction, k_{ij} depends only on $\nu\kappa_{ij}$ and not on the hopping rates; when the reaction rate is faster than thermal migration, k_{ij} depends only on the hopping rates.

Quantum Tunneling Modifications

If a barrier-mediated surface reaction involves a light reactant, i.e. H or H_2 (and possibly C or O), quantum tunneling may be the dominant pathway through which a reaction proceeds, rather than through thermal means. Hasegawa, Herbst & Leung (1992) parametrized the tunneling process through a rectangular potential as

$$\kappa = \exp\left[-2(a/\hbar)\left(2\mu E_A\right)^{1/2}\right] \tag{2.17}$$

where μ is the reduced mass and a is the width of the barrier. For surface migration of atomic or molecular hydrogen, quantum tunneling is more rapid than classical thermal hopping. For a canonical grain at T_d = 10 K and an E_{des}(H) = 450 K, the diffusion time for an H atom due to thermal hopping ($t_{\rm diff}$) is 2.50 s; the calculation for quantum tunneling migration, equivalent to equation 2.8, is given by

$$t_{qhop} = \nu_0^{-1} \exp\left[(2a/\hbar)\,(2mE_b)^{1/2}\right] \tag{2.18}$$

The quantum diffusion time for an H atom is 5.7×10^{-5} s.

Desorption Mechanisms

Surface species may return to the gas phase through a variety of mechanisms. Thermal desorption time scales are calculated as in equation 2.8, replacing E_{dif} with E_{des}. For a dust temperature of 10 K, desorption times less than 10^6 years requires $E_{des} \lesssim 600$ K, which is true only for H, H_2, and He. Heavier atomic species, e.g. carbon, nitrogen, and oxygen, have E_{des} set to 800 K; due to the exponential behavior of the barrier, thermal desorption rates are negligible for these atoms. In models of hot core regions that include a warm-up phase, dust temperatures surpass 200 K; all surface species desorb, seeding the gas phase with complex species formed on the surface during the warm-up.

Molecules formed on the surface may also desorb due to the energy of reaction breaking the surface-molecule bond. Termed reactive desorption, this was studied and implemented by Garrod, Wakelam & Herbst (2007). It is assumed that this process is important only for reactions that generate a single product; in two-product reactions, energy can be lost through lateral translation of the products.

To model reactive desorption, we take the surface-molecule bond to be an additional molecular vibrational mode and calculate the probability P for the energy in this bond to be greater than E_{des}, given an energy of reaction E_{reac}. Using Rice-Ramsperger-Kassel (RRK) theory, the probability is given by

$$P = \left(1 - \frac{E_{des}}{E_{reac}}\right)^{s-1} \tag{2.19}$$

where s is the number of vibrational modes in the system. For most reactions $E_{reac} \gg E_{des}$, such that $P \approx 1$. The rate of desorption can then be approximated as νP. However, the competition between energy loss to the surface and the breaking of the molecule-surface bond must be considered; if the rate of energy loss into the surface is too rapid, desorption will not occur. This competition is given by

$$f = \frac{\nu P}{\nu_s + \nu P} = \frac{aP}{1 + aP} \tag{2.20}$$

where ν_s is the rate of energy loss to the surface and $a = \nu/\nu_s$. We adopt a value of 0.01 for a for all reaction products, giving $f \lesssim 1\%$.

Surface species may also acquire the necessary energy for desorption from absorption of a photon. Photo-desorption rates were studied by Öberg et al. (2009); Öberg, van Dishoeck & Linnartz (2009) for H_2O, CO, CO_2, and N_2. Rates and yields for these species are included in the model; for all other species, a yield of 10^{-3} is assumed. In dark cloud conditions where $A_V \gtrsim 3$, reactive desorption yields are maintained while direct photo-desorption is strongly diminished.

Modified Rate Equations

The rate equations used to calculate bimolecular surface reaction rates, i.e. 2.11, have an implicit assumption in that the product $N_i \cdot N_j$ approximates the number of unique pairs of reactants on the grain surface. This approximation breaks down when stochastic effects become important.

We use N_i to represent the number of species i on a representative dust grain; we can be more precise and define the expectation value of the population of species i on a dust grain to be

$$\langle N(i) \rangle \equiv \sum_{N=0}^{\infty} N \, P_N(i) \tag{2.21}$$

where $P_N(i)$ is the probability of finding N units of species i on the surface at a given time. With this definition, it is apparent that equation 2.11 approximates the number of unique reaction pairs as $\langle N(i) \rangle \cdot \langle N(j) \rangle$, while the true number is instead $\langle N(i) \cdot N(j) \rangle$. This distinction may cause inaccuracies when populations are small (however, small populations alone are not sufficient to cause inaccuracies). The two population products are equal so long as the probability of population states between reactants i and j remain uncorrelated. If instead they become anti-correlated, i.e. due to a fast rate of reaction forming product ij, the probability of finding both reactants on the surface at the same time is low. The standard form of the rate equation will over-estimate the production rate of ij; in this way, we can see modifications to account for stochastic behavior will reduce reaction rates.

To determine the form of the modified rates, calculation of $\langle N(i) \cdot N(j) \rangle$ is avoided, as it would disallow the use of standard matrix-inversion solution techniques upon which the model relies. Instead, the model follows Garrod

(2008) in the use of small-grain approximation as a limiting case. We take a sample system with reactants i and j and their respective accretion rates (R_{acc}), desorption rates (K_{des}) and reaction rate (k_{ij}). In the simplest stochastic case, $\langle N(i)\rangle, \langle N(j)\rangle \ll 1$. We assume that the reaction rate is much faster than the accretion and desorption rates, such that i and j will react as soon as both are present on the surface. If this assumption holds, the rate of formation of ij no longer depends on k_{ij} but instead on the accretion rate of each reactant times the probability of the presence of its partner on the surface:

$$R_{\text{mod}}(ij) = R_{acc}(i)\,\langle N(j)\rangle + R_{acc}(j)\,\langle N(i)\rangle \tag{2.22}$$

Note that this assumes only i and j are on the surface and does not consider competition with other reactants. If only one reactant has $\langle N\rangle \ll 1$, we retain the standard rate equation, as any correlation between population states would be weak. Additionally, selection of the modified rate requires its value to be less than the standard rate; that is,

$$R_{acc}(i)\,\langle N(j)\rangle + R_{acc}(j)\,\langle N(i)\rangle \leq k_{ij}\,\langle N(i)\rangle\,\langle N(j)\rangle\,n_d \tag{2.23}$$

If a modified rate exceeds the standard rate calculation, the modified rate is ignored. Note that this simple method can produce discontinuities in values of the production rate when N_i is unity. The addition of a transition function f_{ij} is used to smooth the behavior of the production rate near populations of unity. With the addition of f_{ij}, we can apply the same production rate uniformly to all reactions (in units of s^{-1}):

$$R_{\text{trans}}(ij) = f_{ij}\cdot R_{\text{mod}}(ij) + (1 - f_{ij})\cdot k_{ij}\cdot\langle N(i)\rangle\cdot\langle N(j)\rangle \tag{2.24}$$

where the reactant populations determine the value of f_{ij}:

$$\begin{aligned}
\langle N(i)\rangle < 1, \langle N(j)\rangle < 1 : &\quad f_{ij} = 1 \\
\langle N(i)\rangle > 1, \langle N(j)\rangle < 1 : &\quad f_{ij} = 1/\langle N(i)\rangle \\
\langle N(i)\rangle < 1, \langle N(j)\rangle > 1 : &\quad f_{ij} = 1/\langle N(j)\rangle \\
\langle N(i)\rangle > 1, \langle N(j)\rangle > 1 : &\quad f_{ij} = 1/[\langle N(i)\rangle \cdot \langle N(j)\rangle]
\end{aligned} \tag{2.25}$$

This is implemented with equation 2.23 such that if the modified rate is faster than the standard rate, the total rate calculated by equation 2.24 is always equal to the standard rate.

An additional modification is used to more accurately represent the population states of reactants with $\langle N(i)\rangle < 1$. When $\langle N(i)\rangle \ll 1$, using $P(i) \approx \langle N(i)\rangle$ is typically a reasonable assumption. If the expectation value is closer to unity, the assumption $P_{N>1}(i) \approx 0$ may no longer hold. In the limit where $k_{des}(i) \gg k_{ij} \gg R_{\mathrm{acc}}(i)$, desorption dominates the destruction pathways for i; sampling the population state of the surface due to slow accretion is well described by a Poisson process. The probability of finding one or more units of species i at any moment on the surface is then (from Garrod, 2008, Eq. 25)

$$P(i) = 1 - \exp[-\langle N(i)\rangle] \tag{2.26}$$

This approximation is a better fit to complex models where reactions between heterogeneous particles are most likely; if k_{ii} were to dominate, the surface population states $N = 0, 2$ would be strongly coupled and $P(i) \approx \langle N(i)\rangle$ would fit well.

The final modification is to take a more careful account of competition. The modified rates of the form in equation 2.22 calculate the rate of accretion of each species given the presence of its partner on the surface; this assumes 100%

reaction efficiency if there is a moment in time for which both are on the surface. Instead, an efficiency factor must be introduced to account for the possibility of desorption of a reactant prior to reaction. However, a simple approach of weighting each term by $k_{ij}/[k_{ij} + k_{des}(i) + k_{des}(j)]$ overcompensates in this way: if a reactant i is present on the grain, and j accretes but quickly desorbs, i is still present on the grain and can react with the next accretion event of a j unit. The full competition calculations are presented in § 6.1 of Garrod (2008).

CO_2 Surface Treatment

As introduced in Garrod & Pauly (2011), a special treatment was added to MAGICKAL to model the formation of CO_2 on the surface. Besides the production of CO_2 from mobile CO reacting with surface OH, there is a chance that O + H → OH occurs while surface O is bound to CO ice. In this case, the energy of OH formation is more than sufficient for CO + OH → CO_2 + H. We include this possibility by tracking the fractional surface coverage of CO, $0 < \theta(\mathrm{CO}) < 1$. Then a fraction of surface O + H → OH reactions equal to θ(CO) will react to form CO_2 + H.

2.2.3 Mantle Transport and Chemistry

In addition to tracking gas-phase and grain-surface chemistry, we model a third phase to track the ice mantle that grows as species accrete on top of an existing surface layer. The implementation follows that of Hasegawa & Herbst (1993), Garrod & Pauly (2011), and Garrod (2013). Specifically, we allow for an active ice chemistry in the mantle while retaining the option to render the mantle inert;

if dust temperatures are low, the computational cost of adding mantle reactions may not be worthwhile.

In order to simulate the chemical kinetics of mantle chemistry, we assume the mobility of mantle species occurs through thermal diffusion using a similar method to surface migration:

$$k_{\text{swap}}(i) = \nu_0(i) \exp[-E_{\text{swap}}(i)/T_d] \tag{2.27}$$

where E_{swap} is the energy barrier assigned to the swapping of species i with an adjacent water molecule. With our previous use of $E_{\text{dif}} = 0.35E_{\text{des}}$, and the rough assumption that mantle species are bound to twice as many neighbors as surface species, we set $E_{\text{swap}} = 0.7E_{\text{des}}$.

Reactions within the mantle are formulated in a similar manner to equation 2.11, given by

$$R_m(ij) = N_m(i)N_m(j)[k_{\text{swap}}(i) + k_{\text{swap}}(j)]/N_M \tag{2.28}$$

where $N_m(i)$ is the mantle population of species i and N_M is the sum of all mantle species populations.

In addition to migration and reaction within the mantle, swapping between surface and mantle species also occurs. This is a pair-wise process, though explicit treatment of pair-wise coupling between surface and mantle species is not computationally feasible. Instead, we first calculate the swapping rates from mantle to surface. This rate is then matched with a rate of surface species swapping into the mantle, and we apply the rate to each species according to its relative surface coverage. The rate of swapping is determined by the relative sum populations of the surface and mantle, giving the rates

$$R_{\text{swap,m}}(i) = N_m(i) \frac{N_S}{N_M} k_{\text{swap}}(i) \tag{2.29}$$

$$R_{\text{swap,s}}(i) = \frac{N_s(i)}{N_S} \sum_j R_{\text{swap,m}}(j) \tag{2.30}$$

where $R_{\text{swap,m}}(i)$ is the rate of swapping of species i from the mantle to the surface, N_m and N_s are the mantle and surface populations, respectively, of species i, N_M and N_S are the sum populations of the mantle and surface, and $R_{\text{swap,s}}(i)$ is the rate of swapping of species i from the surface to the mantle.

2.3 Physical Model Parameters

The model has physical parameters in addition to the chemical network. Their values are set by the environment of interest; values given here are for a typical model of quiescent dark cloud chemistry in the Milky Way.

The gas phase parameters to be set include: gas density, at 2×10^4 cm^{-3}; gas temperature, at 10 K; and visual extinction (A_V), at 10. A relation is used to convert the visual extinction due to dust into an exterior column of molecular H_2 and CO for self-shielding calculations; for the region from A_V of 0 to 1, we assume no column of H_2 is present. For each magnitude of extinction beyond 1, we use $N_{H_2}/A_V = 8.0 \times 10^{20}$ cm^{-2} mag^{-1}. We then set the CO column to be $5 \times 10^{-5} \cdot N_{H_2}$.

The cosmic ray ionization rate affects chemistry in all phases, and we use a default value of $\zeta_0 = 1.3 \times 10^{-17}$ s^{-1}. The external UV field has separate scale factors for gas and grain chemistry, modifying the rates of photo-ionization, photo-dissociation and photo-desorption.

The parametrization of dust in MAGICKAL has been explained earlier in Section 2.2.2; further modifications to the treatment of dust in MAGICKAL will

be covered in Chapter 3.

MAGICKAL can be run as a single point model with either static or dynamic temperatures, densities, and A_V. Models of quiescent clouds are run with fixed parameters, while simulating the formation of cores in molecular clouds can involve increases in density by orders of magnitude with an associated drop in temperature and jump in A_V.

CHAPTER 3

THE EFFECTS OF GRAIN SIZE AND TEMPERATURE DISTRIBUTIONS ON THE FORMATION OF INTERSTELLAR ICE MANTLES

3.1 Introduction

The chemistry of both quiescent and star-forming regions of the interstellar medium (ISM) is influenced significantly by processes occurring on the surfaces of the dust grains that permeate the gas (e.g. Whittet et al., 1989; Chiar et al., 1995; Geppert et al., 2006; Boogert et al., 2008; Cuppen et al., 2009). Atoms and molecules may accrete onto the grain surfaces, depleting gas-phase abundances, while allowing molecular ice mantles to form on the grains, typically through the addition of atomic hydrogen to atoms and simple molecules such as CO. The products of surface chemical reactions may be returned to the gas-phase by both thermal and non-thermal desorption, while the composition of the bulk ices may be further altered by processing associated with star formation. However, observations of infrared line absorption toward dark clouds and star-forming regions indicate that, while specific abundances may vary between individual sources, the major solid-phase repositiories of oxygen, carbon and nitrogen are a small group of simple, stable molecules: H_2O, CO, CO_2, CH_4, CH_3OH, H_2CO and NH_3 (see Gibb et al., 2000; Whittet et al., 2007; Öberg et al., 2008).

Various computational models of the combined gas-phase/grain-surface chemical system exist and are well described in the literature (e.g. Hasegawa, Herbst & Leung, 1992; Aikawa et al., 2008; Garrod, 2008; Wakelam et al., 2010;

This chapter is an adapted version of the published article (Pauly & Garrod, 2016).

Vasyunin et al., 2009). Common to almost all such models is the adoption of a single, representative dust-grain radius, typically 0.1 μm, with the associated number of surface binding sites on the order of 1 million. In fact, a size distribution of interstellar dust grains was defined based on observational data by Mathis, Rumpl & Nordsieck (1977), with the simple relationship $dn \propto a^{-3.5} da$, where a is the radius of a spherical grain and $0.005\mu m < a < 1.00\mu m$. More recent work by Weingartner & Draine (2001) has defined the distribution more precisely.

The use in astrochemical models of a single grain size has, so far, worked adequately well for two main reasons: firstly, in the majority of astrophysical applications, there is a net deposition of material from the gas-phase onto the grains. The key parameter affecting the gas-phase chemistry is not the individual sizes of grains in the distribution, but the total accreting surface area per unit volume of gas, which can be defined without requiring a size distribution.

The second reason concerns the grain-surface chemistry itself. Most gas-grain models employ surface reaction rates of the form

$$R_{\mathrm{AB}} = [k_{\mathrm{hop}}(A) + k_{\mathrm{hop}}(B)]\, n(A)\, n(B)/n_s \tag{3.1}$$

where R_{AB} is the rate of the reaction between species A and B (assuming no activation barrier is present), k_{hop} is the inverse lifetime of a particular species to hop from one binding site to an adjacent site, $n(A)$ and $n(B)$ are the abundances of species A and B, and n_s is the number of binding sites on the surface, taken in the same units as $n(i)$. Grain-surface abundances are typically parameterized as a fraction with respect to total hydrogen, following the usual treatment for gas-phase species. As explained by Acharyya, Hassel & Herbst (2011), a simple chemical system consisting of accretion, desorption and surface reactions gov-

erned by equation (1) is unaffected by the choice of representative grain size, so long as the surface area available for accretion is held constant.

However, the fidelity of such an approach may break down for several reasons. Firstly, as described by Acharyya, Hassel & Herbst (2011), the growth of an ice mantle on the grain surface must result in an increase in the accretion cross section of the grains. This may be treated by modeling the grain/ice radius explicitly, but the increase of radius with ice mantle is nevertheless dependent on the assumed underlying grain size (as well as its morphology), requiring an explicit grain size to be chosen.

Secondly, equation (1) is not universally applicable to all surface reactions at all times, due to stochastic effects (see Garrod, 2008). These effects become important under conditions where both reactants in equation (1) attain surface populations close to or less than one per grain. Such conditions can become especially prevalent for small grains. Any method used to treat such effects explicitly, including the so-called modified-rate method, necessarily considers the species populations per grain, which again breaks the independence of the system from the choice of grain size.

Perhaps most importantly, the temperatures of the dust grains are strongly dependent on their sizes. A simple analysis, based on the assumption that the dust absorption efficiency for relevant wavelengths is of order unity (Krügel, 2003), indicates that grain temperatures are proportional to $a^{-1/6}$, where a is the dust-grain radius. As found by Garrod & Pauly (2011), while elements of the grain-surface chemistry are robust to small changes in temperature in the 8 – 12 K range, others may vary drastically; the abundance and formation mechanism of surface CO_2 in particular was found to switch according to a threshold tem-

perature of around 12 K, with values greater than this leading to highly efficient conversion of CO to CO_2, while temperatures below this value produced much more moderate CO_2 formation. The inclusion of a distribution of grain sizes would allow grain-size populations to fall either above or below this threshold temperature, under static conditions. Furthermore, the collapse models of Garrod & Pauly (2011) produced falling dust temperatures, as visual extinction increased, reducing the degree of grain heating by the external, interstellar radiation field. The consideration of a size distribution would allow different populations to reach different temperatures at each stage of collapse.

Acharyya, Hassel & Herbst (2011) used size distributions in gas-grain chemical models, finding no increase in agreement with observations of either gas or grain species. However, the dust temperatures were fixed, and held uniform across all grain sizes, and the models did not include a method to reproduce the stochastic behavior of the surface chemistry.

In this study, we expand the approach of Garrod & Pauly (2011), to include a distribution of initial grain sizes, with the radii of each grain population increasing as ice mantles are formed. The grain radii influence the surface chemistry through the accretion rates of gas-phase species, through the determination of the absolute populations of reactants per grain, and in the calculation of grain temperatures, which affects the surface diffusion and desorption rates. We investigate the effects of the grain-size and temperature distributions on the formation of the major components of interstellar ices, under static conditions, as well as under the varying density, extinction and dust temperature conditions associated with collapse to form a dark-cloud core.

The computational and modeling methods used are outlined in Section 2.

Results are presented in Section 3, and discussed in Section 4. We highlight the main conclusions of this study in Section 5.

3.2 Methods

We use a version of the three-phase gas-grain model *MAGICKAL* (Garrod, 2013) to simulate the coupled gas-phase and grain-surface chemistry. The surface consists of one chemically-active monolayer, whose total allowed population varies with grain size (see Section 2.1). Following Garrod & Pauly (2011), due to the low-temperature conditions used in the models, chemistry *within* the ice mantles themselves is switched off, as is bulk diffusion between ice surface and mantle; the ice mantle beneath the surface acts as an inert store of material. A net gain in surface atoms and molecules (due to reaction, desorption and accretion) results in a commensurate transfer of surface material into the mantle, with each chemical species being transferred in proportion to its abundance in the surface layer. A similar transfer occurs in the case of a net loss of surface atoms and molecules, with species transferred to the surface layer according to their abundances in the mantle.

The dust-grain chemical model is expanded to include all reactions and processes for an arbitrary number of grain-size populations, upon each of which an individual surface chemistry is traced. For this reason, the gas-phase and grain-surface chemical network is reduced somewhat from that used by Garrod (2013), to allow faster numerical integration. This mainly involves the removal of carbon-chain species with greater than 5 atoms and of species and reactions related to the elements Si, Cl and P. The network includes a total of 475 gas-

phase species, of which the 200 neutrals may also reside on the grain surfaces or within the ice mantles. The network includes photo-dissociation of surface species, as well as photo-desorption and reactive-desorption processes (see Garrod, Wakelam & Herbst, 2007; Garrod, 2013). Gas-phase photo-dissociation of H_2 and CO are treated following Lee et al. (1996), as in our previous models. The grain surface chemistry is treated using modified rate method "C", of Garrod (2008).

3.2.1 Grain-Size Distribution

In the models presented here, we consider the grain population to be initially composed of a distribution of grain radii as defined by the classic description of Mathis, Rumpl & Nordsieck (1977), wherein

$$dn = c \times a^{-3.5} da \tag{3.2}$$

where n is the population of the specific grain size a, and c is a constant, with upper and lower limits to the distribution of 0.25 and 0.005 μm. A value of $c = 7.762 \times 10^{-26}$ is taken from Draine & Lee (1984), which assumes silicate grains.

Here, each grain is assumed to be spherical, having a cross-sectional area of $\sigma = \pi a^2$. The full size distribution is divided into N_b bins, equally-spaced across the range of $\log_{10} \sigma$. Since the pertinent quantity for the purposes of accretion and surface coverage is area, not radius, this binning method ensures optimal coverage of the full range of grain conditions. For each bin, i, the mean cross-sectional area of grains between its lower and upper limits, $< \sigma(i) >$, is calculated (using equation 2), and this value is used as the representative grain

area for this bin, from which its radius – and thus volume – is also calculated.

3.2.2 Grain Mantle Growth

The new models also consider the time-dependent ice-mantle growth in the calculation of dust-grain radii. In line with our previous models, we assume an areal surface binding-site density of $1/A_s = 1.0 \times 10^{15}$ cm^{-2}, which provides the surface density of sites and surface species. In order to determine the physical depth of a surface monolayer, we simply assume $d_{\rm ML} = A_s^{1/2}$.

As a dust grain gains material, its radius must grow. Thus, at each moment in model time, the radius of each dust-grain population is assessed, with each constituent atom or molecule of the ice mantle and surface layer adding a volume $A_s^{3/2}$ to the basic grain volume for each grain population. The effective radius, $a_{\rm eff}(i)$, of each grain is then re-calculated assuming sphericity. The number of binding sites on each grain-size population is thus also calculated at each moment, according to $N_s(i) = 4\pi a_{\rm eff}^2(i)/A_s$. This value is used in the calculation of surface chemical rates (Eq. 1). An effective cross-sectional area for each grain population is also calculated, $< \sigma_{\rm eff}(i) >$, which determines the rate of accretion of gas-phase material onto that grain population.

3.2.3 Grain Temperature

Here, we present certain models that include a distribution of grain temperatures across the size distribution. In order to calculate the variation of temperature with effective radius, we use the simple approximation $T_d \propto a_{\rm eff}^{-1/6}$.

Although this relationship is strictly only applicable in the case that the dust is fully efficient at absorbing relevant photons for heating and the dust temperature is smooth over time, it allows the general behavior of the grain-size distribution to be traced in a simple manner. A more accurate approach to grain temperatures at the smallest sizes may be incorporated into future models.

In the collapse models presented, the dust temperatures are determined according to the expression derived by Garrod & Pauly (2011, equation 17). This expression refers to a canonical grain of 0.1 μm radius, whose temperature varies according to the heating–cooling balance of the grain at various visual extinctions. This temperature is also scaled using the above relationship to take account of the varying grain sizes of each grain population, as the ice mantles grow.

3.3 Results

To investigate the effects of the grain-size distribution, we present models that differ incrementally from three control models. Each such control model assumes a single grain size (i.e. $N_b = 1$) with a temperature of 8, 10 or 12 K, a visual extinction of 10 and a gas density $n_H = 2 \times 10^4$ cm^{-3}. All static dark cloud models are run at this density, and all models in this paper assume a fixed *gas* temperature of 10 K. The single-grain control models are labeled 1G_T8, 1G_T10, and 1G_T12 respectively; see Table 1. Table 2 shows the initial and final effective grain sizes for these and other models. It should be noted that, due to the strong bias of Eq. (2) toward small grain sizes, the initial grain size of the single-grain models is ~10 times smaller than the typically-adopted representative grain size

in previous models.

The next set of models uses a distribution of 5 grain sizes ($N_b = 5$), with a *uniform* dust-grain temperature of 8, 10 or 12 K across all grain sizes. These models are labeled 5G_T8_UNIF, 5G_T10_UNIF, and 5G_T12_UNIF.

The final set of dynamically static models assumes a dust-temperature distribution, with the initial temperature determined by grain radius, as described in Section 2. A systemic temperature is defined, of 8, 10 or 12 K, which refers to the temperature assigned to a grain with an effective size (i.e. grain + mantle) of the canonical 0.1 μm radius. The initial temperatures of each of the 5 grain populations are scaled to this temperature, and are then allowed to change according to the ice-mantle growth that modifies the effective grain radius in each population. The three models are labeled 5G_T8_DIST, 5G_T10_DIST, and 5G_T12_DIST.

We also present results from a free-fall collapse model, labeled 5G_COLL, with an initial density $n_H = 3 \times 10^3$ cm^{-3} and a final density $n_H = 2 \times 10^4$ cm^{-3}, as carried out by Garrod & Pauly (2011). The initial dust temperature is determined by the initial visual extinction, which is set to $A_V = 3$ such that the model finishes at similar density and A_V to our dark cloud models. The associated increase in visual extinction results in a drop in the temperature of the canonical 0.1 μm grain from 14.72 K to 8.14 K. In this model, the temperature of each grain population varies both with the increasing visual extinction, caused directly by collapse, and with the increase in grain-mantle size, which also acts to lower the grain temperature. Note that in any model where a temperature distribution is used which depends on grain size, the temperature may also vary as a result of grain-mantle growth.

Model		N_G	$T_D[0.1\mu m]$	A_V
1G_T8		1	8	10
1G_T10		1	10	10
1G_T12		1	12	10
5G_T8_UNIF		5	8	10
5G_T10_UNIF		5	10	10
5G_T12_UNIF		5	12	10
5G_T8_DIST	(i)	5	8	10
5G_T8_DIST	(f)	5	7.65	10
5G_T10_DIST	(i)	5	10	10
5G_T10_DIST	(f)	5	9.62	10
5G_T12_DIST	(i)	5	12	10
5G_T12_DIST	(f)	5	11.59	10
5G_COLL	(i)	5	14.72	3
5G_COLL	(f)	5	8.14	10.63

Table 3.1: List of models and parameters used, where N_G is the number of grain sizes discretized from the grain size distribution (if used), $T_D[0.1\mu m]$ is the initial temperature of a dust grain with radius = 0.1μm, and A_V is the visual extinction. For the DIST and COLL models, initial (i) and final (f) values are given.

3.3.1 Mantle Growth and Temperature Evolution

Figure 3.1 shows the grain-size evolution for all of the various models. Mantle growth occurs as gas species accrete onto grain surfaces and form ice mantles. Panel 3.1(a), corresponding to the static, single-grain, T_d = 10 K model, shows significant growth beginning around 10^4 yr. This growth is seen at similar times in the five-grain model, shown in Panel 3.1(c). As growth is driven by accretion, mantle growth of a given grain size is determined primarily by the total cross-sectional area of that population. Mantle growth is also modified by the grain temperature; if the temperature is sufficiently high that desorption of a

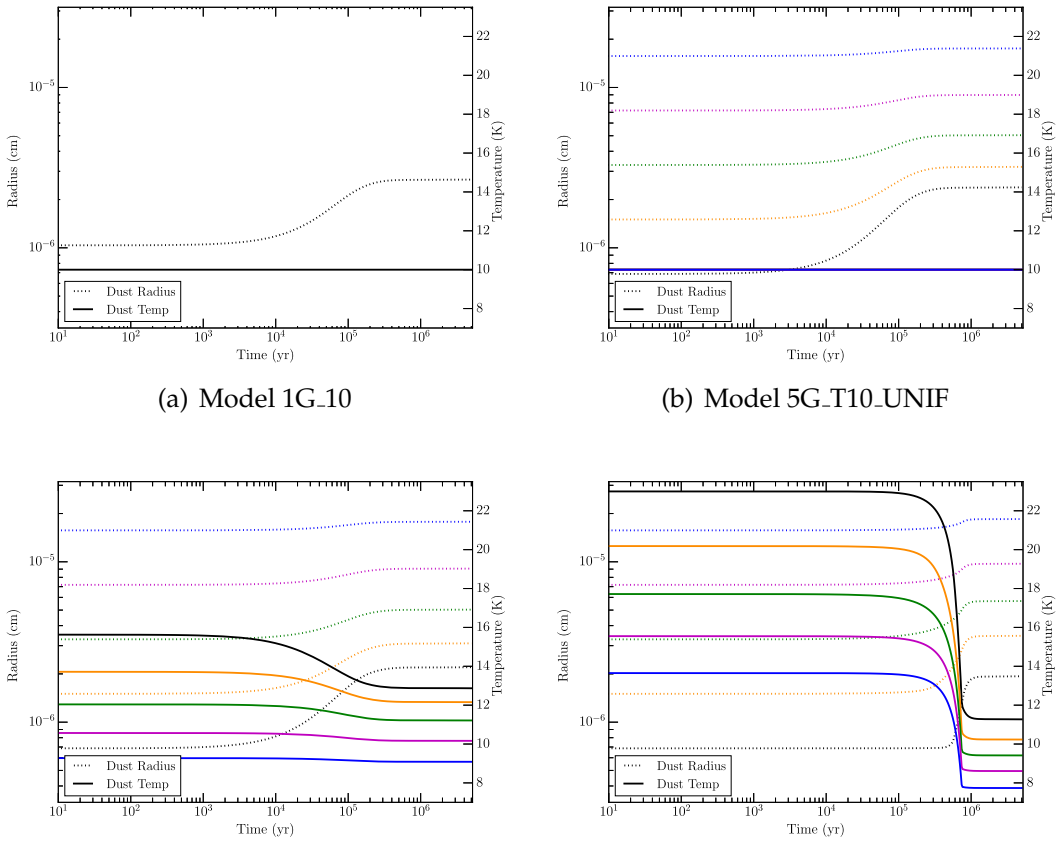

(a) Model 1G_10

(b) Model 5G_T10_UNIF

(c) Model 5G_T10_DIST

(d) Model 5G_COLL

Figure 3.1: Grain size and temperature evolution for the four classes of models. Grain size is shown on the left side using the dashed lines, while the temperature is read off the right side using the solid lines. Colors correspond to grain sizes; temperature and grain size line colors correspond to the same grain population.

common species is frequent, ice accumulation rates may be lower. This can be seen by comparing the total growth of the smallest grain for model 5G_T10_DIST (which uses a distribution of time-dependent dust temperature) to the growth of the same grain size in model 5G_T10_UNIF (in which all five grain sizes have temperature 10 K), as shown in Table 3.2.

The smallest grains are shown to grow significantly, tripling their radius in most cases. Also, while an individual large grain has greater cross-sectional

Model		R_{gr1} [μm]	R_{gr2}	R_{gr3}	R_{gr4}	R_{gr5}
1G_**	(i)	0.0104	-	-	-	-
1G_T8	(f)	0.0285	-	-	-	-
1G_T10	(f)	0.0266	-	-	-	-
1G_T12	(f)	0.0259	-	-	-	-
5G_****	(i)	0.0069	0.015	0.033	0.072	0.157
5G_T8_UNIF	(f)	0.0257	0.034	0.053	0.092	0.177
5G_T10_UNIF	(f)	0.0238	0.032	0.050	0.090	0.175
5G_T12_UNIF	(f)	0.0231	0.031	0.049	0.088	0.175
5G_T8_DIST	(f)	0.0234	0.032	0.052	0.094	0.182
5G_T10_DIST	(f)	0.0220	0.031	0.050	0.091	0.178
5G_T12_DIST	(f)	0.0224	0.031	0.048	0.086	0.176
5G_COLL	(f)	0.0193	0.035	0.057	0.097	0.185

Table 3.2: Initial grain size (i) and final grain size (f) in μm for each grain size in all models used. Note that for a given number of grain sizes, all models start with the same initial radii.

area, due to the lower population of large grains the dominant ice component is found on the smallest grains.

Figure 3.1 also shows the temperature evolution of the grains. For the single grain and uniform temperature models, we set a fixed temperature and no change occurs. The temperature distribution models show temperature evolution due to grain growth. Following the aforementioned power law, as grain radius increases the grain temperature drops. This temperature variation can be a strong determinant as to which chemical species are abundant, due to the temperature-sensitive nature of grain surface reactions.

3.3.2 Chemical Evolution - Single Grain

Figure 3.2 shows the depth-dependence of important mantle species for the three single-grain models. Ice abundances are plotted as a fraction of the total ice present in each monolayer, versus the depth of that monolayer, which is normalized to the final amount of ice in the mantle at the end of the model run. Plotted values toward the left of the plot indicate ices that were deposited earlier in the chemical evolution of the cloud, and which are thus deeper down in the mantles; values toward the right were more recently deposited and nearer to the surface. H_2O comprises the majority of the ice. CO is gradually formed in the gas phase and accreted onto the surface; its abundance in the ice grows steadily with its gas-phase abundance. CO_2 is produced on the surface; the dominant formation mechanism in this model is formation of OH on a CO ice surface, as described by Garrod & Pauly (2011). This produces a final CO_2 abundance of roughly 25 percent with respect to CO for the 8 and 10 K cases, although it is somewhat higher in the 12 K model. These ratios are low when compared with observed values for dark clouds.

Shown in Table 3.3 are the mantle ice fractions with respect to water at 10^6 years for all models. This time is chosen for the model output as it is a representative time scale for the quiescent stage of molecular clouds. The CO ice abundance matches well with observed dark cloud values (e.g. Elias 16, from Gibb et al., 2000). High-mass young stellar object observations from Gibb et al. (2000) and Whittet et al. (2011) show a range of abundances with varying levels of model agreement. CO_2 abundance in the three single grain models increases with increasing dust temperature. This reproduces the results of prior work - near 12 K, CO surface diffusion and reaction with OH becomes competitive

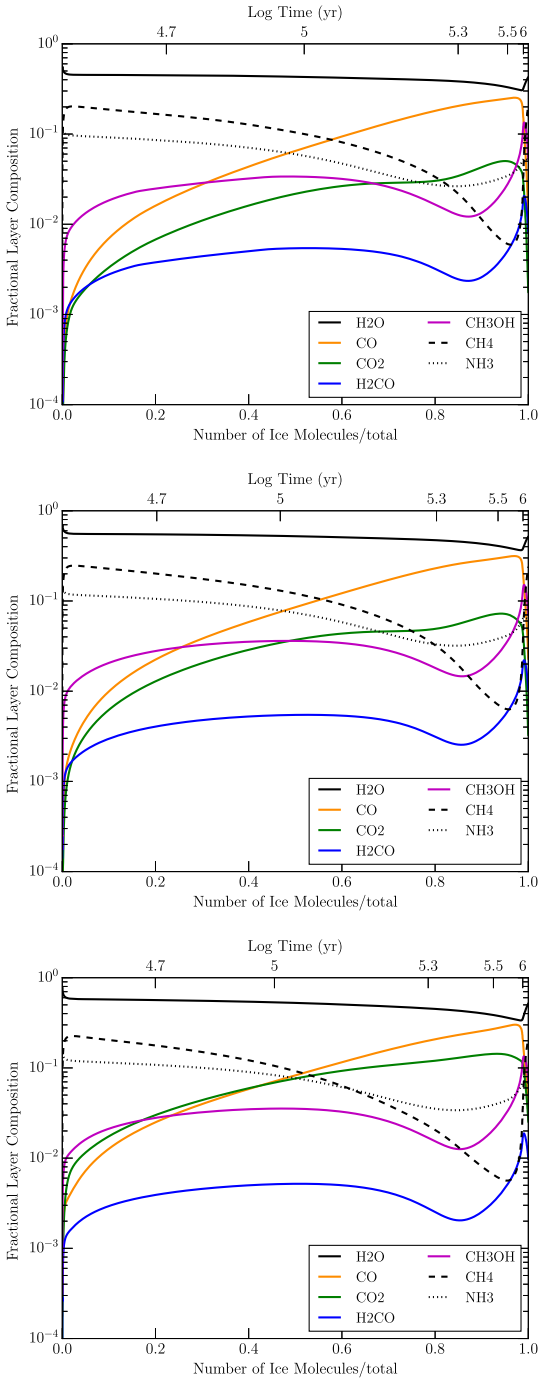

Figure 3.2: Shown is the evolution of the grain mantle species for the single grain models, with 1G_T8 in the top panel, 1G_T10 in the middle, and 1G_T12 on bottom. Fractional composition of each ice monolayer is shown on the y axis for a given monolayer depth shown on the x axis, as normalized to the final amount of ice in the mantle.

Species	H_2O	CO	CO_2	CH_3OH	H_2CO	CH_4	NH_3
1G_T8	2.08(-4)	21.6	5.0	6.2	1.0	24.4	14.1
1G_T10	2.02(-4)	23.1	6.7	5.8	0.89	23.6	14.3
1G_T12	1.84(-4)	21.6	14.9	5.6	0.83	19.6	14.8
5G_T8_UNIF	2.16(-4)	19.1	4.6	5.5	0.92	27.1	14.9
5G_T10_UNIF	2.03(-4)	23.2	6.8	5.5	0.85	23.4	15.1
5G_T12_UNIF	1.83(-4)	21.9	15.3	5.4	0.80	19.9	15.2
5G_T8_DIST	2.02(-4)	23.7	7.1	5.7	0.88	22.5	15.3
5G_T10_DIST	1.59(-4)	7.9	36.2	2.9	0.42	23.6	20.5
5G_T12_DIST	1.58(-4)	1.1	43.2	2.1	0.32	25.6	26.8
5G_Coll	1.39(-4)	29.7	31.0	6.3	1.1	12.4	21.7
Elias 16[a]	2.5(18)	25	18	<3	...	...	≤ 9
W33A[a]	1.10(19)	8	13	18	3	4	15
NGC 7538 IRS9[b]	6.7(18)	37.6	23.1	7.1	...	...	...

Table 3.3: Mantle abundances at 5×10^6 years for relevant species in models and observed dark clouds. The value of H_2O listed is with respect to total atomic hydrogen abundance, while the values for other species are given as abundance in percent of the H_2O mantle abundance. For the three observations, the H_2O value is the observed column density, with the following column values in similar fashion to the models.[a]: Gibb et al. (2000); [b]: Whittet et al. (2011)

with the water-forming reaction OH + H_2, efficiently converting CO to CO_2.

The hydrogen-rich species CH_4 and NH_3 are strongly produced in the model at early times, with abundances significantly greater than observed values. This could be a result of atomic initial conditions and the lack of treatment for the cloud's early formation period. CH_4 is more abundant in low temperature models, likely a result of decreased reaction competition for carbon hydrogenation at lower temperatures (see also Garrod & Pauly (2011) on this point).

Methanol (CH_3OH) is produced by the successive addition of hydrogen to CO on the grain surface. Efficient production of methanol requires an availabil-

ity of atomic hydrogen and sufficient time for it to react with CO and H_2CO - the limiting steps in the formation pathway, due to the activation energy barriers present in those reactions. If accretion, and consequent formation of new ice-mantle layers, is too rapid, CO and H_2CO can be frozen into the mantle without full conversion to methanol. Methanol ice is formed at a roughly constant rate throughout the single grain models.

3.3.3 Chemical Evolution - Grain Size Distribution

The first implementation of the grain-size distribution begins with models of multiple grain sizes all fixed at a uniform temperature; separate models are run at 8, 10, and 12 K. All models begin with the same total grain cross-section. The temperature is held fixed throughout the model run, despite the differing initial grain size and the changing grain size through time, as seen in Figure 3.1. Differences in final composition between single-grain and multiple-grain models with equal temperature (e.g. 1G_T8 and 5G_T8_UNIF) should be a result only of how the cross-sectional and surface area are distributed amongst the grains. Shown in Figure 3.3 is the mantle evolution for model 5G_T10_UNIF.

For models with multiple grains, it can be informative to plot the aggregate behavior of all grain surface and mantle species. We plot the aggregate mantle behavior by weighting each individual grain surface abundance by that grain's accretion rate. We then sum the weighted abundances from each grain to find an aggregate surface value for a given species. The composition of new mantle ice follows from the composition of the surface. The aggregate mantle in Panel 3.3(a) shows little difference from the single grain model. Compar-

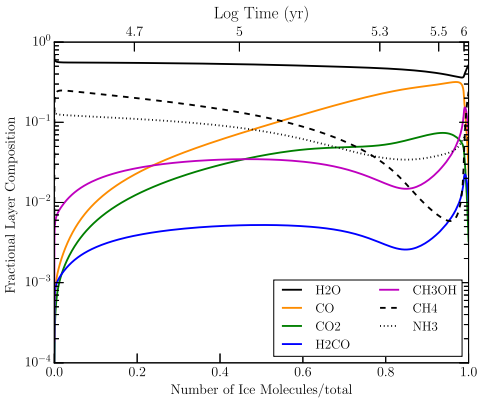

(a) Aggregate Ice Mantle

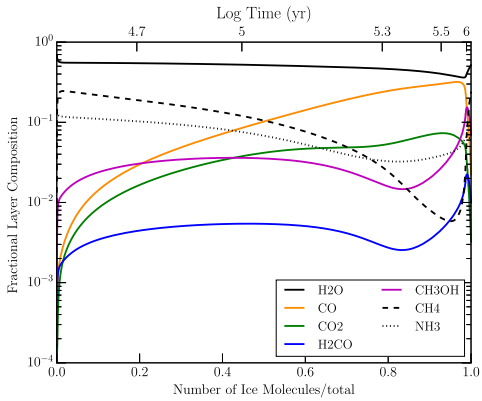

(b) Grain Size 1

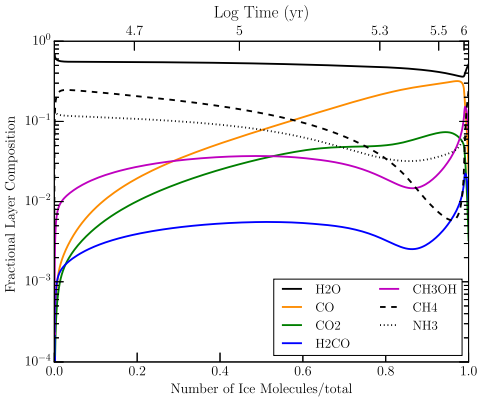

(c) Grain Size 2

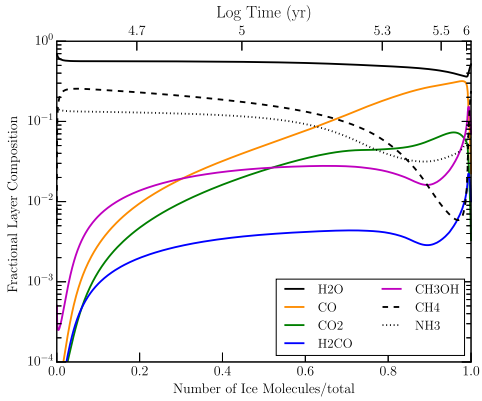

(d) Grain Size 3

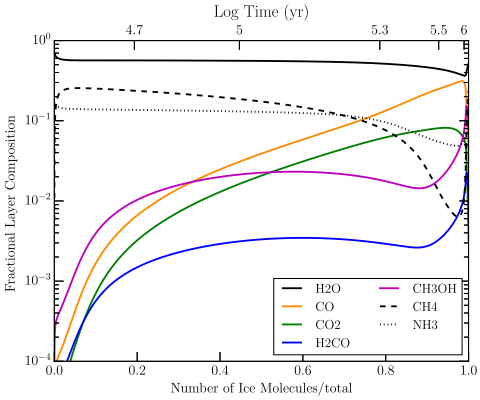

(e) Grain Size 4

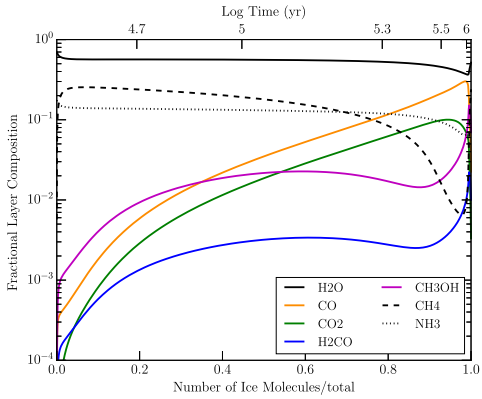

(f) Grain Size 5

Figure 3.3: Chemical evolution for model 5G_T10_UNIF. The upper left panel shows the evolution of the aggregate ice mantle, while the other panels show the evolution for the smallest grain (1) to the largest grain (5). No large differences are present between the grain sizes.

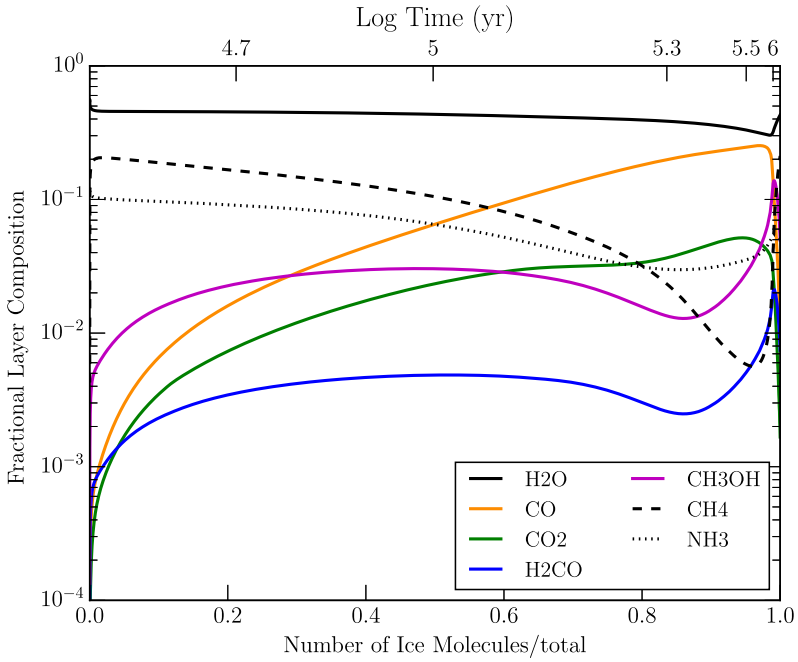

(a) Aggregate Ice - Model 5G_T8_UNIF

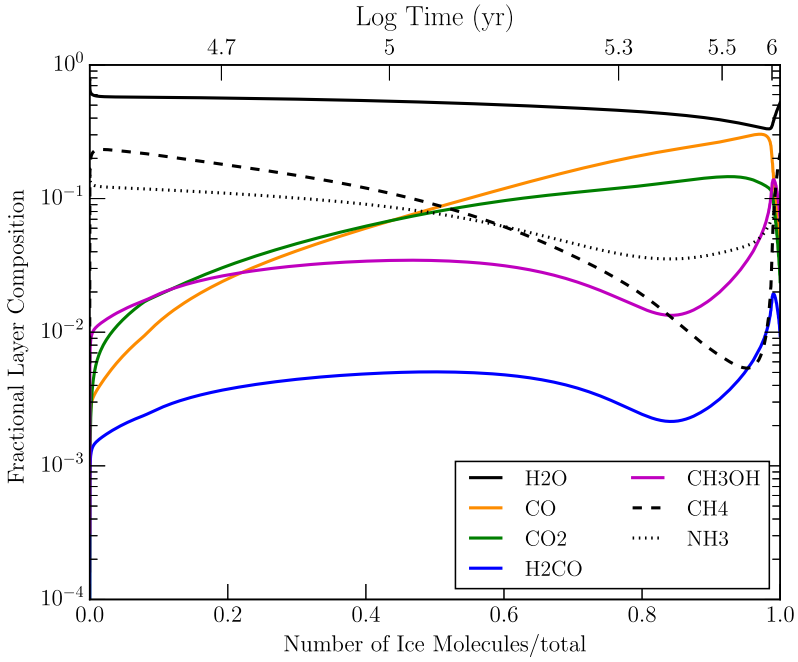

(b) Aggregate Ice - Model 5G_T12_UNIF

Figure 3.4: Aggregate mantle evolution for models 5G_T8_UNIF and 5G_T12_UNIF.

ing 1G_T10 and 5G_T10_UNIF in Table 3.3 shows the models are largely similar, with only a marginal discrepancy in NH_3 abundance. Examining the individual grain populations in 5G_T10_UNIF, the largest grains seem to produce more NH_3 at later times than expected. Apart from NH_3, it seems that the grain distribution alone has no large effect on the chemistry of the cloud.

Figure 3.4 shows the aggregate ice mantles for the 5G_T8_UNIF and 5G_T12_UNIF models, which constitute the sum of each species over all grain-size populations (naturally weighted according to the abundance of each grain population). CO and CO_2 abundances vary with temperature as expected - there is more CO_2 production and less CO at higher temperatures.

The grain-size distribution introduces an individual accretion rate for each grain size, as well as a size-dependent total number of binding sites. The change in number of binding sites can affect the chemistry by changing the amount of time taken for a species to diffuse across the full grain surface. However, the aggregate behavior of the five-grain, uniform-temperature models is comparable to the single-grain models, implying that a grain-size distribution alone does not strongly affect the surface chemistry.

3.3.4 Chemical Evolution - Grain Size and Temperature Distribution

Figure 3.5 shows the evolution of the mantle chemistry for model 5G_T10_DIST, in which the temperature of each grain population varies with the combined grain and ice mantle radius. It is apparent that the initial dust temperature

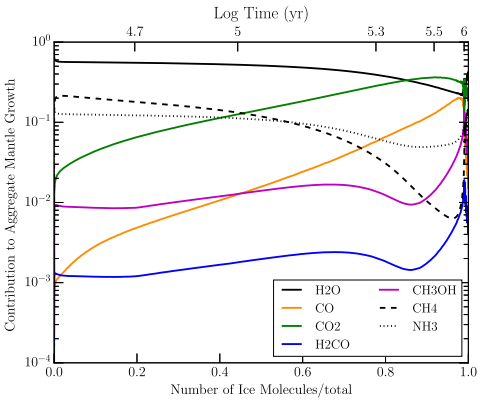

(a) Aggregate Ice Mantle

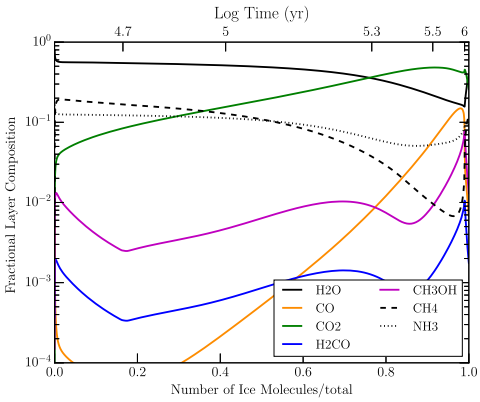

(b) Grain Size 1

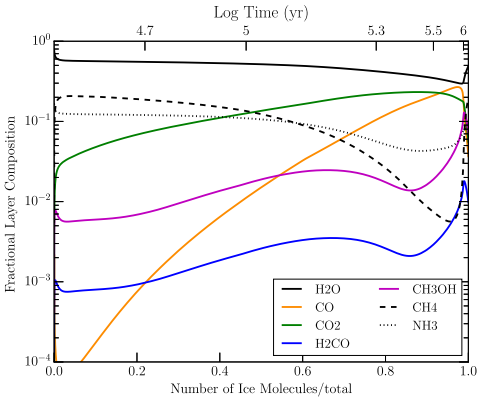

(c) Grain Size 2

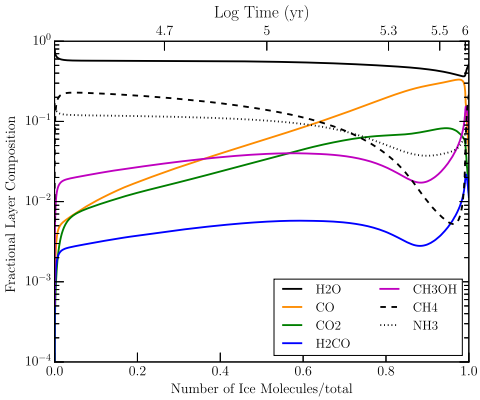

(d) Grain Size 3

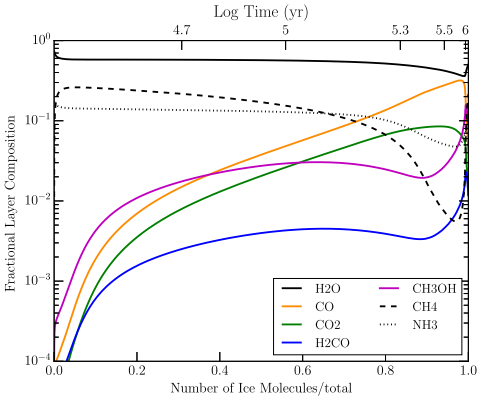

(e) Grain Size 4

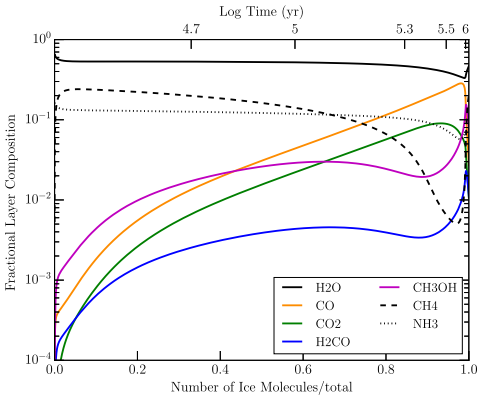

(f) Grain Size 5

Figure 3.5: Chemical evolution for model 5G_T10_DIST. The upper left panel shows the evolution of the aggregate ice mantle, while the other panels show the evolution for the smallest grain (1) to the largest grain (5). The temperature variation, both between grains and as individual grain populations grow, determine the CO/CO_2 chemistry.

distribution greatly affects the surface chemistry. On the two smallest grains, shown in Panels 3.5(b) and 3.5(c), CO_2 formation is initially highly efficient, with initial $T_d \geq 12K$. On the larger grains, the cold chemistry remains, and CO is more abundant than CO_2. As shown in Table 3.3, the total aggregate amount of water ice has decreased due to increased competition by CO in reactions involving OH.

The effects of grain growth are also seen in the chemical evolution of the small grains. As the ice mantles grow and T_d drops (for grain size 1, from 15.6 K to 12.9 K), the CO_2/CO ratio decreases. The effect is most dramatic in the two smallest sizes, as CO fractional abundance changes by up to three orders of magnitude. Grain size 2 (Panel 3.5(c)) crosses the temperature threshold for efficient CO_2 production, and briefly has a surface CO_2/CO ratio <1. As a result of the efficient CO_2 production, aggregate CO abundance drops to only 8 percent with respect to H_2O. This is on the low end of observed dark cloud values (Table 1).

The hydrogenated species in Model 5G_T10_DIST are again overproduced. NH_3 abundance has increased when compared with model 5G_T10_UNIF and is greater than observed dark cloud values. CH_4 abundance is relatively consistent across all static models. CH_3OH abundance is consistent with observed values and is not affected greatly by the temperature distribution.

With a grain temperature distribution, the 8 K and 12 K models are more varied when compared with the 10 K equivalent model (again, with this temperature being assigned to the canonical grain with radius 0.1μm). Figure 3.6 shows the size and temperature evolution of models 5G_T8_DIST and 5G_T12_DIST. The mantle-growth behavior is comparable, while the general form of the tem-

perature evolution is similar but scaled by the 4 K difference. This is expected, as the temperature evolution is determined by the rate of accretionary growth.

Figure 3.7 shows the chemical evolution of the two models. The extreme temperature of grain size 1 in 5G_T12_DIST produces a CO_2-dominated mantle, with CO comprising less than 10^{-4} of a layer in most of the mantle layers. Due to the majority of the dust cross-sectional area coming from the smallest grain size, the aggregate chemistry of 5G_T12_DIST is CO_2 dominated. Grain size 5 shows fairly efficient production of CH_3OH, but the low accretion rates caused by the small population of the largest grain size causes the effects of grain 5 to be muted in the aggregate mantle. Model 5G_T8_DIST has a CO dominated chemistry, with the temperature of only the smallest grain rising above 12 K, and only for the beginning of mantle accumulation. As the temperature of the smallest grain population drops, the chemistry becomes fairly uniform across grain sizes. This suggests that the temperature distribution may be most important when the grain temperature approaches a threshold temperature for an important surface reaction, e.g. the 12 K threshold for efficient formation of CO_2 from CO.

3.3.5 Chemical Evolution - Collapse Model

Figure 3.1(d) shows the grain size and temperature evolution for model 5G_COLL. The dust temperature for this model is determined by the power law $T_d \propto a^{-1/6}$, which is normalized to the temperature of a 0.1 μm grain, as determined by the visual extinction at any moment in the model run (Garrod & Pauly, 2011). The time of highest rate of collapse in the model can be seen in the

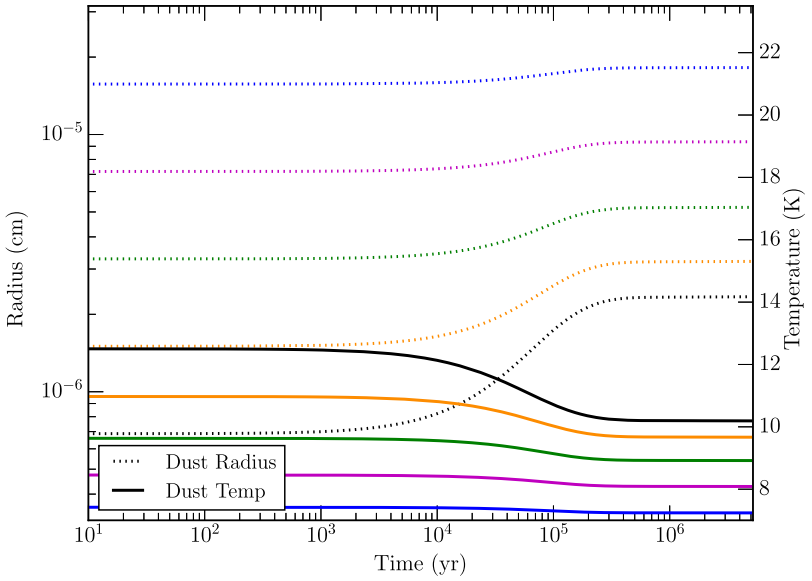

(a) 5G_T8_DIST

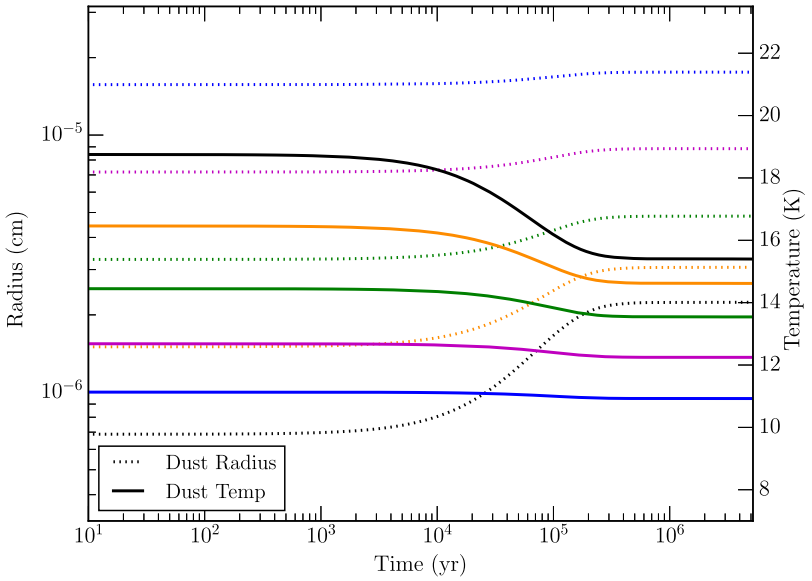

(b) 5G_T12_DIST

Figure 3.6: Grain size and temperature evolution for the 8 K and 12 K models including a temperature distribution across five grain sizes. The size variation between the two models is fairly similar, indicating that the difference in temperature does not strongly affect accretion rates (and therefore temperature evolution, relative to the starting temperature.)

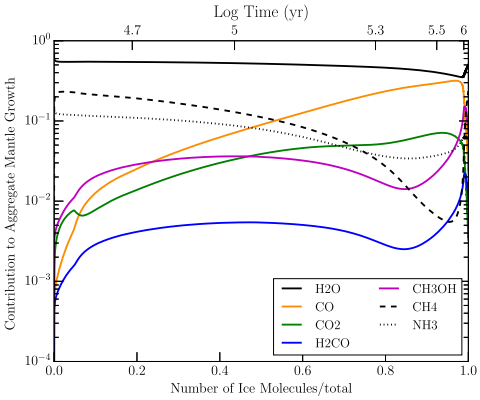

(a) Aggregate Ice Mantle

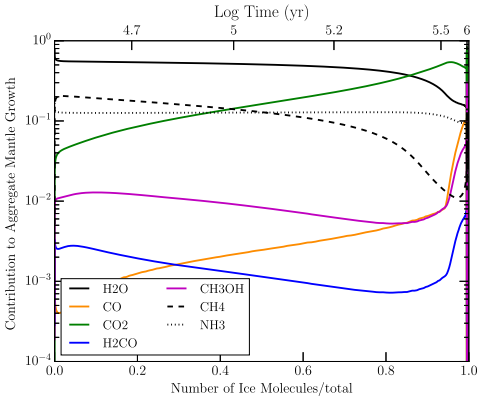

(b) Aggregate Ice Mantle

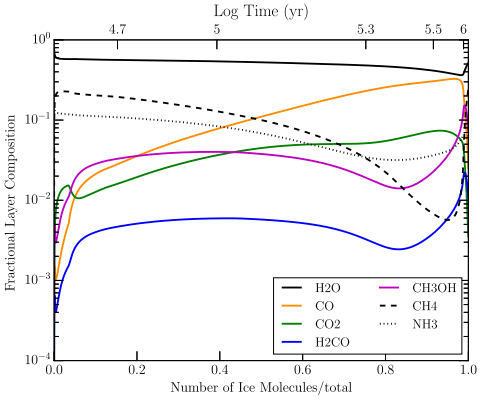

(c) Grain Size 1

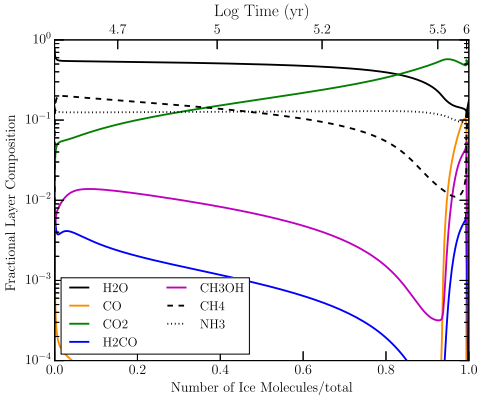

(d) Grain Size 1

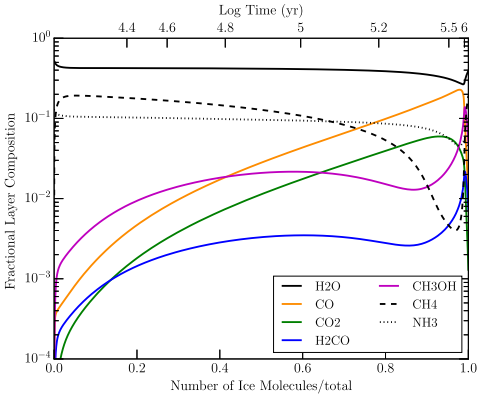

(e) Grain Size 5

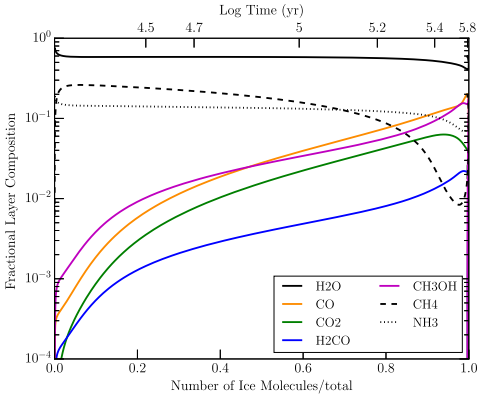

(f) Grain Size 5

Figure 3.7: Chemical evolution for models 5G_T8_DIST (left column) and 5G_T12_DIST (right column). Strong differences are present between all three temperature distribution models.

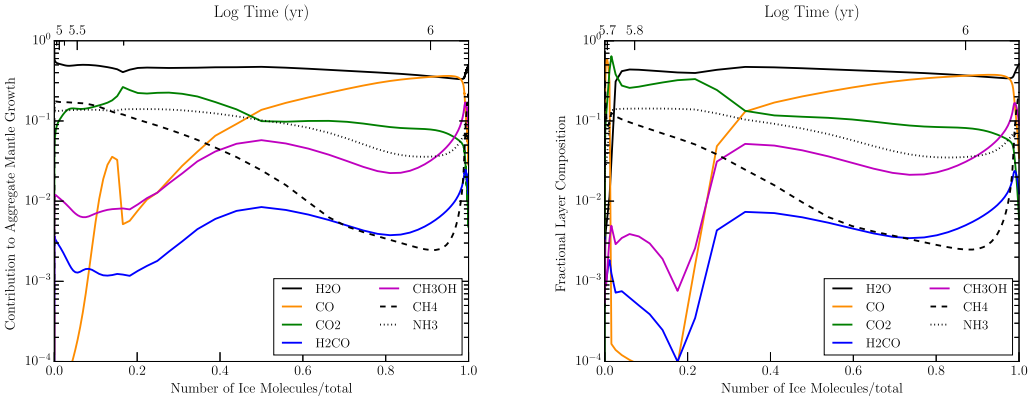

(a) Aggregate Ice Mantle

(b) Grain Size 1

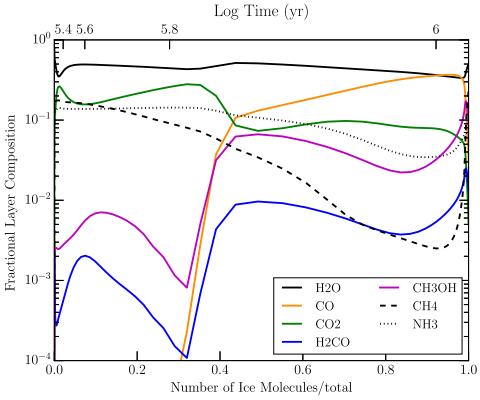

(c) Grain Size 2

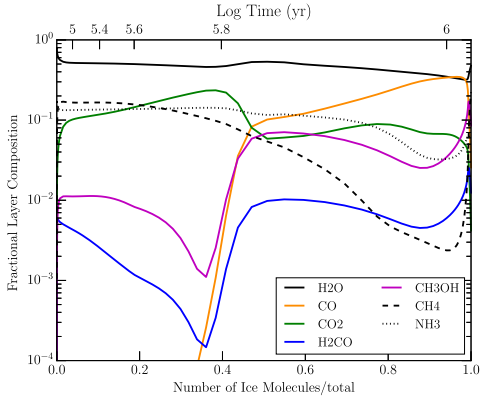

(d) Grain Size 3

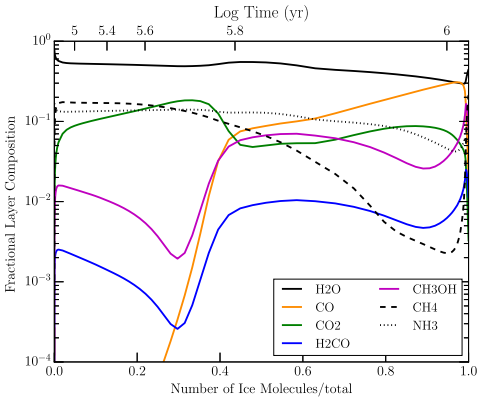

(e) Grain Size 4

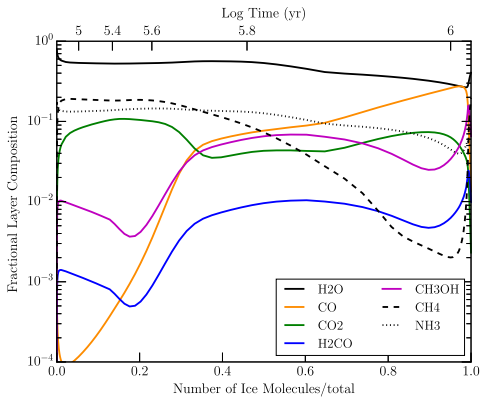

(f) Grain Size 5

Figure 3.8: Chemical evolution for model 5G_COLL. The upper left panel shows the evolution of the aggregate ice mantle, while the other panels show the evolution for the smallest grain (1) to the largest grain (5).

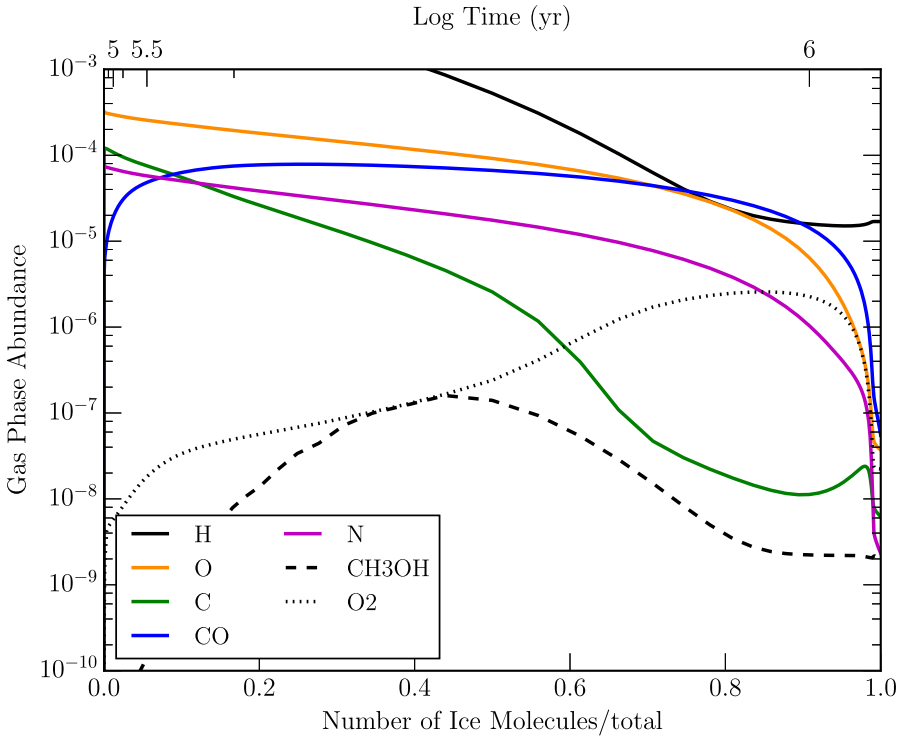

Figure 3.9: Gas-phase chemical evolution for model 5G_COLL, with abundances relative to n_H.

figure as the time at which most accretion occurs, around 6×10^5yr. Prior to the main collapse phase, the small grains are much hotter than in any of the static-cloud models. Post-collapse, the grain temperatures are comparable to the final temperatures for model 5G_T8_DIST, see Figure 3.7.

The chemical evolution of the collapse-model grain mantles is shown in Figure 3.8. Cusp-like features are present in the aggregate mantle plot due to the rapid changes in surface chemistry during the collapse. Prior to collapse, the dust temperature of the smallest grains is greater than 20 K. At this temperature, accreted atomic hydrogen and oxygen quickly desorb, and the time spent on the grain surface is not sufficient to produce OH efficiently. During this stage, the surface is predominantly covered with CO. However, once the small grains

drop below 19 K, atomic oxygen remains on the surface long enough to react with atomic hydrogen to form OH, and OH concentration jumps by eight orders of magnitude. Surface CO is then efficiently converted to CO_2 via CO + OH. This transition in behavior can be seen in Panel 3.8(a) where CO shows a peak in fractional layer abundance near 15% of total ice deposited. Past the peak, the contribution to aggregate CO fraction from grain one becomes negligible, as its CO is efficiently converted into CO_2. After the majority of the collapse has taken place and the temperature drops further, the smallest grain drops below 12 K, the temperature required for efficient CO_2 production. The aggregate mantle returns to a CO_2/CO ratio $<$1.

The evolution of selected gas-phase species is shown in Figure 3.9. The gas-phase evolution has not changed considerably from the models of Garrod & Pauly (2011). The largest difference occurs in methanol, with elevated abundances in the current 5G_COLL model. Methanol is produced on grains surfaces, but a fraction ($<$1 %) is returned to the gas phase through the reactive-desorption mechanism (Garrod, Wakelam & Herbst, 2007). Gas-phase methanol abundance is highly sensitive to the barriers set for hydrogen abstraction from surface methanol by atomic H. The more rapid abstraction produced in this model results in more CH_3O/CH_2OH, which quickly recombines with H, resulting in more methanol desorption. The methanol desorbed into the gas phase is nevertheless only a small fraction of the total produced on the grains.

Compared to 5G_T10_DIST, the general composition of the aggregate mantle has been enriched in CO and depleted in H_2O and CH_4. CO_2 abundance is comparable in both models, indicating the mean dust temperature during collapse is somewhat similar to the DIST model. Gas-phase abundances of grain-surface

products closely follow their production due to desorption of surface species. Gas-phase CO_2 peak abundances are comparable in 5G_COLL and 5G_T10_DIST models, though final collapse values are greatly reduced due to a decrease in surface abundance, coincident with the decrease in grain temperature.

Methanol formation in the collapse model is fairly stable, showing the largest variation when a grain crosses from CO_2-dominated to CO-dominated surface composition. With abundant surface CO, the hydrogenation chain to CH_3OH occurs more frequently. The grains in the collapse model spend the majority of time under 12 K, which leads to comparable methanol abundances to the UNIF models with $T \lesssim 12$ K.

3.3.6 Effect of Discretization and Number of Grain Sizes

To test the effects of discretizing the grain size distribution and to determine if five grain sizes are sufficient to reproduce the effects of a continuous distribution, we use models with various numbers of grain sizes. The number of grain sizes is used to bin the power law from Equation 3.2, with calculated grain abundances given in Table 3.4. Shown in Table 3.5 are the results of collapse models ranging from two grains to eleven. Figure 9 shows the aggregate mantles of the models for comparison. The effects of discretizing the grain size distribution are seen in the abundance discrepancies for the two and three grain models. Note that the number of peak-like deviations of CO at early time correspond to the number of grain sizes that start at a dust temperature too high for atomic oxygen to form OH on the surface. Beyond five grains, the differences in species abundances drop to minimal levels. This supports a choice of four or five grains to

N_b	GD_{gr1}	GD_{gr2}	GD_{gr3}	GD_{gr4}	GD_{gr5}	GD_{gr6}	GD_{gr7}
1	5.694×10^9	5.737×10^9	5.921×10^9	6.234×10^9	6.632×10^9	7.081×10^9	7.564×10^9
2	-	7.628×10^{11}	1.542×10^{11}	7.189×10^{10}	4.689×10^{10}	3.614×10^{10}	3.059×10^{10}
3	-	-	4.018×10^{12}	8.289×10^{11}	3.316×10^{11}	1.845×10^{11}	1.237×10^{11}
4	-	-	-	9.558×10^{12}	2.345×10^{12}	9.415×10^{11}	5.001×10^{11}
5	-	-	-	-	1.658×10^{13}	4.805×10^{12}	2.022×10^{12}
6	-	-	-	-	-	2.453×10^{13}	8.178×10^{12}
7	-	-	-	-	-	-	3.307×10^{13}

Table 3.4: Gas-to-dust ratios, calculated as the number of hydrogen atoms to the number of grains, for classes of models with a given number of grain sizes. Each column presents values from a single model, with the gas-to-dust ratio for a given size category read from the rows, i.e. the smallest grain in each model is the first row and the largest grain in the last non-empty row.

Model	H_2O	CO	CO_2	CH_3OH	H_2CO	CH_4	NH_3
2G_COLL	1.485(-4)	35.4	30.6	7.29	1.10	11.1	21.6
3G_COLL	1.508(-4)	34.9	29.4	7.37	1.13	11.5	21.5
4G_COLL	1.513(-4)	33.9	29.7	7.32	1.12	12.0	21.7
5G_COLL	1.507(-4)	34.1	30.0	7.33	1.12	11.9	21.8
6G_COLL	1.506(-4)	34.2	30.0	7.37	1.13	11.8	21.7
7G_COLL	1.507(-4)	33.9	30.2	7.35	1.13	12.0	21.8
11G_COLL	1.460(-4)	34.1	31.0	7.32	1.13	11.8	21.8

Table 3.5: Mantle abundances at 5×10^6 years for models with varying numbers of grain sizes. The value of H_2O listed is with respect to total atomic hydrogen abundance, while the values for other species are given with respect to the H_2O abundance.

capture the complexity of the size distribution while minimizing computational runtime.

3.4 Discussion

The behavior of models with uniform temperature across a grain-size distribution shows surprising similarity to the single grain counterparts, indicating that simply introducing the distribution without any associated change in temperature has little effect on the chemistry.

A fraction of surface reactions are well-modeled with rate equations, while the rest are altered by stochastic effects. The cross-sectional area of a dust grain is used to calculate the accretion rates for gas-phase species; if the surface population of all reactants drops to of order unity, the modified rate equations are used. These modifications were the primary mechanism expected to alter the surface chemistry for the class of models with uniform temperature.

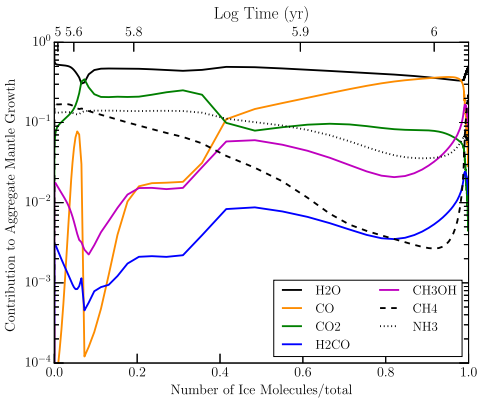

(a) 2 Grains

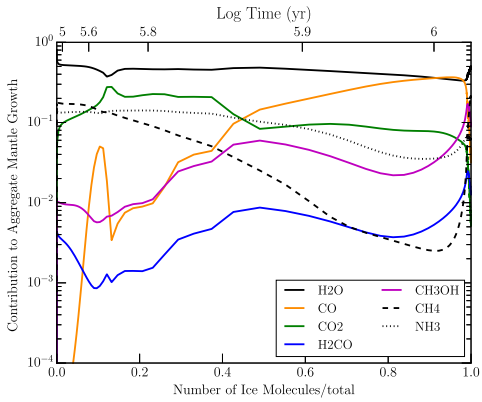

(b) 3 Grains

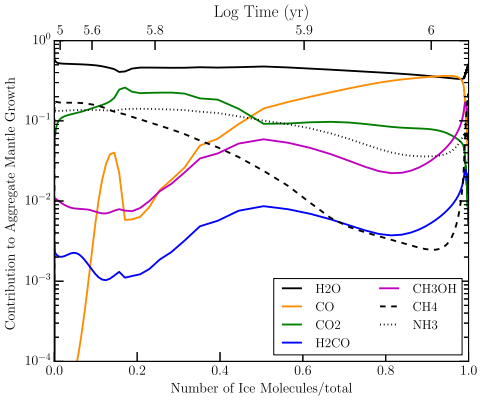

(c) 4 Grains

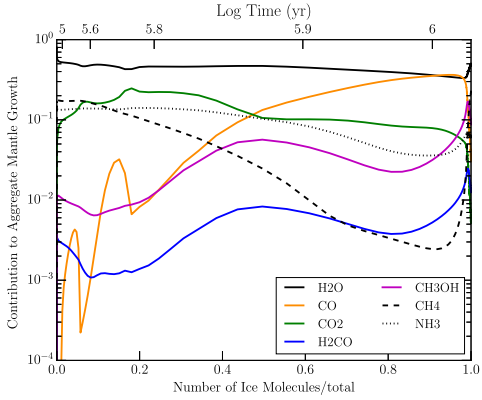

(d) 6 Grains

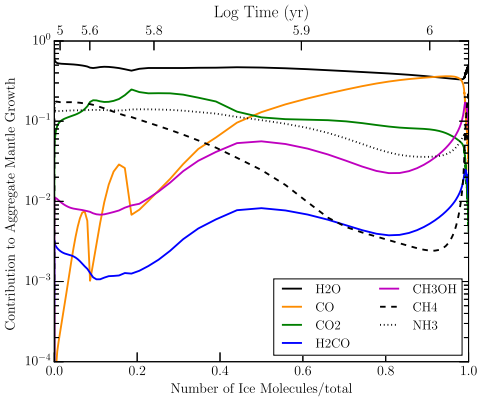

(e) 7 Grains

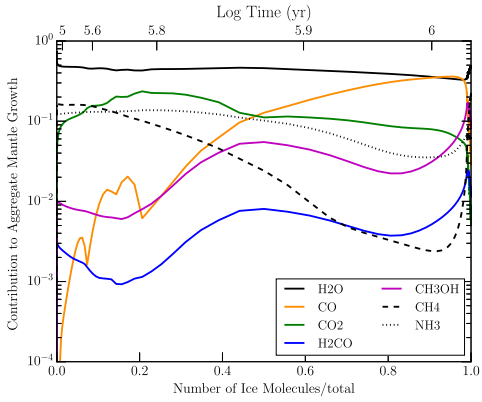

(f) 11 Grains

Figure 3.10: Aggregate mantles for collapse models with varying numbers of grain sizes.

The models find the same rate treatment is appropriate for a given reaction on all grain sizes, for nearly all (~90%) surface reactions. There are quantitative differences in ice composition between the grain sizes in the UNIF models; however, these differences follow a relationship that is reasonably reproduced by a single grain size model. This is shown in Table 3.3 by comparing single grain models to UNIF models with equal temperature. Grain-size-dependent behavior is observed in the UNIF models as an increase in the abundance of the hydrogenated species CH_4 and NH_3 with increasing grain size. This occurs due to the stochastic nature of the hydrogenation reactions; the intermediate steps from atomic carbon and nitrogen to their hydrogenated forms are rate-limited by the accretion of hydrogen, which is larger for grains with a larger cross section.

The inclusion of a temperature distribution across grain sizes creates a more varied composition across the grain sizes. The conversion of CO to CO_2 occurs via an efficient pathway above a threshold temperature of $\sim$ 12K. CO is strongly depleted for grains with a temperature above this threshold, and CO_2 is the primary carbon-bearing surface species. Correlation of H_2CO and CH_3OH abundances to CO abundance follow from their formation via CO hydrogenation; the low abundance of CO on small, warm grains causes a depletion in methanol on those grains. It should be noted that in absolute quantity, the smallest grains still possess the most methanol, due to their greater total number and summed cross section; rather, it is a depletion in the amount of methanol ice when expressed as a fractional abundance with respect to water ice.

The collapse models explore higher temperatures at early times on the smallest grains, shown in Figure 3.1(d). The accretion closely follows the collapse, oc-

curring as a burst rather than a sustained rate. The aggregate mantle plots have cusp-like behavior due to grain temperatures rapidly decreasing during collapse, with the most pronounced compositional changes on the smallest grains. At early times the smallest grains are sufficiently warm that atomic species do not have time to react before desorbing. As the collapse proceeds, accretion rates increase and the dust temperature drops. Once a dust temperature of 20 K is reached, $O + H \rightarrow OH$ becomes competitive as a sink for atomic oxygen, and the binding energy of OH is large enough to secure it on the grain surface. Through reaction with OH, surface CO abundance sharply plummets to a value of order unity; the less-efficient modified rate prevents CO + OH from further reaction. This is seen in the aggregate mantle plot 3.8(a) as a sharp dip in fractional layer abundance of CO. CO_2 is efficiently formed until the dust temperature crosses the 12 K threshold.The initial temperature of the largest grains in the 5G_COLL model is sufficiently low that atomic species readily stick to the surface. The elevated abundance of atomic hydrogen creates an enrichment of hydrogenated species - H_2O, CH_4, and NH_3.

The set of collapse models with varying numbers of grain sizes points to the threshold temperature detailed above. For less than five grain sizes, only the smallest grain size in a given model is too hot for atomic species to react. For six to ten grain sizes, there are two, while the eleven grain model shows three grains with a thin surface layer of accreted CO at early time. Examining the aggregate mantle abundances, all models agree to 5% accuracy for most major species. Five grains was chosen for models as a compromise between optimal sampling of the grain size distribution and computational complexity.

When comparing the grain size distribution models to those with a single

grain size, the primary effects we expect to see should be evident of a difference in chemistry on the small, hot grains versus the large, cool grains. These effects are muted in the UNIF and DIST models because the small grains dominate the distribution of cross-sectional area; in the 5G_T10_DIST model, nearly 60% of total grain species are found on the smallest grain, and 80% on the two smallest grains. However, the difference is more pronounced in the 5G_COLL model. With grain temperatures above 20 K, the two smallest grains fail to retain significant surface species until collapse. During this time, the third grain size has the most grain species, at around 42%. Post-collapse, the two smallest grains grow substantially and hold roughly 70% of grain species.

The high-temperature desorptive effect serves to hinder observational differentiation between single-grain and multi-grain models; the change in chemistry we might expect to see on small grains is absent, because their surface does not allow for adsorbed species to efficiently react. The dominant grain mantle is the warmest surface under 20 K, which will preferentially form CO_2 ice over CO ice if that surface is above 12 K. Observational constraints may be more forthcoming when considering grains in a post-collapse warm-up phase associated with hot cores in the star formation process, where more refractory species are found initially on grain surfaces. Even though in the denser conditions of a hot core, it is likely the dust and gas temperatures would be well coupled, flattening out the temperature distribution across the grain sizes, the enriched state of the smaller grains could be enhanced by the thin nature of ice mantles on the smallest grains; the top layer of the smallest grains in the 5G_COLL model contains 5.1% of the total ice, and 43.4% of the ice is found in the uppermost ten layers. A significant fraction of the mantle could then be involved in surface chemistry such as diffusion, reaction, and desorption. It is worth noting that the heating

of small grains can be stochastic, and the time variation of small grain temperatures can be extreme for the smallest grains (see Cuppen, Morata & Herbst, 2006).

We therefore suggest that, under diffuse to translucent conditions where grain mantles are beginning to form, the smallest grains should be essentially bare, with substantial proportions of the ice abundance stored on the mid-size to large grains. This balance should shift during cloud collapse so that small grains hold the majority of ice material, albeit in thinner ice mantles than are formed on the larger grains.

Past work (Garrod & Pauly, 2011) found a similar temperature threshold for CO_2 production; the model results were interpreted as an explanation for the abundance of polar and apolar CO and CO_2 ices at varying temperatures in dark clouds (for observations, see Whittet et al., 2009; Cook et al., 2011). This interpretation is not changed by the results of these grain-size distribution models. The effect of forming CO_2-rich, CO-poor mantle layers at high temperature is still present, as is the CO/CO_2 abundance ratio of 2-4 at temperatures lower than 12 K. It should be noted that the collapse models end at a density equivalent to that found in dark clouds ($n_H = 4{\times}10^4$ cm^{-3}), by which point gas-phase CO is not fully depleted. In some sources, significantly greater gas densities may be achieved, with correspondingly higher CO depletions.

The most important attributes (assumptions) of the distribution are how the cross-sectional area is distributed across grain sizes and how the temperature of grains is determined. For the Mathis power law, the *area* is distributed as $\frac{dX_{tot}}{da} \propto a^{-1.5}$, placing the majority of accretion onto small grains. This smoothes the power law into a flatter effective distribution as small grains accrete, shown

in the initial and final radii in Table 3.2. Future work will consider more complex grain distributions, like those of Weingartner & Draine (2001). Distributions that place the majority of grain surface area on large grains could affect the aggregate chemistry. The temperature distribution assumes that the grains are heated by an ambient radiation field and that the dust absorption efficiency is unity across all grains, allowing a simple relationship between the temperatures of each grain size to be assigned. Future modeling will take into account explicitly the optical properties of each grain size, although a full treatment of stochastic heating of the smallest grains is unlikely to be achievable using a rate-based gas-grain chemical model.

3.5 Conclusions

We summarize our main conclusions from this study:

- Inclusion of a grain size distribution with uniform grain temperature does not strongly affect the model at dark cloud temperatures and densities, despite the inclusion of modified rates. This reinforces the results of Acharyya (2011).
- Consideration of a grain temperature distribution causes variation in ice production between grain sizes, with CO_2 ice favored over CO above 12 K. The small grains are warmest and most abundant, leading to an increase in CO_2 ice when comparing models with a dust-temperature distribution against models that use a uniform dust temperature.
- The collapse model shows unique behavior due to low initial A_v and high initial temperatures on the smallest grains. Above 20 K, accreted atomic

species desorb before reacting with other surface species, with only heavy molecular species like CO bound to the surface. As the collapse proceeds, grain temperatures decrease as density increases and ice mantles grow. This leads to a transitory period of CO_2 enrichment, similar to models of Garrod & Pauly (2011).

- The majority of grain-surface ice material resides on the smallest grain populations, under low temperature/high extinction conditions, due to the greater size of this population. Under more diffuse conditions where the small-grain temperatures exceed 20 K, the main carrier of the ice mantles, such as they are, will be the medium-sized grains.
- The collapse models produce an ice mantle on the dust grains, with a varying thickness from 40 to 100 monolayers, from the smallest to largest grains. On the smallest grains the mantles are thin, and 43% of the total ice is present in the uppermost ten layers; these species are more readily available for surface chemistry, leading to a possible enrichment in chemical complexity during a warm-up phase following the collapse.
- The number of grain sizes chosen in the discretization of the size distribution shows only a small chemical effect. The representative grain radius may need to be reduced from 0.1 μm to 1G model values to better represent the Mathis (1977) distribution. Observable effects may be more pronounced if small grains are allowed an initial reservoir of refractory molecular species in a core warm-up model.
- The inclusion of a grain-size distribution is a general improvement for chemical models with variable temperature and density. The distribution in size and temperature captures the changing environment experienced by chemical species during the collapse to a dark cloud. For static models,

the use of a grain size distribution is less critical; the effects of the distribution can be recreated by a single-grain model with decreased grain radius and elevated grain temperature, due to the weighting effects of the grain size distribution assumed here.

CHAPTER 4

MODELING ICES IN MAGELLANIC CLOUD YSOS

4.1 Introduction

Much of our understanding about the details of star formation comes from investigations of stars and the interstellar medium (ISM) in the galaxy, yet the peak of star formation occurred in the past at lower metallicity (Madau & Dickinson, 2014). The Magellanic Clouds, local dwarf satellites of the Milky Way, provide an astronomical laboratory to study the process of star formation in a metal-poor environment. Comparison studies between sites of star formation in the Magellanic Clouds and the Milky Way can illuminate the metallicity dependence of local physical processes via observational tracers such as molecular emission and absorption features. Knowledge of multiple molecular abundances can begin to separate effects of metallicity from local physical parameters, e.g. the radiation environment and the dust temperature.

Mid-infrared spectral observations of embedded young stellar objects (YSOs) in the Milky Way (MW) have found a wealth of solid-state features, showing high column densities of ices such as H_2O, CO, CO_2, and CH_3OH (Gerakines et al., 1999; Gibb et al., 2004). H_2O is the most abundant ice, with a typical column density of order 10^{-4} with respect to total hydrogen; CO_2 is next, at an average value of CO_2:$H_2O \simeq 0.2$ (Boogert & Ehrenfreund, 2004). CO and CH_3OH ices follow at lower abundance, though with nearly an order of magnitude of variation between lines of sight. These ices are found in the dense, cold envelopes surrounding the luminous central source, and they hold information

This chapter is an adapted version of the submitted article [[citetPauly2017]].

on the collapse history of the progenitor dense molecular cloud via e.g. the polar to apolar ratio of the CO and CO_2 ice features (Gibb et al., 2000). They are processed to some extent by the internal radiation source, yet a complete explanation for the variation in observed galactic YSO ice abundances is not in hand. Local environment likely plays a role, with changes in the nearby interstellar radiation field (ISRF) or the cosmic ray ionization rate affecting gas and grain surface chemistry. Additionally, variations in the underlying elemental abundances of the collapsing cloud will influence the general chemistry and total ice column density.

Observations of massive YSOs (MYSOs) in the nearby Magellanic Clouds show a marked difference in ice abundances with respect to galactic counterparts (van Loon et al., 2005; Oliveira et al., 2009, 2011, 2013; Shimonishi et al., 2008, 2010, 2016a). Shimonishi et al. (2010) and Oliveira et al. (2011) have detected H_2O, CO and CO_2 ice in massive YSOs in the Large Magellanic Cloud (LMC); they found bulk compositional differences in LMC sources compared to their galactic counterparts, shown in elevated CO_2 ice or depleted H_2O ice, with an average value for CO_2:H_2O of 0.32. Oliveira et al. (2011, 2013) found only an upper limit for CO ice in all Small Magellanic Cloud (SMC) sources studied, with abundances (with respect to their H_2O columns) a factor of three to ten lower than their galactic counterparts. Oliveira et al. (2011) and Shimonishi et al. (2016a) provided additional near-infrared spectra of a sample of LMC MYSOs, with detections or upper limits for CH_3OH ice towards all sources studied.

In addition to ice abundance variations, the properties of gas and dust in the Magellanic Clouds also differ from their galactic counterparts. A significant fraction of molecular gas in galaxies like the metal-poor Magellanic Clouds re-

side in a CO-dark phase, where an extended photo-dissociation region keeps all atoms but hydrogen in atomic form (Madden et al., 2012; Madden, Cormier & Rémy-Ruyer, 2016; Roman-Duval et al., 2014). LMC dust temperatures are elevated; Bernard et al. (2008) used *Spitzer Space Telescope* data to find a globally-averaged value of 21.4 K, or 23 K in the 30 Dor region. They also performed spectral energy distribution (SED) fitting with a variable ISRF, finding that increasing ISRF strength by a factor of ~ 2.1 best fits average LMC observations. Galametz et al. (2013) analyzed data from *Spitzer, Herschel* and the *Large Apex Bolometer Camera* to better model the sub-millimeter component of the dust SED. Their best-fit dust temperature for the N158-N159-N160 region of the LMC is 27 K.

Dust temperatures in the SMC have been measured towards H II regions and YSOs. Towards N27, a bright H II region in the SMC bar, Caldwell (1997) finds dust temperatures of 33-40 K, while Heikkilä, Johansson & Olofsson (1999) finds a similar range of 35-40 K. van Loon et al. (2010) use observations of YSOs in the Magellanic Clouds to find dust temperatures of 37-51 K in the SMC versus 32-44 K in the LMC. Chiar et al. (1998) finds dust and ice temperatures in galactic YSO counterparts to be generally less than 30 K, with some measurements of 23-25 K.

We lack detailed measurements on the ISRF of the Magellanic Clouds; apart from the ISRF fitting of Bernard et al. (2008) in the LMC, Vangioni-Flam et al. (1980) and Pradhan, Murthy & Pathak (2011) provide evidence for a factor of 4 to 10 increase in the UV and far-UV field strength in the SMC when compared to the solar neighborhood.

Chemical models by Garrod & Pauly (2011) found that dust temperatures

can strongly affect the abundances of key grain surface molecules. Above dust temperatures of ~ 12 K, grain surface diffusion of CO becomes rapid, and the reaction CO + OH → CO_2 + H efficiently produces CO_2. The authors also presented a gas-grain model with free-fall collapse which reproduced the threshold visual extinctions for detection of H_2O, CO_2 and CO ices. In this work, we will utilize a similar approach for an investigation of ice abundances towards YSOs in the low metallicity environments of the LMC and SMC.

We collate observations of MYSOs for which H_2O, CO, CO_2 and CH_3OH detections or upper limits are available, excluding CH_3OH for SMC sources (toward which no measurements of CH_3OH have yet been achieved). Table 4.1 lists the total sample we will use for model comparison. Figure 4.1 shows the observations from Table 4.1 in a ternary H_2O:CO_2:CO ice diagram. The ternary plot describes the relative abundances of this three-component ice system. Importantly, we also consider methanol (CH_3OH) ice, a key component for galactic YSOs and now detected toward some LMC MYSOs. To include this fourth component on a ternary diagram, we include a second point for those sources with methanol detections or upper limits; these points show the fractional abundance of H_2O:CO_2:(CO+CH_3OH). This pairing choice of (CO+CH_3OH) is chemically motivated, as CH_3OH is primarily formed from the successive hydrogenation of CO on grain surfaces (Watanabe & Kouchi, 2002; Watanabe, Shiraki & Kouchi, 2003; Watanabe et al., 2004; Fuchs et al., 2009; Cuppen et al., 2009). The figure shows a transition in composition, with some blending between some LMC and galactic sources.

Using the single-point free-fall collapse model detailed by Garrod & Pauly (2011) and Pauly & Garrod (2016), we investigate parameters responsible for the

chemical variation amongst MYSOs in the galaxy, LMC and SMC. We take the elemental abundances and dust temperatures to be the parameters of interest for the model study. We describe our model methods and parametrization in §2; results of the model grid are shown in §3; discussion of the results and additional parameters of interest are presented in §4; §5 concludes the study with some thoughts on future work.

4.2 Methods

We use the gas-grain chemical code MAGICKAL and its associated chemical network, first presented by Garrod (2013) and updated by Pauly & Garrod (2016) to include a grain-size distribution consisting of five grains. The model features 475 gas-phase species and 200 grain surface species with a network of roughly 9000 reactions and processes. Grain surface species are tracked in two separate phases, surface and mantle; the surface species participate in desorption, reaction and diffusion across grain sites, while the ice mantle is treated as a separate phase that is coupled to the surface. Bulk diffusion in the mantle ice is treated explicitly, allowing reactions within the mantle, as well as exchange between surface and mantle components; however, for the low temperatures involved in this work we treat the mantle phase as inert except for the transfer of surface material into the bulk, as the mantle grows. The model uses the modified-rate approach detailed in Garrod (2008) (method "C") to account for possible stochastic effects in the surface chemistry. The chemical network also includes photo-dissociation and photo-ionization processes, with photons sourced either from the ambient field or the cosmic ray-induced UV field.

	Source	H_2O	CO	CO_2	CH_3OH
MW	Mon R2 IRS 2[ac]	77.1%	5.8	13.0	4.1
	RAFGL989[ad]	62.7	12.6	22.7	2.0
	RAFGL2136[acd]	76.5	4.5	13.1	5.9
	RAFGL7009S[ade]	59.0	9.5	13.0	18.5
	W33 A[acd]	74.2	5.4	8.6	11.8
	NGC 7538 IRS1[ae]	73.3	6.0	17.0	<3.7
	NGC 7538 IRS9[acd]	66.5	12.4	16.9	4.2
	W3 IRS 5[ade]	83.7	2.4	10.5	<3.4
LMC	ST1[b]	69.0	11.4	16.4	<3.3
	ST2[b]	77.2	<2.1	15.7	<5.0
	ST3[b]	73.8	3.2	21.7	<1.3
	ST4[b]	67.5	4.6	24.4	<3.5
	ST5[b]	72.2	3.4	20.3	<4.1
	ST6[b]	60.8	<14.7	21.1	3.4
	ST7[b]	60.8	3.3	32.9	<2.9
	ST10[b]	67.2	10.7	19.6	2.5
	ST14[b]	73.9	8.7	11.8	<5.6
	ST16[b]	76.9	<7.8	10.6	<4.7
SMC	IRAS 00430–7326[f]	88.3	<1.3	10.4	...
	S3MC 00540–7321[f]	85.4	<0.8	13.8	...
	S3MC 00541–7319[f]	80.0	<0.6	19.4	...
	IRAS 01042–7215[f]	94.6	<2.6	2.8	...

Table 4.1: Fractional ice columns for observed high-mass young stellar objects in the Milky Way, Large Magellanic Cloud and Small Magellanic Cloud. The abundance of each species is shown relative to the sum of the four column densities, in percent.[a]: Gibb et al. (2004), [b]: Shimonishi et al. (2016a), [c]: Brooke, Sellgren & Geballe (1999), [d]: Boogert et al. (2008), [e]: Dartois et al. (1999), [f]: Oliveira et al. (2013)

4.2.1 Physical Model

The updated MAGICKAL code utilizes a grain size distribution. Following Pauly & Garrod (2016), we adopt the power-law fit to the size distribution of

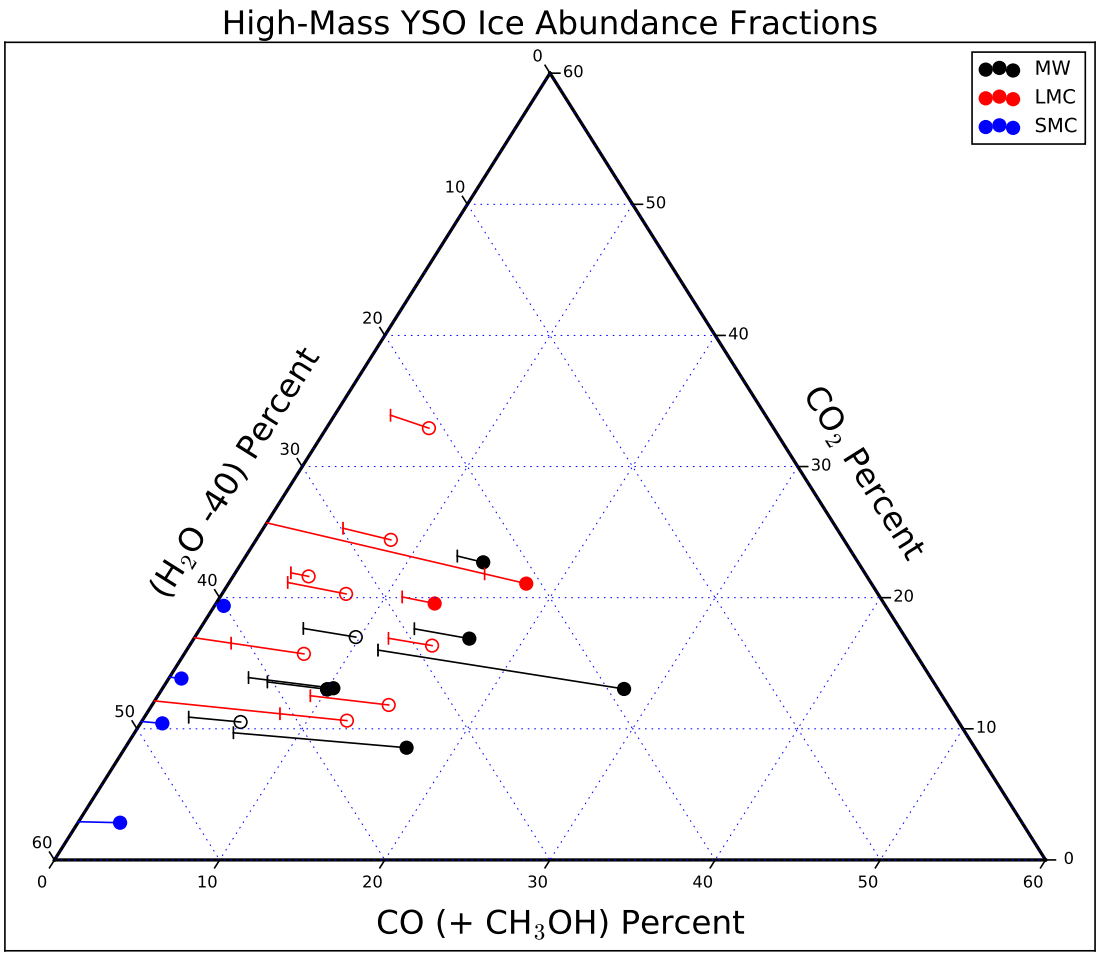

Figure 4.1: The relative abundances of the four major ices in massive young stellar objects in the Milky Way (black), LMC (red), and SMC (blue). SMC sources have only upper limits on CO and no information on CH_3OH; SMC points show the composition at the upper limit value with a line drawn to zero CO abundance. For LMC and Milky Way sources, the vertical tick shows the H_2O:CO:CO_2 composition, while the circles show the composition including CH_3OH ice as H_2O:(CO+CH_3OH):CO_2. For LMC sources with only an upper limit on CO, lines have been drawn to zero CO abundance, while sources with an upper limit on CH_3OH ice have an open circle. (Ternary figure style from Harper et al., 2015)

silicate grains in the ISM provided by Mathis, Rumpl & Nordsieck (1977), which follows the relationship $dn/da = Ca^{-3.5}$. Upper and lower limits to the distribution adopted in the model, as well as the power law constant are given in Table 4.2. The upper limit from Mathis, Rumpl & Nordsieck (1977) is loosely constrained by extinction curve measurements, while the lower limit is a practical

modeling constraint imposed by stochastic single-photon heating of very small dust grains (Cuppen, Morata & Herbst, 2006). At sizes smaller than roughly $\sim 0.02\mu$m, grains experience single photon heating to temperatures sufficient to desorb surface species at time scales shorter than accretion rates; therefore, they are not expected to contribute significantly to ice-mantle formation. The power law constant is taken from Draine & Lee (1984), though it is scaled down to match the original gas-to-dust ratio; this is required due to our shift in a_{min} and a_{max} from the values given by Mathis, Rumpl & Nordsieck (1977).

We assume a spherical shape for grains, with the cross-sectional area as $\sigma = \pi a^2$. We discretize the grain size distribution into five bins, equally spaced in $\log(\sigma)$. For each bin, i, the mean cross-sectional area of grains in the bin, $\langle \sigma_i \rangle$, is calculated via the power law. This σ and its associated radius are used as representative values for all grains in that bin.

Parameters	Values
Initial n_H	3×10^3 cm^{-3}
Final n_H	2×10^4 cm^{-3}
Initial A_V	3.00
Final A_V	10.627
Final time	5×10^6 yr
T_{gas}	10 K
a_{min}	0.02 μm
a_{max}	1.00 μm
Power law constant	4.436×10^{-26} cm$^{2.5}$/H
Cosmic ray ionization rate	1.3×10^{-17}s^{-1}

Table 4.2: Model Physical Parameters

The power law constant determines the total abundance of dust. Roman-Duval et al. (2014) measured the gas-to-dust ratio in the LMC, finding a range

of 160 to 500 for the dense to diffuse ISM, compared to 100 to 250 for the Milky Way. We follow Acharyya & Herbst (2015) and use a value of 175; this value is fixed for all models.

The power law exponent from Mathis, Rumpl & Nordsieck (1977) concentrates cross-sectional area in grains with the smallest radius, which are more numerous, whereas dust mass and volume are concentrated in the largest, least-populous grains. Small grains will drive the bulk surface chemistry due to concentrated accretion cross-section.

4.2.2 Collapse Method

We use free-fall collapse to simulate the density of the YSO envelope, using the methods presented by Garrod & Pauly (2011), following Spitzer (1978) and Brown, Charnley & Millar (1988). The density increases following:

$$\frac{dn}{dt} = \left(\frac{n^4}{n_i}\right)^{1/3} \left\{ 24\pi G m_H n_i \left[\left(\frac{n}{n_i}\right)^{1/3} - 1 \right] \right\}^{1/2} \tag{4.1}$$

with n_i the initial density, G the gravitational constant, and m_H the mass of a hydrogen atom. Initial and final densities and visual extinctions are given in Table 4.2, where the final visual extinction is not a parameter but is determined from the other three parameters via the relation $A_V = A_{V,0}(n_H/n_{H,0})^{2/3}$.

4.2.3 Dust Temperatures

We model the evolution of dust temperature as a function of the visual extinction and dust radius, following methods outlined in Garrod & Pauly (2011).

We add an additional variable in a model-dependent interstellar radiation field (ISRF). With dust heating from the ISRF equal to cooling from dust radiation, we solve:

$$\int_0^\infty Q_\nu J_\nu D_\nu \left(A_V\right) d\nu = \int_0^\infty Q_\nu B_\nu \left(T_d\right) d\nu \tag{4.2}$$

where Q_ν is the frequency-dependent efficiency of absorption or emission, J_ν is the radiation field intensity incident on the cloud edge, $D_\nu \left(A_V\right)$ is the attenuation of the radiation field at a given frequency for a given A_V, and $B_\nu \left(T_d\right)$ is the Planck function. We use the assumption from Krügel (2003) for the right-hand side of Equation 1, expressed in cgs units, valid for grains between the small- and large-grain limits, to find:

$$\int_0^\infty Q_\nu J_\nu D_\nu \left(A_V\right) d\nu = 1.47 \times 10^{-6} a T_d^6 \tag{4.3}$$

with a as the dust grain radius. We use tabulated data on line-of-sight extinction profiles with $R_V = 5$ from Cardelli, Clayton & Mathis (1989) and Mathis (1990) to determine $D_\nu(A_V)$. This approach assumes plane parallel geometry. The absorption efficiency of dust grains at wavelengths relevant to the ISRF is approximated as $Q_\nu^{abs} \propto a\lambda^{-1.5}$ with a maximum Q value of 2.0, a reasonable assumption for carbonaceous grains. Silicate dust has a more complex (and generally weaker) absorption behavior in the 0.1 - 10 μm range. Our treatment therefore implicitly considers only carbonaceous grains. Of note, we treat the growth of the ice mantle during model evolution as extra grain material and not explicitly as ice for the value of Q_ν^{abs}.

We approximate the ISRF in various environments by modifying the multi-component fit from Zucconi, Walmsley & Galli (2001) for the Milky Way. The fit includes contributions from three discrete stellar black-body populations, both hot and cool diffuse dust components, and the cosmic microwave background.

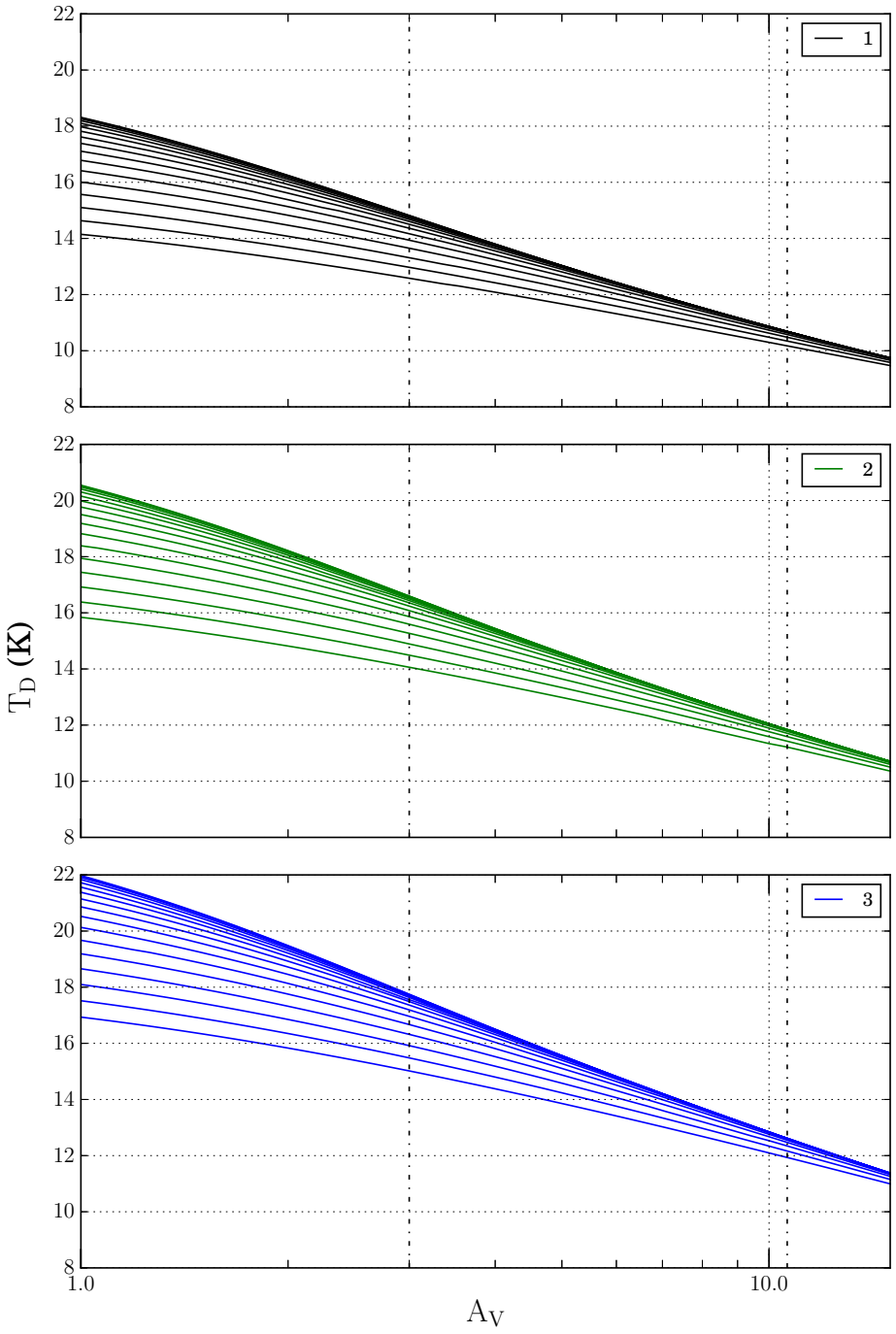

Figure 4.2: Tracks of dust temperature versus visual extinction with lines for dust grains of constant radius, from $a_{lower} = 10^{-1.7}\mu$m to $a_{upper} = 10^{-0.1}\mu$m; smaller grains have higher temperature. The top panel shows results for a stellar intensity factor of 1.0, the middle panel for 2.0, and the bottom panel for 3.0. Vertical dash-dotted lines indicate the span of A_V covered in our models' collapse.

To simulate variation in ISRF intensity in the Magellanic Clouds, we scale the stellar components uniformly, from the base factor of 1.0 to 3.0 in increments of 0.5. The resulting dust temperatures are shown in Figure 4.2 for a range of dust radii spanning the sizes explored in our models, with the smallest grains having the highest temperature. Note that the largest radius bin is $10^{-0.1}$ μm and not 10^{0} due to the discretization of the power law into five sizes in each model. The dashed vertical lines show the extent of A_V covered during the model collapse; the increase in A_V during the collapse process results in a general cooling and a flattening of the temperature distribution with respect to grain size.

The dust temperature tracks in Figure 4.2 are for grains of constant radius, but it should be noted that the effective grain radius is not constant during the model evolution; as gas species accrete and form an ice mantle, the grain radius grows, producing further cooling (see Pauly & Garrod, 2016).

The ISRF factor used to scale the dust heating is also used to scale the photo-ionization and photo-dissociation rates in the model, as the stellar component of the ISRF is the primary source of UV photons. Ionization and dissociation via the secondary UV field from cosmic rays are treated separately.

4.2.4 Elemental Abundances

To model the ISM of the metal-poor galaxies, we deplete the heavy elemental abundances in the initial setup of our models. The Magellanic Clouds have bulk metallicity of $Z_{LMC} \sim 0.4Z_{\odot}$ and $Z_{SMC} \sim 0.2Z_{\odot}$ (Russell & Dopita, 1992). Kurt & Dufour (1998) collated observations of eight LMC and six SMC HII regions with updated atomic transition data to find the mean abundances of carbon, nitrogen

Element	MW	LMC	SMC
H	5.000(-5)	5.000(-5)	5.000(-5)
H_2	0.499975	0.499975	0.499975
O	3.200(-4)	2.140(-4)	1.047(-4)
C^+	1.400(-4)	6.310(-5)	1.585(-5)
N	7.500(-5)	1.12(-5)	2.820(-6)
C/O Ratio	0.438	0.295	0.151

Table 4.3: Elemental abundances, listed with respect to total hydrogen number density, n_H. The first column represents galactic abundances, taken from Garrod & Pauly (2011). The second column is used as representative values for the LMC, taken from Peimbert (2003). The final column is the most depleted abundances considered and are taken from the sample of SMC HII regions in Kurt & Dufour (1998).

and oxygen. Peimbert (2003) collected a UV-visible spectrum of 30 Doradus in the LMC with the Very Large Telescope; with 269 identified emission lines, they calculate the total abundance of carbon, nitrogen and oxygen. The results differ slightly if recombination lines are used rather than collisionally excited lines; we have chosen to use the results of the collisional lines. These two studies provide us with ISM compositions to model the metal-depleted environments associated with star formation in the Magellanic Clouds. The abundance values are shown in Table 4.3; these abundances will be referred to as MW, LMC, and SMC.

4.3 Results

We computed a grid of fifteen models by multiplying the stellar component of the ISRF with values of [1.0, 1.5, 2.0, 2.5, 3.0] and varying the elemental abundances between initial elemental abundance setups, MW, LMC and SMC. Fig-

ure 4.3 shows the evolution of the dust temperatures and radii for twelve of the fifteen models. The end of collapse is apparent at $\sim 8{\times}10^5$ years, seen in the dust temperature minima; the model is then held at the final collapse density of 2×10^4 cm^{-3} until 5×10^6 years. While the visual extinction remains constant after the final density is reached, halting the increase in attenuation of the radiation field, the dust temperatures continue to fall gradually due to the increasing size of the combined grain plus mantle. At the final visual extinction of 10.6, the dust temperature distribution has flattened for all but the largest grain size, which is somewhat cooler. Ice mantle growth primarily occurs at times immediately before and after the peak density is reached, when accretion onto the grains from the gas phase becomes rapid. The cross-sectional surface area is concentrated in the grains with small radius, causing the accretion rate to be highest for the smallest grains. The radius of this bin increases by up to a factor of three in models with high metal abundances; combined grain and ice radius values are given in Table 4.4.

Figure 4.4 shows, for a selection of models, the fractional ice-mantle composition by species, aggregated over all grain populations and plotted against ice layer depth. This ice depth is normalized to the final total ice abundance. Aggregate abundances for a given species are computed by first determining its fractional surface coverage on each grain size. Next, these fractional coverages are weighted by each grain's relative growth rate with respect to the total grain surface growth rate. These panels plot this weighted aggregate surface composition against the total ice abundance; the upper axis plots time for comparison. The mantle deposition rate for a given species depends directly upon its relative surface population, such that the surface composition is indicative of the newly-formed mantle composition at each point in model time. Therefore, these plots

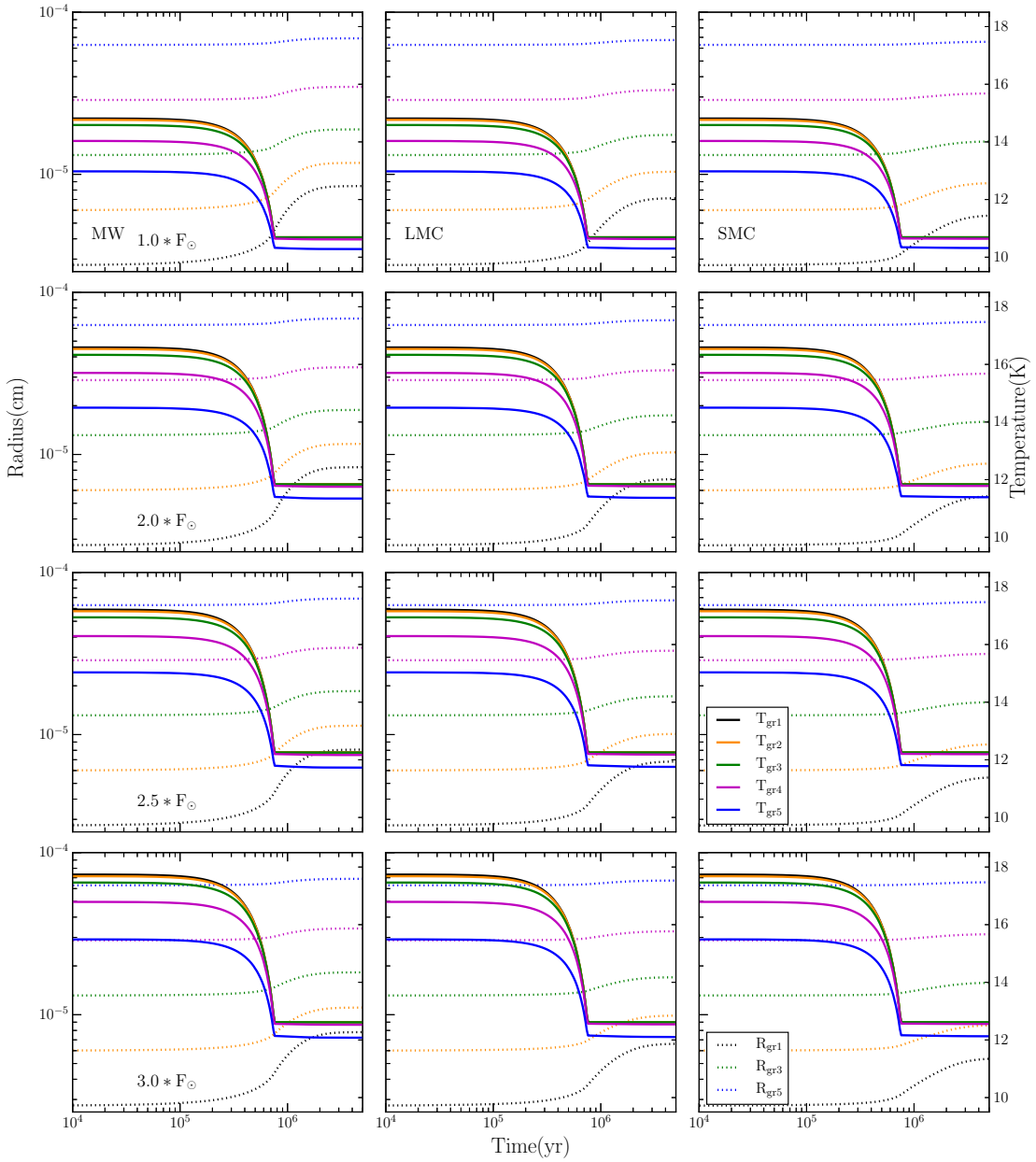

Figure 4.3: Dust temperature (solid lines) and dust radius (dashed lines) versus time for the five grain sizes in the twelve models. Models with MW abundances are shown in the first column, LMC in the second, and SMC in the right column. Dust radius comprises the combined radius of the underlying dust grain plus the ice mantle. The first row has the base ISRF; ISRF increases with decreasing row with values of 2.0, 2.5 and 3.0.

can be read as the mantle composition as a function of aggregate 'layer'.

H_2O is the dominant ice component in nearly all models as expected, follow-

Model	Grain 1	Grain 2	Grain 3	Grain 4	Grain 5
Initial Radii	0.0275	0.0601	0.1313	0.2872	0.6279
1.0_MW	0.0857	0.1185	0.1900	0.3471	0.6893
1.5_MW	0.0853	0.1182	0.1898	0.3464	0.6888
2.0_MW	0.0846	0.1174	0.1891	0.3458	0.6888
2.5_MW	0.0821	0.1149	0.1868	0.3443	0.6894
3.0_MW	0.0795	0.1122	0.1843	0.3420	0.6890
1.0_LMC	0.0712	0.1038	0.1751	0.3312	0.6734
1.5_LMC	0.0709	0.1036	0.1749	0.3309	0.6729
2.0_LMC	0.0704	0.1030	0.1744	0.3305	0.6728
2.5_LMC	0.0682	0.1009	0.1723	0.3290	0.6731
3.0_LMC	0.0661	0.0987	0.1702	0.3270	0.6723
1.0_SMC	0.0556	0.0882	0.1595	0.3154	0.6566
1.5_SMC	0.0555	0.0881	0.1594	0.3153	0.6563
2.0_SMC	0.0552	0.0878	0.1592	0.3151	0.6562
2.5_SMC	0.0544	0.0870	0.1583	0.3145	0.6563
3.0_SMC	0.0535	0.0861	0.1574	0.3136	0.6560
1.0_SMC_gdr500	0.0773	0.1100	0.1813	0.3372	0.6786

Table 4.4: Initial and final grain plus mantle radii, in μm, to accompany Figure 4.3. Note that all models begin with the same grain size distribution, given in the first line.

ing observations. The collapse is complete by $\sim 8 \times 10^5$ ($10^{5.9}$) years; for models with 1.0, 1.5 or 2.0 stellar intensity, this causes dust temperatures to drop below an efficiency threshold for producing CO_2 from CO + OH, identified by Garrod & Pauly (2011). CO mobility on the grain surface is sufficiently slowed at temperatures below $\sim$ 12 K; by this point, the fractional abundance of CO grows above that of CO_2. Models with 2.5 or 3.0 stellar intensity never drop below this temperature threshold, and as a result high CO_2 ice abundances are found throughout those models.

CH_3OH ice is formed via the hydrogenation of surface CO, which is only

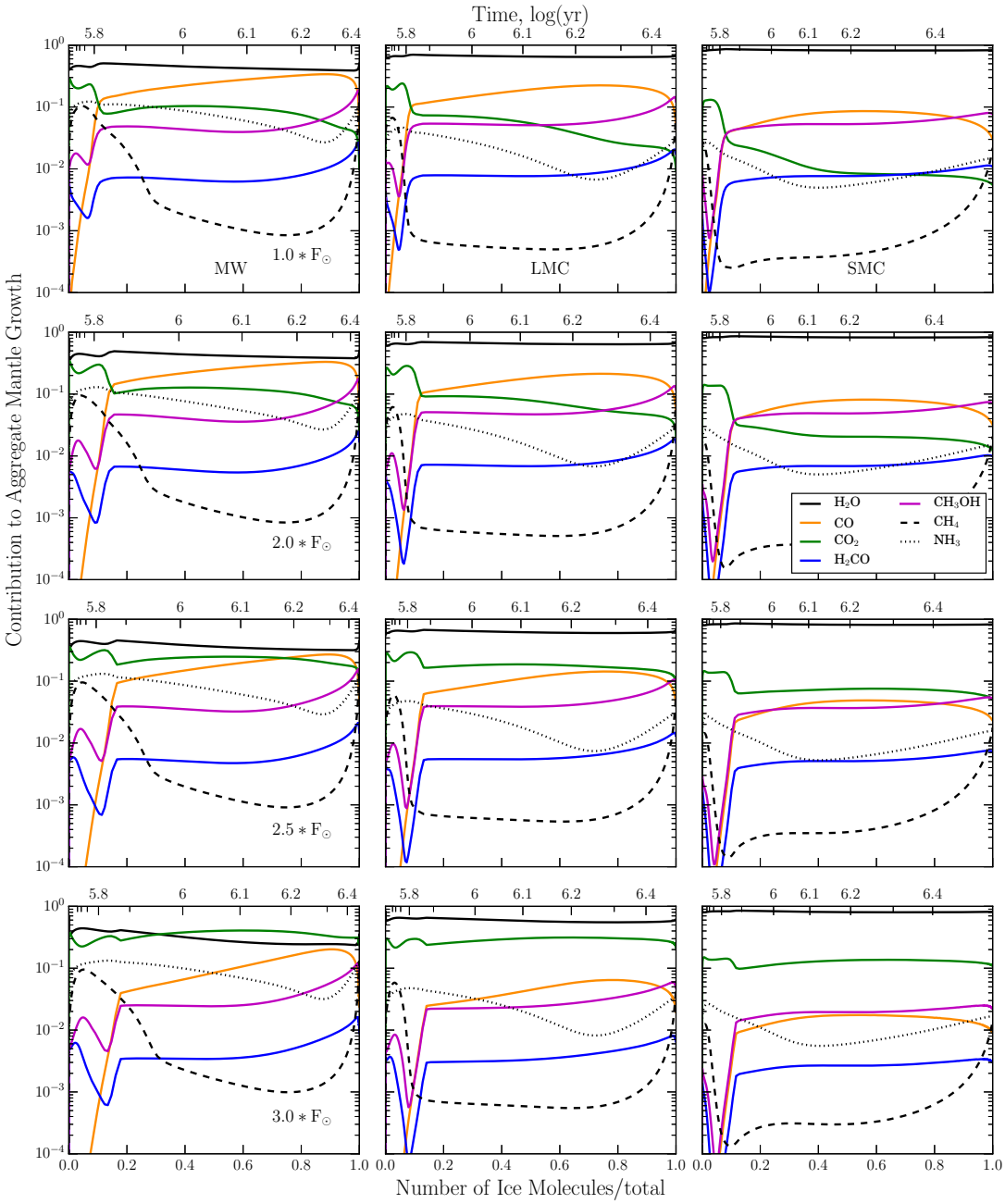

Figure 4.4: Plots of the fractional surface layer abundance plotted against the growth of the aggregate ice mantle. For a given point in the accretion history of the ice mantle, the composition of newly formed mantle material can be read from the surface abundances, aggregated across all grain size bins. Model results with ISRF values of 1.5 are omitted.

present after temperatures drop below the 12 K threshold. For MW models with abundant CO ice, the efficiency of CH_3OH formation appears low, with the

abundance ratio of CH_3OH:CO ranging from 1:2 to 1:5. However, in SMC models with low CO surface abundance, surface CH_3OH can be equal in abundance to CO, and these molecules are similarly abundant throughout those model runs.

The hydrides CH_4 and NH_3 appear to track closely the elemental abundance of their atomic parent, with some dependence on temperature shown for models with galactic elemental abundances.

The following subsections describe the important reactions producing and destroying each primary ice component; we refer to relative abundance trends seen in Figure 4.4 or to abundance values at 10^6 or 5×10^6 years, found in Tables 4.5 and 4.6.

4.3.1 H_2O Ice Behavior

H_2O ice formation occurs primarily through the surface hydrogenation of OH, which is in turn formed via O + H on the surface. Prior to the completion of collapse, if dust temperatures are greater than ~13.5 K, reaction proceeds primarily through OH + H. At these dust temperatures, desorption of H_2 is strongly competitive with the barrier-mediated OH + H_2. After collapse, the dust is cool enough such that H_2 resides on the grain surface for sufficient time to react and becomes the dominant H_2O formation route.

Figure 4.4 shows that H_2O is the most abundant ice mantle component for all models except those with MW elemental abundances at high stellar intensity, 2.5_MW and 3.0_MW. In these models the CO gas abundance is high, and post-

Model	H_2O		CO		CO_2		CH_3OH		CH_4		NH_3	
Time	10^6 yr	5×10^6 yr	10^6	5×10^6	10^6	5×10^6	10^6	5×10^6	10^6	5×10^6	10^6	5×10^6
1.0_MW	6.41(-5)	1.51(-4)	29.0	51.4	26.0	22.1	8.3	11.3	6.9	3.7	22.1	16.9
1.5_MW	6.03(-5)	1.47(-4)	28.5	52.6	30.5	23.7	7.9	11.0	6.7	3.5	21.9	16.1
2.0_MW	5.65(-5)	1.39(-4)	26.2	51.4	37.4	30.5	7.4	10.7	6.9	3.6	22.7	16.7
2.5_MW	4.86(-5)	1.12(-4)	17.8	42.6	57.4	62.2	6.5	10.8	7.8	4.2	26.2	20.7
3.0_MW	4.15(-5)	8.51(-5)	8.1	29.7	82.1	113.0	4.8	10.1	8.9	5.3	30.4	27.2
1.0_LMC	4.28(-5)	1.38(-4)	14.2	24.7	16.2	9.3	6.2	8.8	1.6	0.8	5.3	3.1
1.5_LMC	4.14(-5)	1.37(-4)	13.2	24.7	18.9	10.2	5.7	8.4	1.4	0.8	5.4	3.1
2.0_LMC	4.00(-5)	1.33(-4)	11.6	23.1	22.3	13.7	5.2	8.1	1.4	0.7	5.5	3.2
2.5_LMC	3.67(-5)	1.17(-4)	6.8	15.4	31.8	29.1	4.0	6.8	1.5	0.8	5.9	3.6
3.0_LMC	3.40(-5)	1.01(-4)	2.6	6.8	41.2	48.6	2.3	4.5	1.5	0.8	6.3	4.1
1.0_SMC	2.13(-5)	8.55(-5)	4.3	7.8	5.8	2.3	4.0	6.4	0.3	0.2	1.8	1.2
1.5_SMC	2.10(-5)	8.52(-5)	4.0	7.8	6.9	2.6	3.6	6.2	0.2	0.2	1.8	1.2
2.0_SMC	2.07(-5)	8.41(-5)	3.4	7.3	8.2	3.8	3.2	5.8	0.2	0.2	1.8	1.2
2.5_SMC	2.00(-5)	7.98(-5)	2.0	4.4	11.3	9.3	2.3	4.3	0.2	0.2	1.9	1.2
3.0_SMC	1.94(-5)	7.53(-5)	0.8	1.6	14.3	15.6	1.1	2.2	0.2	0.2	1.9	1.3
1.0_SMC_gdr500	8.35(-6)	7.70(-5)	3.7	7.4	5.4	1.4	4.1	7.1	0.3	0.1	1.8	0.9

Table 4.5: Fractional ice mantle abundances, shown for two times for each species and model; the left sub-column shows abundance (or fractional abundance with respect to water, in percent) at 10^6 years, while the right sub-column shows abundances at 5×10^6 years.

Model	H_2O		CO		CO_2		CH_3OH		CH_4		NH_3	
Time	10^6 yr	5×10^6	10^6	5×10^6	10^6	5×10^6	10^6	5×10^6	10^6	5×10^6	10^6	5×10^6
1.0_MW	6.41(-5)	1.51(-4)	1.86(-5)	7.74(-5)	1.67(-5)	3.33(-5)	5.30(-6)	1.70(-5)	4.44(-6)	5.57(-6)	1.41(-5)	2.54(-5)
1.5_MW	6.03(-5)	1.47(-4)	1.72(-5)	7.73(-5)	1.84(-5)	3.49(-5)	4.76(-6)	1.61(-5)	4.01(-6)	5.12(-6)	1.32(-5)	2.37(-5)
2.0_MW	5.65(-5)	1.39(-4)	1.48(-5)	7.14(-5)	2.11(-5)	4.24(-5)	4.19(-6)	1.49(-5)	3.87(-6)	4.94(-6)	1.28(-5)	2.32(-5)
2.5_MW	4.86(-5)	1.12(-4)	8.63(-6)	4.77(-5)	2.79(-5)	6.95(-5)	3.18(-6)	1.21(-5)	3.77(-6)	4.74(-6)	1.27(-5)	2.32(-5)
3.0_MW	4.15(-5)	8.51(-5)	3.35(-6)	2.53(-5)	3.41(-5)	9.62(-5)	2.00(-6)	8.63(-6)	3.69(-6)	4.54(-6)	1.26(-5)	2.31(-5)
1.0_LMC	4.28(-5)	1.38(-4)	6.08(-6)	3.42(-5)	6.93(-6)	1.29(-5)	2.64(-6)	1.22(-5)	6.71(-7)	1.12(-6)	2.27(-6)	4.34(-6)
1.5_LMC	4.14(-5)	1.37(-4)	5.48(-6)	3.38(-5)	7.82(-6)	1.41(-5)	2.36(-6)	1.15(-5)	5.98(-7)	1.03(-6)	2.23(-6)	4.28(-6)
2.0_LMC	4.00(-5)	1.33(-4)	4.64(-6)	3.07(-5)	8.93(-6)	1.82(-5)	2.08(-6)	1.07(-5)	5.71(-7)	9.87(-7)	2.20(-6)	4.25(-6)
2.5_LMC	3.67(-5)	1.17(-4)	2.51(-6)	1.81(-5)	1.17(-5)	3.40(-5)	1.46(-6)	8.00(-6)	5.43(-7)	8.91(-7)	2.18(-6)	4.22(-6)
3.0_LMC	3.40(-5)	1.01(-4)	8.96(-7)	6.85(-6)	1.40(-5)	4.93(-5)	7.91(-7)	4.53(-6)	5.12(-7)	7.83(-7)	2.15(-6)	4.19(-6)
1.0_SMC	2.13(-5)	8.55(-5)	9.13(-7)	6.68(-6)	1.24(-6)	1.93(-6)	8.54(-7)	5.47(-6)	5.95(-8)	1.99(-7)	3.82(-7)	1.00(-6)
1.5_SMC	2.10(-5)	8.52(-5)	8.29(-7)	6.68(-6)	1.46(-6)	2.21(-6)	7.60(-7)	5.25(-6)	4.93(-8)	1.86(-7)	3.79(-7)	9.97(-7)
2.0_SMC	2.07(-5)	8.41(-5)	7.11(-7)	6.13(-6)	1.70(-6)	3.22(-6)	6.63(-7)	4.85(-6)	4.36(-8)	1.75(-7)	3.77(-7)	9.95(-7)
2.5_SMC	2.00(-5)	7.98(-5)	4.02(-7)	3.55(-6)	2.26(-6)	7.42(-6)	4.53(-7)	3.44(-6)	3.84(-8)	1.49(-7)	3.75(-7)	9.92(-7)
3.0_SMC	1.94(-5)	7.53(-5)	1.52(-7)	1.24(-6)	2.79(-6)	1.18(-5)	2.23(-7)	1.66(-6)	3.37(-8)	1.18(-7)	3.72(-7)	9.88(-7)
gdr500[a]	8.35(-6)	7.70(-5)	3.09(-7)	5.70(-6)	4.48(-7)	1.07(-6)	3.43(-7)	5.50(-6)	2.16(-8)	7.19(-8)	1.52(-7)	6.75(-7)

Table 4.6: Absolute ice mantle abundances, shown for two times for each species and model; the left sub-column shows abundance at 10^6 years, while the right sub-column shows abundances at 5×10^6 years. [a]:Model name abbreviated from 1.0_SMC_gdr500.

collapse temperatures are warm enough for CO mobility on the grain surface. These effects combine for CO + OH to compete effectively with H + OH and H_2 + OH, reducing H_2O ice abundance while enhancing CO_2. In models with reduced elemental abundances, CO never attains the surface coverage required for CO_2 production to reach similar levels. Additionally, the decreased C/O ratio in 'LMC' and 'SMC' chemistries further enhances H_2O dominance over carbon-bearing ice species.

The absolute abundance of H_2O ice (Table 4.5) does not strictly follow the abundance of oxygen across the different models; because the carbon abundance serves to lock oxygen into CO-structured molecules, the fraction of oxygen found in H_2O is determined in large part by the C/O ratio. As dust temperature increases due to increased stellar intensity, H_2O ice abundance drops. This is due to increased competition between OH + CO and OH + H/H_2; increasing temperatures serves to increase the fraction of OH going towards CO_2 formation via increased CO mobility, while the production of H_2O decreases in turn.

4.3.2 CO Ice Behavior

CO is efficiently formed in the gas phase and accretes onto the grain surface. At early times in the model nearly all surface CO reacts with OH to form CO_2 due to mobile CO on the warm ($\gtrsim 12K$) dust. If the dust temperature remains high after collapse, CO_2 efficiently forms at late times as well. At post-collapse densities, the hydrogenation of CO into the short-lived HCO also becomes an important process, with possible outcomes of reverting to CO or forming stable H_2CO.

H_2CO can then be further hydrogenated to form methanol, CH_3OH. These reactions serve to destroy CO ice; however, if accretion rates are comparable to the rate of these destruction reactions, the transport of CO to the mantle phase can proceed before the destruction of all surface CO, leading to non-negligible CO mantle abundances and less efficient conversion to methanol.

Figure 4.4 shows low CO abundances pre-collapse for all models. Post-collapse, the behavior is determined by the dust temperature and the accretion rate. Accretion rate is driven by the amount of carbon, oxygen and other heavy elements in the model; it is lowest in SMC models and highest in MW models. Higher accretion rates will drive more surface CO into the inert mantle simply by building up the ice layers more quickly, leading to higher CO ice abundances in the mantles. The post-collapse dust temperature determines the efficiency of CO_2 formation; for models with less than 2.5 times the base stellar intensity, an inversion in the CO:CO_2 ratio is seen at the end of collapse, while a stronger interstellar radiation field allows strong CO_2 formation even to A_V of 10.6. This depletes CO levels for the entirety of the model.

The surface abundances of the five grain populations are shown separately in Figures 4.5 and 4.6 for two models, 1.0_LMC and 3.0_LMC. In Figure 4.5, the abundance of CO is seen to increase dramatically as the model collapses and grain temperatures drop below the 12 K threshold. The exact time of the abundance turnover is different for the individual grain populations, as each has a different temperature. Figure 4.6 shows a model dominated by CO_2 for all but the largest grains due to elevated dust temperatures induced by the elevated ISRF value of 3.0. The relative drop in temperature is also more extreme, and the finite number of time steps is apparent in these plots due to a rapid transition in

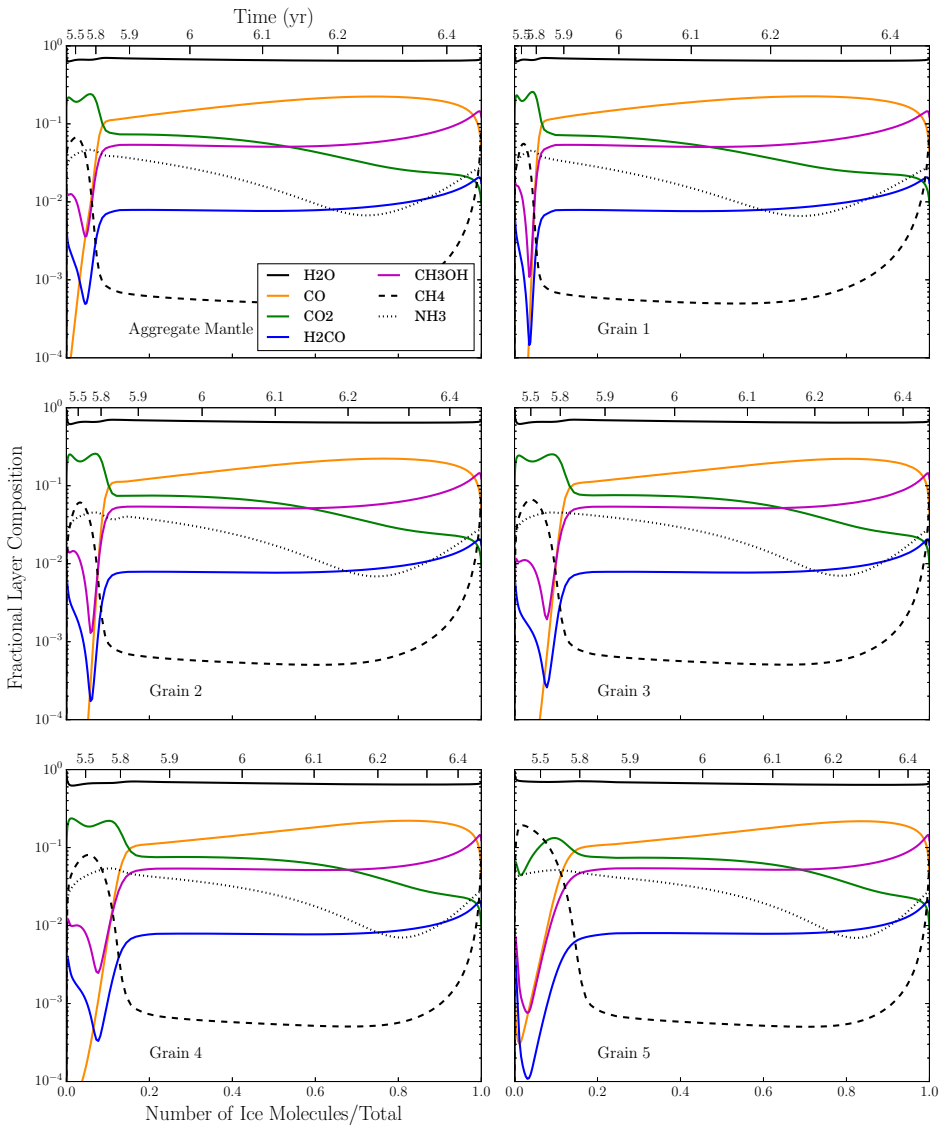

Figure 4.5: These panels plot the fractional layer composition as a function of total mantle plus surface abundance (or time) for the model 1.0_LMC. The aggregate layer composition is shown in the top left panel, as in Figure 4.4. The following five panels depict the fractional layer abundances for the five grain size populations in the model.

chemical behavior.

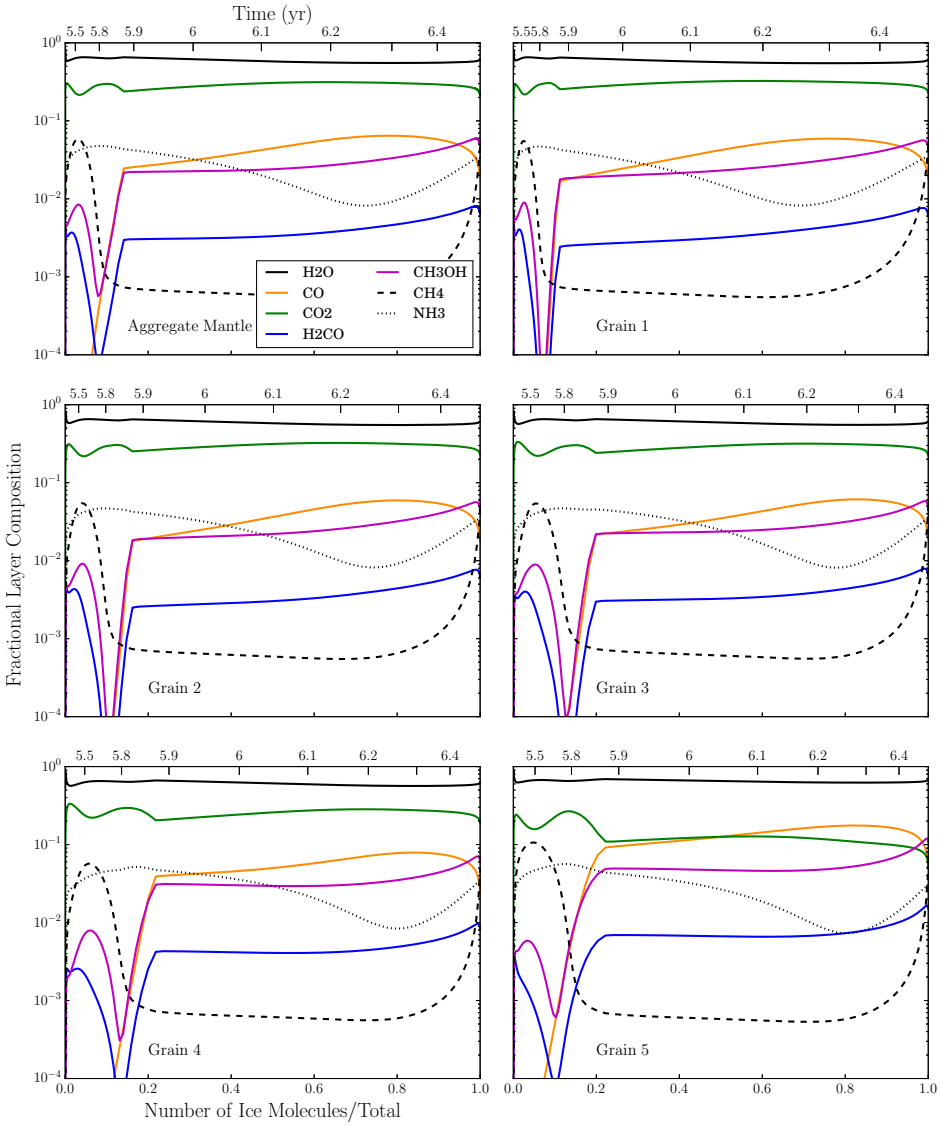

Figure 4.6: Fractional layer compositions, as in Figure 4.5, but for the model 3.0_LMC.

4.3.3 CH_3OH Ice Behavior

Hydrogenation of CO to CH_3OH has two steps with activation energy barriers that produce short-lived radicals, HCO and CH_2OH/CH_3O. Hydrogenation of

HCO will form products of either H_2CO or H_2 + CO with equal probability, an assumption of our model. Once formed, H_2CO is fairly robust to reverting to a less-hydrogenated form, reacting with a hydrogen atom to form CH_3O or CH_2OH more readily than HCO + H_2. Hydrogen addition to H_2CO and abstraction from CH_3OH are fast, as manifested in the constant ratio of surface abundances between the two species across all models.

The total abundance of CH_3OH ice in the models shown in Table 4.6 has little spread, with variation of only a factor of two to four across models with an order of magnitude less elemental carbon abundance (MW to SMC). Notably, the amount of CH_3OH relative to the amount of CO on the grain surface increases as the elemenatal carbon abundance decreases across models. The change is primarily driven by a strong decrease in CO ice abundance as elemental abundances decrease, from MW to LMC to SMC values. For a set of models with equal elemental abundances, the abundance of CH_3OH drops by a factor of two to four as the ISRF increases from 1.0 to 3.0, showing a decrease in formation efficiency at higher dust temperatures.

4.3.4 CH_4 and NH_3 Ice Behavior

These ices form primarily through successive hydrogenation on grain surfaces. NH_3 ice has a linear pathway with little branching, though N_2 can be a significant nitrogen carrier for models with high nitrogen abundance. CH_4 ice shows similar behavior; the primary formation of CH_4 begins with atomic carbon. The sharp decline in CH_4 ice abundance shown in Figure 4.4 at early time is indicative of carbon forming CO in the gas phase and the atomic abundance decreas-

ing rapidly. Because nitrogen has no equivalent reservoir, its ice behavior is more consistent throughout mantle formation.

The total abundance of NH_3 ice shown in Table 4.6 reflects a consistent fraction of total nitrogen found in NH_3 ice across models with varying elemental nitrogen abundance. However, CH_4 ice does not follow this trend; CH_4 ice abundance per carbon atom is elevated in models with increased elemental carbon abundance. This likely reflects the increasing carbon to oxygen ratio found in our choice of elemental abundances; models with increased carbon abundance also have an increased carbon to oxygen ratio, allowing for more carbon to be found outside of CO-based species.

Figure 4.5 shows the ice compositions of individual grain sizes in the distribution, specifically for the 1.0_LMC model. CH_4 behavior on the largest grain size differs from its counterparts at early times ($\sim 3 \times 10^5$ years). CH_4 surface abundance is greater than CO_2 for the largest grain; this is caused primarily by the difference in temperature between the grain sizes, with lower temperatures enhancing hydrogenation rates of atomic carbon. The destruction of atomic carbon on large grains is almost entirely through C + H $\rightarrow$ CH, while on small grains roughly 20% of carbon reacts via C + OH $\rightarrow$ CO + H. Additionally, the warmer temperatures on small grains permits diffusion of the CH_3 radical, opening new pathways for destruction of CH_3 via e.g. CH_3 + CH_3 $\rightarrow$ C_2H_6, a molecule not yet detected in interstellar regions but strongly detected in the coma of Comet Hyakutake (Mumma et al., 1996). Ethane surface and mantle abundances are highest on the small grains, with a C_2H_6:CH_4 grain abundance ratio in the model 1.0_LMC of 1.0 at 3×10^5 years, dropping to 0.1 at 10^6 years.

4.4 Discussion

Figure 4.7 shows the model results overlaid on the observations. For each model we plot two points per panel; for the top panel, the smaller leftward point shows the ice composition at $8{\times}10^5$ years, while the large rightward point shows the composition at 10^6 years. The lower panel shows the same models at times of 10^6 years and $5{\times}10^6$ years. The choice of time spent at post-collapse density is arbitrary, and because physical conditions do not change significantly during this time, the composition follows a roughly straight line between these points. The MW and SMC abundance models appear to match observations more closely at earlier times, while the LMC observations have variation such that model matches are found at both early and late times.

Models with MW abundances show compositions enriched in CO_2 and CO/CH_3OH, with the relative enrichment between the two set by the stellar flux parameter. As no observations lie near the high-flux galactic abundance models, these models do not appear to represent any observed MYSO and can be ignored.

LMC MYSOs demonstrate large variation in composition, from extreme CO/CH_3OH depletion (as in SMC sources) to highly enriched in CO_2. Models with LMC-like elemental abundances fall across the ensemble of LMC MYSOs, though there is considerable overlap between LMC and galactic sources. The models separate cleanly on this plot, implying additional effects not addressed in the model setup. Variation in local metallicity may cause blending, as metal-poor MW YSOs may appear chemically similar to LMC MYSOs. Parameters beyond our model, such as variation in collapse speed or ice processing may

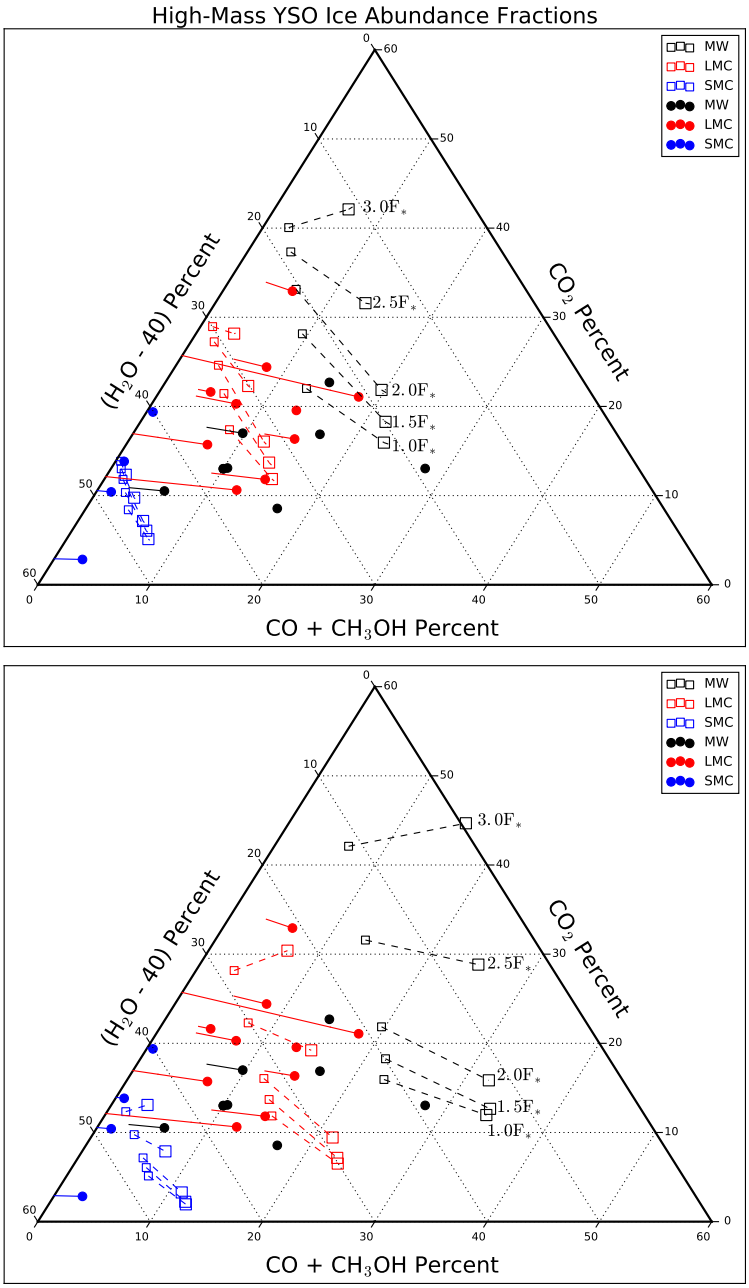

Figure 4.7: These panels overlay the model results on the observations from Figure 4.1. With matching colors for model elemental abundances to source environment (MW, LMC, SMC), models with increasing stellar flux parameter move upwards on the plot, with galactic chemical abundance models labeled. For each model, two points are plotted; for the top panel, the smaller leftward square shows the ice composition at the time of collapse completion (~8×10^5 years), while the larger rightward square shows the composition at 10^6 years. For the lower panel, the leftward square shows the composition at 10^6 years, while the rightward square shows the values for 5×10^6 years. (Ternary figure style from Harper et al., 2015)

also play a role. Models are able to fit LMC observations at the full range of stellar flux parameter tested.

Models with the most depleted elemental abundances fall near the observed SMC MYSOs, matching the low (undetected) CO abundance and presence of CO_2. The models lying closest to observed YSO abundances have high stellar flux values, though the models cannot fully reproduce the spread in CO_2 abundances and typically overproduce CO/CH_3OH. Of note, the composition of SMC models in Figure 4.4 shows a roughly equal abundance of surface CO and CH_3OH, while observational upper limits exist only for CO. Tightening the abundance constraints on these two species would provide strong evidence for the validity of our CO surface chemistry.

The increased CH_3OH abundance relative to CO in SMC models is an unexpected result. CH_3OH formation requires CO surface residence times to be longer than the mantle deposition timescale to allow sufficient time for hydrogenation. In this way, the balance between CO and CH_3OH is determined primarily by the accretion rate of elements heavier than hydrogen. With long CO surface residence times, CO_2 production will also be increased if dust temperatures are above the necessary threshold for CO surface mobility.

4.4.1 Thermal Ice Processing

The models produce a reasonable fit to observations, though a general trend exists in overproduction of (CO + CH_3OH). This may not be a simple model issue but instead a comparison of model results to observations in different physical regimes. These MYSOs are highly luminous objects, and thermal processing

of the envelope is likely to have occurred in many sources. In this case, the most volatile ices may be under-abundant due to desorption when compared to the final model output, which ends prior to a grain heating and ice desorption phase.

Collings et al. (2003a,b) find a significant fraction of CO ice desorbs at grain temperatures of ~ 25 K, with some CO still bound to open OH bond sites within the H_2O-dominated ice matrix. In this picture, CO ice is able to linger in the H_2O ice until ~ 140 K, when H_2O ice crystallization removes the bond site for CO and it readily desorbs. If temperatures reach $\gtrsim$ 70 K, CO_2 will begin desorption from an H_2O surface (Fayolle et al., 2011; Noble et al., 2012). Entrapment of CO_2 in the H_2O ice will prevent complete removal of CO_2, though relative loss is dependent on ice thickness, mixing ratio, and other parameters. Complete loss is not expected until H_2O crystallization. These experimental results provide evidence for the observations having gone through some amount of mantle desorption; models with a following warm-up phase may better account for this effect.

We use a single-point model to trace the collapse; the outer regions of a core may be chemically younger than the central source, and this difference in total ice formation between regions may be significant depending on the age of the outer envelope. Ice formed in this young environment would be CO_2-rich and CO-poor. If inner regions are strongly heated by star formation, envelope ice could also provide a reservoir for some CO ice without the need for entrapment in H_2O.

4.4.2 Cosmic Ray Ionization Rate

The cosmic ray ionization rate, ζ, was held fixed throughout our model grid at a value of 1.3 $\times 10^{-17}$ s^{-1}. Other chemical model work in the Magellanic Clouds have used either the galactic local value or an enhanced value (Chin et al., 1998; Acharyya & Herbst, 2015, 2016). Data on ζ_{LMC} and ζ_{SMC} is scarce; Abdo et al. (2010a) analyzed a Fermi-LAT >100 MeV gamma ray map of the LMC and found the globally-averaged cosmic ray ionization rate to be 20-30% of the local MW value. Regional variability can be significant, with cosmic ray sources in the LMC causing nearby regions to have ionization rates higher than the globally averaged value. SMC studies lack the sensitivity and resolution required for anything other than a global measurement; this value is depleted by at least a factor of six to seven with respect to the local galactic value (Abdo et al., 2010b).

4.4.3 Gas to Dust Ratio

Another model quantity held fixed was the gas to dust ratio, at a value of 175. This is known to vary with environment, but we chose to keep it fixed to disentangle its effects from the effects of changing elemental abundances and dust temperatures. We ran an additional model with a base ISRF value and SMC abundances at a gas to dust ratio of 500 to test the robustness of the grid results. The aggregate mantle of the reduced dust model is shown in Figure 4.8 below to the equivalent grid model with a ratio of 175. The composition does not appreciably change while the aggregate accretion rate is seen to decrease, evidenced by the longer times required to reach an equivalent relative ice abundance. Absolute ice abundances are given in Table 4.6; the decreased accretion

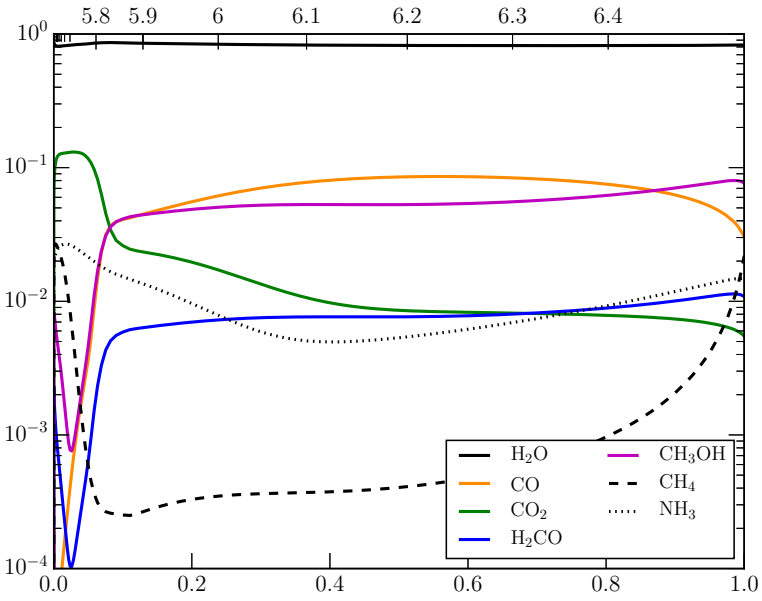

(a) Gas to Dust Ratio: 175

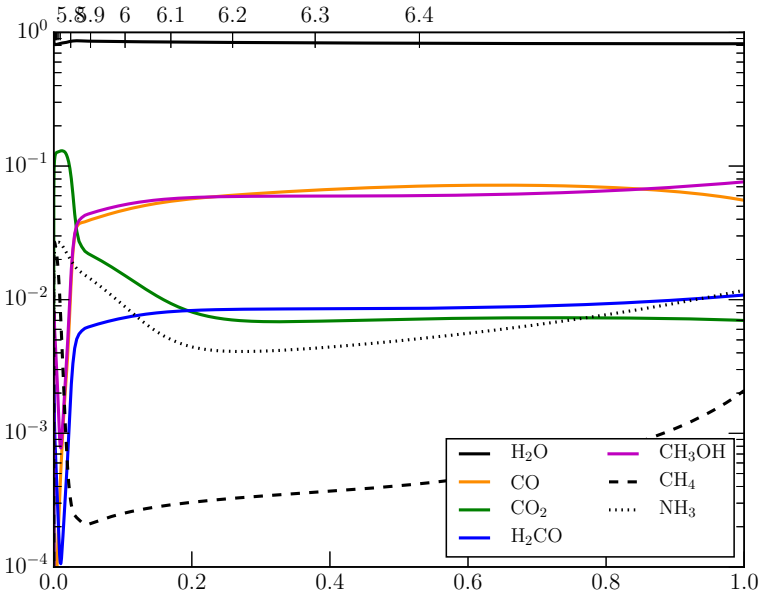

(b) Gas to Dust Ratio: 500

Figure 4.8: These panels compare models with 1.0 F_* and SMC abundances but differing gas to dust ratios. Panel (a) shows the model with a ratio of 175 while panel (b) shows the model with a ratio of 500.

rate lowers CO_2 abundance, while other species are comparable due to the long post-collapse phase from 10^6 to 5×10^6 years. Notably, the model with an increased gas to dust ratio still exhibits enhanced CH_3OH abundance. The increased formation efficiency of CH_3OH appears to be directly connected to the heavy atom accretion rate onto grain surfaces, the key driver of inert ice mantle growth. If the ice mantle does not grow quickly enough to sequester CO, long surface times coupled with high hydrogen accretion rates produce a high CH_3OH abundance.

4.5 Summary

Our results suggest that gas-grain models of cold cloud collapse can produce ice mantle abundances that match reasonably well to observations in a variety of environments. We conclude that:

- The values of ISRF intensity and elemental abundances chosen provide an adequate distribution of ice abundances that cover the observed ice abundances in YSOs. Models with strongly enhanced ISRF intensity at MW elemental abundances are excluded, while SMC models with enhanced ISRF are preferred.
- LMC models lie near observed YSOs for every value of the ISRF intensity modeled, characterizing the large spread in LMC YSO ice abundances. This may be indicative of large local fluctuations in the LMC ISRF.
- The ISRF intensity strongly affects the relative abundance of CO_2 to CO/CH_3OH, with higher ISRF values leading to CO_2 enhancement. This

is caused by a temperature threshold for CO mobility on grain surfaces, leading to efficient production of CO_2 at dust temperatures $\gtrsim 12$ K.

- Increasing model elemental abundances (and corresponding C/O ratio) decreases the H_2O abundance against the other ices; this is evidenced by model values moving parallel to the H_2O ternary axis with changes in elemental abundance.
- Our models indicate that the lack of CO in SMC sources is most likely caused by a combination of low elemental abundances and high ISRF intensity.
- CH_3OH abundance is found to be enhanced in low-metallicity environments. This will be important for complex organic molecule production in LMC and SMC hot core models.

We leave some issues to be addressed in future work. Thermal processing of the ice is important for matching observed ice abundances, and it is not included in these models. We find significant growth in the [dust+mantle] radius, which affects both the dust temperature and surface chemistry; however, we assume a Q_{abs} of carbonaceous dust for temperature calculations, though the Q_{abs} of ice will differ. We also use a grain size distribution found for silicate grains; this could be resolved by using values for silicate or carbonaceous grains throughout, or by attempting to model both populations.

Future models could investigate the dependence on cosmic ray ionization rate, a parameter with large variation across the LMC. The rate of collapse may also be important, as it sets the heavy atom accretion rate. Follow-up models will address behavior in collapse to higher densities ($\sim 10^7$ cm^{-3}), including a

warm-up phase for comparison to a newly detected hot core in the LMC (Shimonishi et al., 2016b).

CHAPTER 5

CONCLUSIONS AND FUTURE WORK

In this work I have presented an update to the gas-grain chemical code MAGICKAL which introduces multiple grain sizes and the ability to track the surface and mantle chemistry on separate grain populations. Models including two to eleven grain sizes were analyzed with either quiescent or collapsing dark cloud conditions.

We found that the inclusion of multiple grain sizes does not strongly affect the chemistry if the temperature of the multiple grain size populations is assumed to be uniform. However, multiple grain sizes can be important if grain temperatures are varied; particularly, a large effect is seen when calculated dust temperatures fall near critical values related to the desorption and diffusion barriers of common interstellar species, e.g. increased CO surface mobility at $T_d \gtrsim$ 12 K. Ice mantles on the smallest grain sizes have relatively few monolayers, making mantle species more readily available for chemistry during the active ice phase of future warm-up models.

We applied this updated MAGICKAL model to an investigation of ice mantle formation in the cold envelopes surrounding massive young stellar objects. We compare our models to a sample of luminous MYSOs in the Magellanic Clouds (MCs) and the galaxy. The MYSOs studied display prominent infrared absorption caused by significant line-of-sight column densities of H_2O, CO, CO_2, and CH_3OH ice, with the relative abundance of each component varying dramatically across environments. We modeled the the envelope with a single-point model undergoing free-fall collapse from n_H=3×10^3 cm^{-3} to 2×10^4 cm^{-3}. We created a grid of models with varied initial conditions; we scale the external

radiation field to replicate the observed elevated dust temperatures in the MCs as compared to galactic environments, and we reduce the elemental abundances to match those measured in LMC and SMC HII regions.

Across the grid of models, we are able to find reasonable fits to the observations. SMC models have strongly reduced CO abundances, fitting well the upper limits towards SMC MYSOs. LMC sources show the greatest variation in H_2O:CO_2:[CO+CH_3OH] relative abundances, and the models using LMC elemental abudances are able to match the extent of compositional variation. Galactic MYSOs somewhat overlap LMC sources; models with galactic abundances and elevated dust temperatures do not match any source we considered.

The discrepancies that remain between models and observations point to the importance of thermal processing of the ices. Due to the proximity of the envelope to its luminous host, an additional radiation field is present which our model does not account for. We found a unexpectedly high abundance of CH_3OH ice relative to total carbon abundance in models with LMC and SMC elemental abundances. CH_3OH ice is the precursor to many complex species formed in during the warm-up associated with the hot core phase of massive star formation; modeling the chemistry in MC hot cores has not yet been explored, and will prove an exciting environment for future observational facilities such as ALMA and the James Webb Space Telescope (JWST) to explore.

We now outline our future study of chemistry in massive star-forming regions of the Magellanic Clouds, modeling the recently discovered hot cores in the Large Magellanic Cloud (Shimonishi et al., 2016b, R. Indebetouw 2017, private communication). The project is ongoing, and results from only the first phase of modeling is complete.

5.1 Models of Hot Core Chemistry in the Magellanic Clouds

Hot cores are dense ($n_H \sim 10^7$ cm^{-3}) and warm ($T_d \sim 100 - 250$ K) regions surrounding forming massive stars, suggested to be a short-lived stage between deeply embedded protostars and zero-age main sequence stars inside a compact HII region. During the cold collapse from molecular cloud to prestellar core, density increases and the extinction rises, driving gas and dust temperatures to values $\lesssim 8$ K. Gas-phase species accrete onto grain surfaces, forming substantial ice mantles composed primarily of H_2O, CO, CO_2, CH_3OH, NH_3, and CH_4.

As the protostar forms and heats the core, dust temperatures rise; this mobilizes grain-surface and ice-mantle species and enables the formation of complex molecules. As the dust temperatures continue to rise, surface species attain sufficient energy to desorb and return to the gas phase. H_2O, the dominant ice mantle component, will sublimate efficiently at $T_d \gtrsim 150K$; once refractory species are liberated, further complex molecule formation occurs in the warm, dense gas (Garrod & Herbst, 2006; Garrod, Widicus Weaver & Herbst, 2008).

Molecules in the warm gas phase radiate in a multitude of rotational lines, providing observational markers of chemical formation and history as well as the ability to constrain environmental parameters such as gas temperature and density. To understand how the complex chemical processes of hot cores depend on metallicity and other environmental parameters, we can target sources in the nearby Large Magellanic Cloud. The low metallicity ($Z \sim 0.4\ Z_\odot$) and low dust-to-gas mass ratio (approximately half the value of the solar neighborhood) provide a unique laboratory to study massive star formation.

Shimonishi et al. (2016b) (hereafter S16) targeted ST11, a source spectroscopically confirmed to be a MYSO in previous work (Seale et al., 2009; Shimonishi et al., 2010), with the Atacama Large Millimeter/Sub-Millimeter Array (ALMA). Observations were taken in Band 7, with spectral bands targeting molecular emission lines in the the frequency range 336-357 GHz; observations were in compact configurations, leading to a synthesized beam size of $0.''5 \times 0.''5$, corresponding to 0.12 pc at the assumed LMC distance of 49.97 pc (Pietrzyński et al., 2013).

S16 detect a variety of molecules towards ST11: CO, $C^{17}O$, HCO^+, $H^{13}CO^+$, NO, H_2CO, SiO, H_2CS, ^{33}SO, SO_2, $^{33}SO_2$, and $^{34}SO_2$. The source size in 840 μm continuum is estimated with a Gaussian FWHM at $0.''6$, very near the beam size. Molecular lines of NO, SiO, ^{33}SO, SO_2, and $^{34}SO_2$ have an extent equivalent to the beam size, while HCO^+, $H^{13}CO^+$, H_2CO, CO, and $C^{17}O$ are extended, with FWHM of $0.''8$-$1.''4$.

Surprisingly, S16 find only upper limits for more complex molecules, e.g. CH_3OH, CH_3OCH_3, C_2H_5OH, and $HCOOCH_3$. The upper limit for CH_3OH towards ST11 lies more than two orders of magnitude below the column density seen towards galactic hot cores in Orion or W3 (Schilke et al., 1997; Helmich & van Dishoeck, 1997). The lack of saturated complex molecules seen towards the LMC hot core may point to a striking chemical difference in this phase of high-mass star formation.

5.1.1 Hot Core Model Methods

To investigate this contrast in chemical inventory, we apply the MAGICKAL three-phase chemical code to a study of the warm-up phase associated with high-mass star formation. We track the gas-phase, grain-surface, and active ice-mantle chemistry across multiple grain sizes through a coupled system of modified rate equations.

Our physical model follows the approach of Garrod (2013); we start with a collapse phase, beginning at a density $n_{\rm H} = 3 \times 10^3$ cm^{-3} and a visual extinction $A_V = 3$. The collapse follows the free-fall expression given in section 4.2.2. Dust temperatures are calculated following Pauly & Garrod (2016) and drop as density increases; the gas temperature is held fixed at 10 K. We halt the collapse phase when it reaches a density of $n_{\rm H} = 1 \times 10^7$ cm^{-3}, at which point $A_V \approx 670$. At this point $T_d \approx 7.5$ K, and most heavy species have accreted onto the dust, forming thick ice mantles.

We then begin a static warm-up phase, heating the dust from 8-200 K at constant density. The high density couples the thermal properties of the gas and dust, such that $T_{gas} = T_d$ once $T_d > 10$ K. We set our initial batch of warm-up models to complete this phase in a warm-up timescale of 2×10^5 years; future models may adopt the fast timescale of 5×10^4 years used in Garrod (2013), as we expect the Magellanic Cloud MYSOs of interest to probe the upper limits of stellar mass and thus the lower limits of formation timescale.

We have used the initial conditions presented in sections 4.2.3 & 4.2.4 to create a grid of models following the physical methods outlined above. We vary the external radiation field strength and elemental abundances to simulate hot

core evolution in Magellanic Cloud environments, with MW models for comparison. At the time of writing, only the collapse phase of the model grid has been completed.

5.1.2 Collapse Results

Source	CO	CO_2	CH_4	H_2CO	CH_3OH	NH_3
W33A[a]	8	13	1.5	6	18	15
NGC 7538 IRS 9[a]	16	22	2	4	5	13
Median Low-Mass Protostar[b]	29	29	5	$\lesssim$2	3	5
Median High-Mass Protostar[b]	13	13	2	$\lesssim$2	4	5
Model	CO	CO_2	CH_4	H_2CO	CH_3OH	NH_3
1.0F_* MW	57	17	3.1	1.2	3.9	17
3.0F_* MW	58	23	2.7	1.0	4.2	18
1.0F_* LMC	30	8.4	0.5	0.8	3.1	3.8
3.0F_* LMC	29	11	0.3	0.8	3.1	3.9
1.0F_* SMC	13	2.3	0.1	0.6	2.4	1.0
3.0F_* SMC	13	3.3	0.1	0.6	2.3	1.0

Table 5.1: Ice compositions of a variety of galactic protostars, given as a percentage with respect to H_2O ice abundance. Model compositions shown are post-collapse, prior to any warm-up. [a]:Gibb et al. (2000), and references within; [b]: Öberg et al. (2011)

We compare the composition of our post-collapse ice mantles to a selection of observed protostars in Table 5.1. The 1.0F_*MW model well reproduces the results of Garrod (2013), though it produces $\approx$ 40% less CH_3OH ice. The final ice composition is not strongly sensitive to the initial radiation conditions; CO_2 is the only sensitive component, with 30-50% more CO_2 in models with the highest radiation field scale factor.

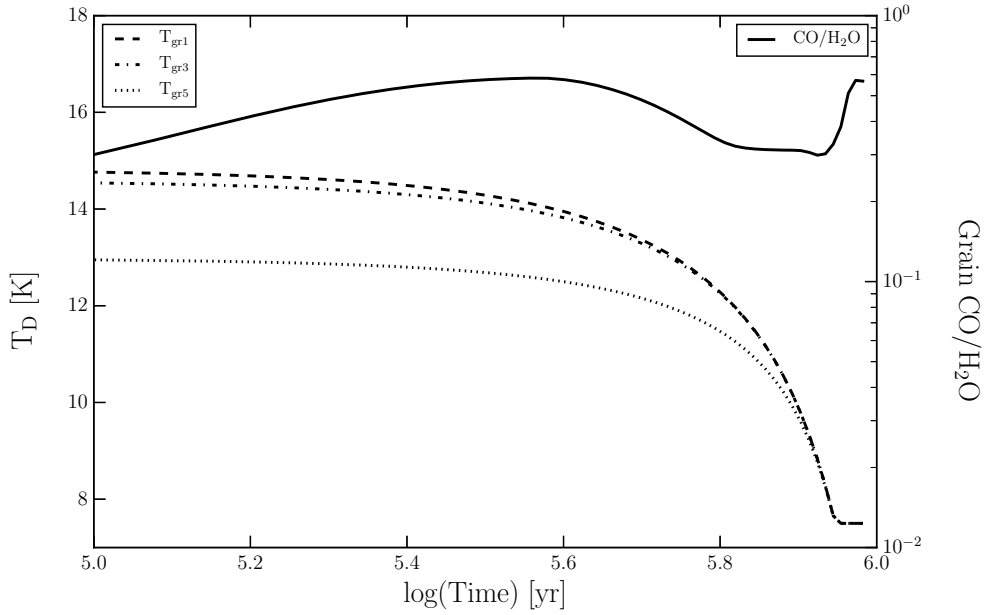

Figure 5.1: Tracks of dust temperature and [surface+mantle] CO fractional abundance with respect to H_2O for the model 1.0F_*MW.

Figure 5.1 shows the evolution of dust temperature and CO fraction for the model 1.0F_*MW. The CO abundance in MW models is high when compared to observations, but the period of collapse during which the abundance is discrepant is relatively short. Additionally, hot cores for which we observations must have proceeded past the collapse stage, by which point thermal ice processing will have desorbed some fraction of the solid CO.

Figure 5.2 shows the evolution of the the primary ice species, presented as a fractional [surface+mantle] abundance with respect to H_2O abundance. Also shown is the normalized total mantle abundance, read from the right-hand axis. For model 3.0F_*MW, grain CO_2 abudance exceeds that of H_2O at early times; however, this time period accounts for <10% of the total mantle growth. Indeed, half of the total mantle is accreted in the last 10^5 years of the collapse. During this time, dust temperatures are <12 K and CO ice is more abundant than CO_2.

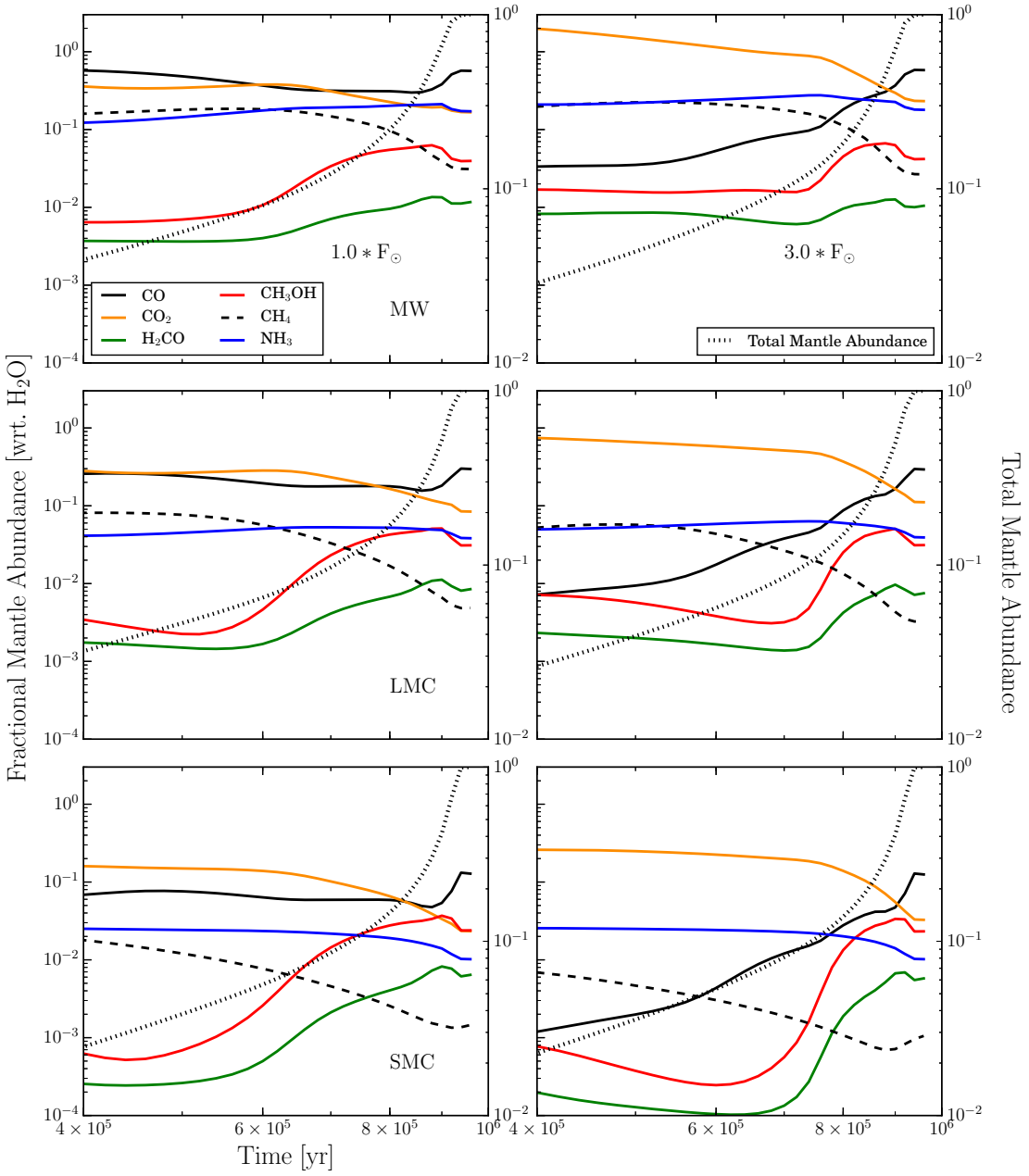

Figure 5.2: Plot of [surface+mantle] abundances for primary ice species, presented with respect to [surface+mantle] H_2O abundance, read from the left-hand axis. Also shown is the normalized sum of all mantle species, read from the right-hand axis.

During the period of strong CO accretion and low dust temperature, CH_3OH readily forms from successive hydrogenation of CO. CH_3OH abundances are remarkably similar across models, as in the models shown in Chapter 4. Despite an order of magnitude of variation in elemental carbon abundance between MW and SMC models, absolute mantle CH_3OH abundance in $1.0F_*$SMC is 30% of that in $1.0F_*$MW.

5.1.3 Future Work

Warm-up models will be computed, utilizing the same physical model but varying the initial chemical composition of the gas and ice mantles, according to the post-collapse abundances calculated above. We plan to compare the results of these models to the observations of S16, as well as provide a first attempt at modeling these low-metallicity complex environments. We expect great strides in observational constraints, both with ALMA in the sub-millimeter and with JWST in the infrared. Differences found between MC and MW models may assist observers in targeting chemical species of interest. In addition, it is of great interest to understand the possible depletion of CH_3OH in MC hot cores, as suggested by the results of S16. We expect this work to be published in 2018.

APPENDIX A

APPENDIX: SPECTRAL EXTRACTION METHODS FOR YOUNG STELLAR OBJECTS IN THE LARGE MAGELLANIC CLOUD

This appendix details a project undertaken in 2015 to examine a catalog of mid-infrared spectra of massive young stellar objects (MYSOs) in the Large Magellanic Cloud (LMC) (Seale et al., 2009). This archival dataset has been re-processed through an updated pipeline that can extract sources either with a full aperture extraction or through optimal extraction using a super-sampled point spread function (PSF) (Lebouteiller et al., 2015). The spectral analysis is presented here along with the catalog, cross-matched with photometric catalogs. Some of the work completed in this project was utilized in Jones et al. (2017), while the rest was used for verification and debugging of the optimal extraction pipeline.

A.1 Sample Overview

Seale et al. (2009) presented spectra of 294 sources in the LMC, taken by the Infrared Spectrograph (IRS) on board the *Spitzer Space Telescope*. The IRS is composed of four modules: two at low spectral resolution (R~ 60-100) from 5.5 to 38 μm (short-low and long-low, or SL and LL); and two at higher spectral resolution (R~600) from 9.9 to 37 μm (short-high and long-high, or SH and LH). The SL module has two configurations; SL1 provides spectra from 7.6-14.6 μm, while SL2 provides spectra from 5.2-8.4 μm. For each source Seale et al. (2009) used the SL, SH, and LH modules to obtain a spectrum from 5.5 to 37 μm.

277 of the objects in the sample display features characteristic of MYSOs,

while the remaining sources have been identified as more evolved stars, i.e. asymptotic giant branch (AGB) and post-AGB stars. The MYSO sources present a range of features, including polycyclic aromatic hydrocarbon (PAH) emission, silicate absorption, ice absorption, and fine-structure lines. A principle component analysis was performed to classify the sources based on the relative strength of the features, and the authors proposed an evolutionary sequence derived from the population statistics of each classification family.

YSOs are defined here as a young central source, possibly accompanied by a disk and and envelope system, which will evolve to form a main sequence star. While low-mass YSOs can be studied successfully in local galactic neighborhoods, studies of galactic massive YSOs present a variety of challenges. Their short lifetime and the nature of the stellar initial mass function make them quite rare; additionally, they typically form in the galactic plane, leading to severe dust obscuration and distance ambiguities. The LMC presents an ideal laboratory for studies of MYSOs; it is located at a known, roughly uniform distance of 50 kpc, and its face-on orientation with low galactic line-of-sight extinction provides a clear view of the entire system (Pietrzyński et al., 2013). The sample of MYSO spectra in the LMC provided by Seale et al. (2009) thus represent the most complete sample of MYSOs for a galaxy.

A.1.1 Sample Selection

The sample selection criteria adopted by Seale et al. (2009) was provided by Gruendl & Chu (2009), and it is briefly described here. All *Spitzer* archival LMC observations were collected, including the Legacy program Surveying the Agents

of a Galaxy's Evolution (SAGE; Meixner et al., 2006) as well as earlier programs targeting individual star-forming regions. All sources with point-source photometry have been extracted in every band of the Infrared Array Camera (IRAC, 3.6, 4.5, 5.8, and 8.0 μm) and the Multiband Imaging Photometer (MIPS) 24 and 70 μm bands. Objects were first selected on infrared excess via [4.5]–[8.0] versus [8.0] color magnitude diagram; next, a cut requiring [4.5]–[8.0]>2.0 was used to exclude main-sequence stars, giant stars, and most AGB stars. Note that this cut may remove evolved YSOs which have lost the majority of their natal dust shell.

A second cut is applied to remove background galaxies: [8.0]>14–([4.5]–[8.0]). This leaves 2910 sources as candidate YSOs. Gruendl & Chu (2009) added supporting observations to extend the spectral energy distributions into the near-infrared and optical; this adds Hα, $J-$, $H-$, and K_s- band, and incomplete $UBVI$ band data. Additional imaging data was used to investigate the source extent and neighborhood. Sources in the supporting catalogs were cross-correlated with the YSO candidates, and a positive match was considered to be within 1.0''. The supporting data enabled the sub-classification of the candidates into "Definite", "Probable", and "Possible" YSOs; of the 2910 candidates, 855 were considered definite, 317 as probable, and 213 as possible YSOs.

The sample of 294 sources selected by Seale et al. (2009) consisted of 269 labeled as definite or probable YSOs, including all sources in those two subsets for which [8.0]<8.0. They selected 25 additional sources with primary classifications other than YSOs due to their extreme or unique character, leading to the possibility of a prior mis-classification and their true nature as being a YSO.

A.1.2 Spectral Extraction and Stitching

The spectra were processed using the *Spitzer Science Center* data reduction pipeline. The data product is first cleaned using campaign-specific rogue pixel masks and frame-to-frame pixel variations using the `IRSCLEAN` package. Next, the background is subtracted; the method used differs between IRS modules due to the variation in slit sizes. For the long slit of SL, two nod positions are differenced to determine a local background, and this is subtracted from the source position. The SH and LH slits are not long enough to contain both the source and an independent background, so background observations are taken from nearby sky positions and differenced from the source location.

The spectra were extracted using either the full aperture (for SH and LH) or a tapered column extraction (for SL). For a full aperture extraction, any flux within the bounds of the pixel map at the given wavelength is extracted and summed. A tapered column extraction uses a window of wavelength-dependent width, according to the variation in the PSF, i.e. wider at longer wavelengths. Note that the window only applies a selection filter to the pixels; it does not weight pixel values according to an assumed PSF shape.

Next, spectral data from the separate modules are stitched together. Several corrections must be applied to the individual components for the stitch to be successful. First, fringing caused by the high-resolution detectors is removed with the `IRSFRINGE` package. Next, spectra are scaled to correct for flux discontinuities. First, SL1 is scaled to SL2; this factor has an average value of 0.98 with a standard deviation of 0.14. Next, LH is scaled to SH where they overlap, from 18.9-19.3 μm; the direction of scaling for this step is inconsequential, as the full high resolution spectrum is finally scaled to match the SL1+SL2 combined

spectrum in the region of overlap (9.9-14.6μm). The (SH+LH):(SL1+SL2) scale factors range from 0.5 to 2.0.

Scaling factors can be expected, as slit area varies substantially between modules. If the source fills both the SH and LH module slits, the scaling factor between the spectra should represent the ratio of slit areas. If the source were point-like, the scaling factor should be unity. That many sources require a non-unity scale factor suggests a common extended component, or significant background emission not well accounted for. Scaling may also be affected by variation in slit orientation or imprecise background subtraction and spectral extraction. If some aspects of the spectrum are point-like, e.g. fine structure lines emanating from a compact HII region, while the dust emission is extended, the scaling may be inappropriately applied to the line fluxes.

A.2 Optimal Extraction Method

Lebouteiller et al. (2015) presented a new extraction method for all high-resolution spectra taken by *Spitzer* in staring mode. They modify the approach above by introducing an automated decision tree with multiple spectral extraction options: full aperture extraction, or a variety of optimal extraction methods. The full aperture extraction method works similarly to the method listed above, and is typically only chosen as the extraction method for sources with highly extended spatial profiles.

The optimal extraction methods use the PSF profile to compare to the data profile in order to calculate the flux density. The key addition is the creation of a super-sampled PSF, which provides the spatial profile of a point-source

anywhere in the SH or LH apertures. The SH PSF was generated from mapping observations of Ξ Draconis, while the LH PSF used observations of Sirius; the mapping scanned across the entire field of the apertures at sub-pixel step size. Of note, the SH and LH apertures are fairly small with respect to the size of the PSF, and they miss a not-insignificant fraction of the PSF shape in any one observation. Because of this, multiple methods can be used to combine PSF data from the two nods of a given observation.

The standard optimal extraction technique scales the PSF to the data profile; however, this can be applied to the two nods individually (producing two spectra to be merged later) or simultaneously (using the improved data sampling of the source profile to produce a single, more accurate spectrum). The drawback of individual extraction is that few pixels are available to scale both the super-sampled PSF and large-scale background emission simultaneously (the details of which can be found in Lebouteiller et al., 2015). For simultaneous extraction, the automated pipeline assumes that the PSF scaling factor and the background emission are identical for a given wavelength and spectral order across both nod images.

Both extractions are used in the pipeline. First, each nod image is extracted individually to find the source position in each observation. The background is ignored during this step, as it doesn't strongly affect the source finder. Next the two nods are extracted simultaneously, using the source positions derived from the individual extractions. This results in a single source spectrum and a background spectrum.

In addition to the standard optimal extraction methods described above, a differential method is calculated. In the differential method, the two nod images

are differenced, resulting in pixel issues being cleanly removed. The differential source profile is then fit with a differential super-sampled PSF, created from a shifted pair of two normal super-sampled PSFs. The differencing removes any extended source emission, providing the spectrum of an unresolved source.

As such, the differential method is the best choice if the source is unresolved. If the source has any extended component, it will be removed and the flux will be underestimated. In the case of nearly point-like sources, the standard optimal extraction method works well to remove the background and increase signal-to-noise when compared to the full aperture extraction. If the source has significant extended components, it cannot be fit well with the PSF, and the full aperture extraction provides the best option.

A.3 YSO Spectra Analysis

With this array of spectral extraction options, we revisit the YSO sample studied in Seale et al. (2009) to determine which extraction method provides the best spectrum for each source. We aim to do this by comparing extracted spectra to photometry taken from catalogs of LMC infrared sources. In addition, we examine the amount of variation between spectra and variation in source extent, as determined by the optimal extraction pipeline source finder.

A.3.1 Photometric Catalogs

Photometric catalogs of sources in the LMC have been created from observations with the Spitzer Space Telescope and with the Wide-field Infrared Survey

Explorer (Meixner et al., 2006; Wright et al., 2010). Spitzer surveys of the LMC have been undertaken in all bands of the InfraRed Array Camera (IRAC; 3.6, 4.5, 5.8 & 8.0 μm) and the 24 & 70 μm bands of the Multiband Imaging Photometer (MIPS). Whitney et al. (2008) report on the YSO candidate survey portion of the SAGE Legacy program; they apply color-magnitude cuts to the SAGE Point Source Catalog and find roughly 1000 candidate YSOs. However, the point source restriction removes YSOs which have extended emission or reside in environments with interstellar and stellar contamination. In addition, they estimate the possibility of 55% contamination due to evolved stars and background galaxies.

Gruendl & Chu (2009) repeated the exercise, but instead of utilizing the SAGE Point Source Catalog, they perform aperture photometry of all archival IRAC and MIPS observations towards the LMC. They find that in the common color-magnitude space selected by both photometric catalogs, $\sim 2/3$ of their YSO candidates are missed in the Whitney et al. (2008) sample, due primarily to the restrictive point source requirement. This points to a high possibility of either extended source emission or complex, crowded environments in which these YSOs reside. Gruendl & Chu (2009) notes that the SAGE group analysis identified YSOs in a part of color-magnitude space that they ignored, containing fainter and more evolved YSOs.

The WISE survey mapped the entire sky in four bands, with two of interest here: W3, centered at 12 μm and W4, centered at 22 μm. Of note, Spitzer had a primary mirror diameter roughly twice as large as that of WISE, leading to angular resolution of the photometry products: IRAC 8.0$\mu m \approx 2''$; MIPS 24$\mu m \approx 6''$; W3 12$\mu m \approx 6.5''$; and W4 22$\mu m \approx 12''$. This may lead to inaccuracies of the

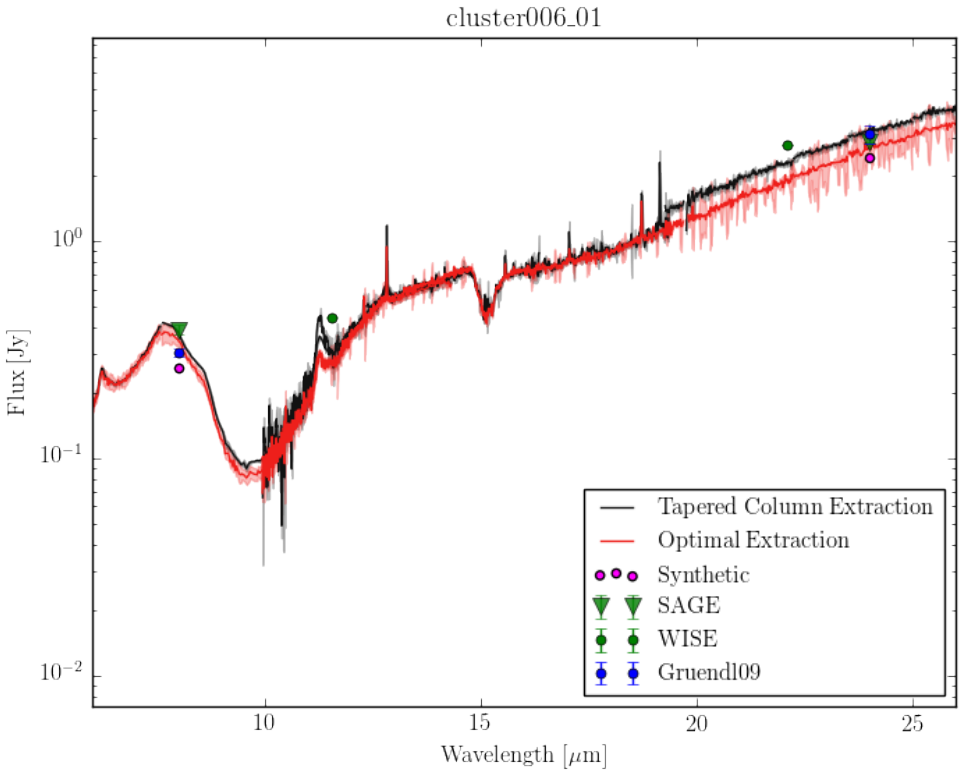

Figure A.1: Spectral extractions of the source named cluster006_01. The black spectrum shows a tapered column extraction, similar in method to the full aperture extraction but with better noise characteristics. The red spectrum shows the regular optimal extraction method, using the combined nods to generate a single spectrum. We also plot the photometry for the source, gathered with Spitzer (blue dots using aperture photometry, Gruendl & Chu (2009); green triangles using PSF-fitted point-source photometry, Meixner et al. (2006)) and WISE, in green circles. Additionally, we show synthetic photometry for the Spitzer 8 and 24 μm bands in magenta circles, generated by applying the photometric filter to the optimal extraction.

WISE photometry due to crowded fields or complex local emission structure.

A.3.2 Synthetic Photometry

Using the photometric filters of IRAC, MIPS and WISE, we can calculate the synthetic photometric magnitude of a spectrum and compare to the cross-matched

photometric catalog sources. Figure A.1 shows the spectral extractions and photometry of a typical source. We note that for conversion of the Spitzer photometric magnitudes to flux densities, MIPS assumes a Rayleigh-Jeans tail, while IRAC does not. This affects the derived magnitude by an appreciable amount.

A.3.3 Classification

We classify the sources based on a comparison of the photometry to the spectra and a comparison between the spectra. We begin with six classes: A, sources for which the spectral extractions and photometry all match; B, sources for which the optimal extraction more closely matches the photometry; C, sources for which the tapered column extraction more closely matches the photometry; D, sources for which the extractions are well-matched but the photometry is not a close match; E, sources for which photometry is not available; and F, for which no pairing produces a good match. Note that 'match' is defined by eye for these comparisons.

The classification is complicated by a variety of issues; the spatial extent of the sources appear to lie in a regime where observations pass from unresolved to partially resolved across the wavelength coverage of the IRS module, causing differences to appear between spectral extractions at short wavelengths. Additionally, some lie in crowded fields, causing inaccuracies in the background subtraction and the aperture photometry. The pairing of complex environments and possibly extended sources sometimes caused the optimal extraction to match the point-source photometry and the tapered column extraction to match the aperture photometry, with the two separate methods not

matching. These difficulties hampered the clean classification of sources, and the final attempt at classification added the class BC, for sources in which optimal extraction matched short wavelengths and tapered column extraction better matched long wavelengths. The full list of sources and classifications are given in Table A.1.

These classifications are the first step in a possible project to better characterize the sample of LMC YSO candidates. They were used to better understand the sources examined in Shimonishi et al. (2016a), as seven of the eleven YSOs studied are present in this spectral sample. They also provide ideal candidates for follow-up investigations with ALMA and JWST, i.e. Shimonishi et al. (2016b) and JWST GTO Observation Specifications under M. Meixner.

Table A.1: This table presents the YSO candidates observed by Seale et al. (2009), along with their cross-matched photometry from SAGE, Gruendl & Chu (2009), and WISE, and the classification derived here.

Object	RA	DEC	GC8μm	GC24μm	SAGE8μm	SAGE24μm	W3	W4	Class
cluster001_01	84.92449	-69.77002	5.93	0.04	6.048	0.745	3.414	-0.644	B
cluster001_02	84.997267	-69.757298	6.54	2.0	6.825	—	5.051	1.907	C
cluster001_03	84.930234	-69.648495	5.48	—	—	—	—	—	E
cluster001_04	84.934689	-69.646512	6.09	—	—	—	—	—	E
cluster001_05	84.941397	-69.644216	5.25	—	—	—	—	—	E
cluster001_06	84.932545	-69.642764	4.87	—	4.683	—	—	—	E
cluster001_07	82.926822	-68.58173	6.52	1.76	—	1.795	4.794	1.75	C
cluster002_01	81.694227	-68.81311	4.25	—	4.433	—	2.335	-0.821	E
cluster002_02	79.801047	-69.152017	4.9	—	5.061	—	3.626	0.437	E
cluster002_03	78.354503	-69.379182	5.53	—	—	—	3.377	-0.419	E
cluster002_04	78.323722	-69.373604	5.62	—	—	—	3.385	-0.63	E
cluster002_05	77.460545	-68.884858	5.24	—	5.291	-0.531	1.948	-1.803	A
cluster003_01	72.972026	-69.391291	4.04	—	4.643	—	—	—	E
cluster003_02	73.190057	-69.197081	4.39	0.61	4.549	0.699	3.333	0.863	A
cluster003_03	73.608564	-69.183975	5.6	—	—	—	3.795	-0.053	E
cluster004_01	83.218554	-69.771825	6.21	0.06	—	—	3.805	0.094	BC
cluster004_02	84.128372	-69.304765	6.5	1.89	6.633	1.866	5.069	2.016	A
cluster004_03	84.665368	-69.09394	6.06	—	—	—	—	—	F
cluster004_04	84.688101	-69.085529	6.06	—	—	—	—	—	F
cluster004_05	84.705276	-69.079001	5.96	—	—	—	—	—	F
cluster004_06	84.815683	-69.511084	—	—	—	0.536	3.927	-0.346	E
cluster004_07	84.911346	-69.651191	6.01	—	—	0.547	—	—	B
cluster004_08	84.912568	-69.653161	5.76	—	—	—	3.424	-0.242	E
cluster004_09	85.104795	-69.670023	—	—	—	1.064	3.808	0.162	E
cluster004_10	85.018314	-69.743779	5.4	—	—	-0.326	2.764	-0.861	C
cluster004_11	84.906686	-69.756946	6.13	—	—	-0.105	3.598	-0.071	B
cluster004_12	84.906375	-69.769389	5.82	-0.28	—	-0.059	3.226	-0.811	C
cluster004_13	84.879961	-70.204705	6.31	1.73	6.658	1.765	5.343	1.802	B
cluster005_01	78.339285	-69.378201	5.67	-0.19	—	-0.143	3.314	-0.619	BC
cluster005_02	78.35207	-69.180083	6.51	1.67	—	1.859	4.666	1.613	BC

Continued on next page

Table A.1 – continued from previous page

Object	RA	DEC	GC8μm	GC24μm	SAGE8μm	SAGE24μm	W3	W4	Class
cluster005_03	77.4697	-68.883515	5.86	—	—	—	3.172	-1.584	E
cluster006_01	82.726022	-68.574534	5.81	0.93	5.555	1.027	4.627	1.2	A
cluster006_02	81.267068	-68.473462	6.33	1.67	6.536	1.688	4.755	1.637	A
cluster006_03	80.552381	-67.975662	5.08	—	5.249	—	2.983	-0.935	E
cluster006_04	83.014352	-67.707141	5.43	0.16	5.684	—	3.892	0.463	B
cluster007_01	74.449863	-66.479093	—	—	5.704	2.179	4.647	1.577	C
cluster007_02	74.1968	-66.408822	—	—	—	1.462	4.445	0.767	E
cluster007_03	73.029025	-66.92122	6.06	0.3	—	—	3.793	0.041	D
cluster008_01	72.797448	-69.446309	6.67	0.99	—	1.127	—	—	A
cluster008_02	72.363699	-69.201737	6.7	0.64	—	0.94	3.765	0.083	D
cluster008_03	73.494047	-69.185192	6.72	0.81	7.319	1.137	5.056	1.121	D
cluster008_04	73.504741	-69.198023	6.96	0.7	—	2.181	—	—	D
cluster008_05	73.500404	-69.198744	6.7	—	7.054	—	4.588	0.657	E
cluster008_06	74.290535	-68.746707	6.44	1.33	—	1.397	—	—	D
cluster008_07	73.242038	-68.060008	6.53	1.36	7.068	1.525	5.252	1.559	A
cluster009_01	76.166076	-70.905256	6.95	0.85	—	—	5.107	0.938	BC
cluster009_02	76.149357	-70.908354	6.56	1.83	6.767	2.246	4.94	0.6	B
cluster009_03	76.158692	-70.911966	—	—	—	0.775	4.186	0.372	E
cluster010_01	80.603723	-69.709109	6.56	0.86	—	0.852	4.762	1.034	BC
cluster010_02	79.764233	-69.636909	7.39	—	—	2.071	4.904	1.071	C
cluster010_03	78.424342	-69.591224	—	—	—	2.087	5.737	2.358	E
cluster010_04	78.329754	-69.364161	6.78	1.78	—	1.676	4.721	1.045	C
cluster010_05	77.600343	-70.235148	6.42	2.1	6.66	2.108	5.359	2.295	A
cluster010_06	78.315556	-69.359956	6.97	2.09	—	2.309	5.235	1.565	C
cluster010_07	77.467733	-68.890906	6.82	0.55	—	0.993	3.898	-0.406	BC
cluster011_01	78.464631	-67.456087	6.25	—	6.746	0.2	4.048	0.271	A
cluster011_02	79.377742	-66.727038	6.93	0.98	7.257	—	5.152	0.964	A
cluster011_03	80.069611	-66.881691	—	—	—	1.643	5.757	1.826	E
cluster011_04	81.455292	-66.252404	5.94	—	6.294	—	3.99	-0.31	E
cluster011_05	80.707805	-66.68225	6.43	1.92	—	1.864	5.599	2.085	BC
cluster011_06	79.368469	-66.718606	6.89	1.42	7.311	1.485	5.635	1.594	B
cluster012_01	84.719429	-69.077061	6.98	—	—	—	3.064	-2.442	E
cluster012_02	84.663458	-69.097831	6.93	—	—	—	—	—	E

Continued on next page

Table A.1 – continued from previous page

Object	RA	DEC	GC8μm	GC24μm	SAGE8μm	SAGE24μm	W3	W4	Class
cluster012_03	84.997982	-69.62511	6.72	1.97	7.063	1.949	5.029	1.799	B
cluster012_04	84.904336	-69.760193	6.6	0.51	—	0.934	4.214	0.116	B
cluster012_05	85.002887	-69.787052	6.89	1.72	—	1.474	5.017	1.396	C
cluster012_06	86.333468	-69.779107	6.65	0.89	—	1.079	5.286	1.152	BC
cluster012_07	86.36633	-69.772938	6.85	1.53	—	1.355	4.786	1.45	BC
cluster012_08	87.159301	-70.035584	6.61	0.83	—	—	5.3	1.15	BC
cluster013_01	76.334452	-66.918477	6.31	0.42	—	—	4.832	0.765	BC
cluster013_02	74.169918	-66.541792	6.61	2.43	6.946	2.363	5.68	2.42	B
cluster013_03	73.960891	-66.576263	6.74	2.13	7.152	2.063	5.629	2.248	B
cluster013_04	73.03839	-66.922748	6.7	0.4	—	1.232	3.627	0.426	F
cluster013_05	74.238539	-66.420262	6.82	1.57	—	1.744	5.646	1.573	BC
cluster014_01	83.425609	-68.767457	6.83	0.8	—	—	3.907	0.204	BC
cluster014_02	82.976788	-68.444602	6.99	1.71	—	1.61	5.439	1.677	BC
cluster014_03	80.931143	-68.009406	6.76	0.96	—	—	4.994	1.177	BC
cluster014_04	80.582033	-68.077059	6.84	1.82	—	1.765	4.953	1.769	C
cluster014_05	83.217895	-67.68582	6.91	2.14	7.207	2.21	5.57	2.326	B
cluster015_01	84.768387	-69.070512	7.53	2.36	—	4.028	4.784	0.274	F
cluster015_02	84.523515	-69.15269	7.25	2.04	7.409	2.24	5.633	1.668	B
cluster015_03	85.039577	-69.673054	7.82	—	—	1.799	4.644	1.018	C
cluster015_04	84.938225	-69.747326	7.44	1.65	—	1.25	5.327	1.547	C
cluster015_05	84.965009	-69.752907	—	—	—	—	—	—	E
cluster015_06	84.871684	-69.788607	7.2	1.12	—	1.099	4.632	1.175	BC
cluster015_07	84.967879	-69.754572	8.14	—	—	—	—	—	E
cluster015_08	85.039538	-69.748183	7.31	1.46	—	1.975	3.529	-0.863	F
cluster015_09	87.075646	-70.019157	7.08	1.29	—	1.342	—	—	A
cluster016_01	84.972634	-71.164733	7.39	1.14	—	—	4.872	1.255	B
cluster016_02	84.981915	-71.166914	7.05	1.67	—	1.269	4.745	0.365	C
cluster016_03	84.993287	-71.16819	7.06	1.88	7.165	2.139	4.907	0.605	B
cluster016_04	84.993825	-71.170714	7.46	1.75	7.669	1.753	—	—	B
cluster016_05	85.411511	-71.320527	7.54	2.42	—	2.692	—	—	BC
cluster016_06	82.84517	-71.069403	7.48	1.88	—	1.953	4.562	0.737	C
cluster016_07	79.394681	-71.249025	7.27	2.43	—	2.422	5.141	1.979	C
cluster017_01	81.097459	-69.651308	7.32	2.35	—	2.371	5.707	2.115	BC

Continued on next page

Table A.1 – continued from previous page

Object	RA	DEC	GC8μm	GC24μm	SAGE8μm	SAGE24μm	W3	W4	Class
cluster017_02	80.889149	-69.620047	7.23	2.12	7.287	2.137	5.215	1.898	A
cluster017_03	79.820266	-69.632634	7.03	2.23	7.478	2.327	5.612	1.838	B
cluster017_04	79.780443	-69.644992	7.33	2.0	—	2.296	4.829	1.333	C
cluster017_05	78.409719	-69.38352	7.44	2.36	—	2.167	5.775	2.013	C
cluster017_06	77.310484	-68.504735	7.57	1.74	—	1.772	—	—	BC
cluster018_01	79.777858	-68.3604	7.1	2.28	—	2.225	—	—	C
cluster018_02	80.729664	-68.069266	7.64	2.3	—	—	4.938	0.716	B
cluster018_03	80.508784	-67.964884	7.68	1.97	—	2.339	4.673	0.804	B
cluster018_04	80.9585	-67.955443	7.63	1.18	7.985	1.265	—	—	A
cluster018_05	80.898083	-67.876554	7.6	2.13	7.76	2.152	6.134	2.267	A
cluster018_06	80.341613	-67.791356	7.45	1.74	—	1.664	5.823	1.759	BC
cluster018_07	83.850225	-67.582099	7.48	1.76	—	2.268	3.813	-0.194	F
cluster018_08	83.21457	-67.683169	7.09	2.12	—	2.212	5.168	1.483	C
cluster018_09	83.114237	-67.692474	7.16	—	—	—	—	—	E
cluster019_01	75.950723	-67.307775	7.26	2.34	—	2.16	—	—	BC
cluster019_02	73.515045	-67.271794	7.39	1.63	7.749	1.678	5.927	1.9	A
cluster019_03	73.244468	-68.048891	7.02	2.31	—	2.39	5.271	2.117	BC
cluster019_04	73.86127	-68.424615	7.24	2.3	—	2.196	5.834	2.358	BC
cluster020_01	83.015934	-67.715781	7.64	2.51	—	2.519	6.502	2.018	BC
cluster020_02	81.931099	-67.440052	7.23	2.48	—	2.532	—	—	BC
cluster020_03	83.133586	-66.454205	7.27	2.32	—	2.491	5.149	1.443	BC
cluster020_05	79.421002	-66.705222	7.53	—	—	2.3	6.078	2.244	BC
cluster021_01	76.023341	-68.394533	7.65	3.63	7.745	3.639	5.919	3.653	A
cluster021_02	75.631201	-68.093268	7.26	3.06	7.297	3.081	5.553	3.131	A
cluster021_03	74.312399	-68.441531	7.22	—	—	2.188	4.584	0.904	C
cluster021_04	74.320084	-68.446664	7.71	2.87	—	3.155	—	—	BC
cluster021_05	75.982796	-67.345841	7.45	2.95	—	2.82	5.836	2.844	BC
cluster021_06	75.983462	-67.312552	7.54	2.93	—	2.803	4.39	2.445	C
cluster021_08	73.523911	-66.751998	6.43	2.65	6.501	2.609	5.453	2.742	A
cluster022_01	73.777099	-69.285781	6.37	—	6.772	2.181	5.025	2.746	D
cluster022_02	73.512645	-69.194364	7.69	—	—	—	4.495	0.566	E
cluster022_03	73.004793	-69.335477	7.41	2.96	7.528	3.06	5.787	2.724	A
cluster022_04	73.019	-69.346218	7.62	2.73	—	2.581	—	—	BC

Continued on next page

Table A.1 – continued from previous page

Object	RA	DEC	GC8μm	GC24μm	SAGE8μm	SAGE24μm	W3	W4	Class
cluster022_05	73.001784	-69.395166	7.53	1.97	—	2.045	5.148	-0.227	C
cluster022_06	72.750648	-69.326223	7.48	2.98	—	3.206	5.907	2.951	BC
cluster022_07	72.226684	-69.163418	7.24	1.77	7.639	1.694	5.428	1.742	B
cluster023_01	83.542647	-67.424833	7.56	3.2	7.938	3.028	—	—	A
cluster023_02	82.731489	-67.335053	7.07	3.06	7.403	3.042	6.155	3.086	A
cluster023_03	81.987859	-67.422864	7.43	3.11	—	3.157	6.129	2.655	C
cluster023_04	81.903876	-67.457946	7.45	3.16	7.506	3.048	5.772	2.389	C
cluster023_06	81.627682	-67.676873	6.94	3.03	—	3.006	6.071	3.181	BC
cluster023_07	80.541983	-67.583216	7.58	2.95	—	2.861	6.511	3.065	BC
cluster023_08	78.499308	-67.380936	7.14	2.8	7.45	2.749	5.629	2.443	A
cluster024_01	81.590601	-68.666404	7.41	2.84	—	2.78	—	—	BC
cluster024_02	79.787557	-69.198923	7.47	3.1	7.636	3.063	5.899	2.896	A
cluster024_03	78.420472	-69.383778	7.3	3.08	7.461	2.874	5.763	2.092	B
cluster024_04	78.437441	-69.586278	7.47	2.91	—	2.834	6.147	2.612	BC
cluster024_05	77.454617	-68.875152	7.1	3.42	7.29	4.751	5.471	1.267	D
cluster024_06	80.72197	-69.853084	7.62	3.17	—	3.21	5.685	2.569	C
cluster024_07	79.548738	-70.507505	7.61	2.82	7.612	2.823	5.366	2.887	A
cluster024_08	77.598693	-69.438925	7.49	3.08	—	3.038	6.215	3.045	BC
cluster025_01	83.903624	-69.203907	7.11	3.25	7.299	3.157	5.661	2.727	B
cluster025_02	84.724493	-69.158683	7.48	2.58	—	2.667	6.834	2.855	A
cluster025_03	84.770316	-69.497197	7.59	2.84	—	3.175	5.184	1.23	B
cluster025_04	84.899934	-69.767803	6.84	—	—	2.109	—	—	B
cluster025_05	83.97647	-69.646686	7.54	—	—	—	—	—	E
cluster025_06	85.876379	-69.412931	6.37	2.56	6.456	2.557	5.15	2.628	A
cluster025_07	85.703723	-69.746194	7.61	3.13	—	3.035	6.296	3.056	D
cluster025_08	87.608683	-69.934186	6.94	3.1	7.044	3.124	4.848	2.793	D
cluster026_01	83.06234	-71.223296	7.5	2.75	—	2.699	5.769	2.747	F
cluster026_02	85.406557	-71.317218	7.55	—	—	2.15	4.714	1.278	C
cluster026_03	86.80405	-70.738015	7.14	3.18	7.202	3.114	5.81	3.327	A
cluster026_04	85.187393	-70.468604	7.1	2.73	—	2.586	5.686	2.787	A
cluster026_05	85.640437	-71.291064	7.47	2.48	7.795	2.491	6.305	2.682	A
cluster027_01	80.593616	-71.592283	7.64	2.76	7.757	2.818	6.191	2.88	A
cluster027_02	77.424708	-71.461684	7.68	3.21	—	3.077	6.554	3.266	C

Continued on next page

Table A.1 – continued from previous page

Object	RA	DEC	GC8μm	GC24μm	SAGE8μm	SAGE24μm	W3	W4	Class
cluster027_04	76.103401	-70.728781	7.44	2.28	—	2.208	5.873	2.145	BC
cluster028_01	79.701502	-69.559623	7.11	3.32	7.19	3.339	5.597	3.406	A
cluster028_02	79.774708	-69.644778	7.5	—	—	2.375	—	—	C
cluster028_03	81.419297	-70.14089	7.8	3.82	7.885	3.77	6.136	3.855	A
cluster028_04	78.072164	-70.455104	7.52	3.28	7.912	3.22	6.504	3.395	A
cluster029_01	84.065963	-69.530972	7.26	3.58	7.775	3.673	5.81	3.082	C
cluster029_02	84.478427	-69.576608	7.75	3.32	7.951	3.21	6.438	3.39	A
cluster029_03	85.141533	-69.419412	6.52	3.44	6.549	3.466	5.65	3.555	A
cluster029_04	84.91311	-69.2985	7.76	1.72	—	1.692	5.803	1.857	BC
cluster029_05	84.743421	-69.0763	7.71	—	—	3.692	—	—	F
cluster029_06	87.109214	-70.147285	7.67	3.39	8.211	3.273	6.195	3.347	D
cluster029_07	83.631054	-68.587179	7.74	3.33	—	3.162	6.253	3.227	A
cluster029_08	85.183462	-69.43184	7.36	3.41	—	3.324	5.838	3.194	C
cluster029_09	86.62218	-69.587271	7.57	3.44	—	3.268	6.025	3.025	C
cluster030_01	86.206767	-67.326311	7.66	3.43	—	3.309	6.571	3.488	BC
cluster030_02	86.436579	-67.157828	7.63	3.41	7.79	3.314	6.023	2.933	A
cluster030_03	84.317847	-66.448512	7.7	3.65	—	3.358	6.444	3.609	C
cluster031_01	75.214389	-66.399969	6.79	2.91	—	2.914	6.027	3.058	BC
cluster031_02	74.448645	-66.471356	7.58	2.7	7.759	2.496	5.677	1.418	B
cluster031_03	74.317697	-66.388852	7.17	1.54	—	1.593	4.528	1.322	C
cluster031_04	74.72625	-66.121901	7.17	3.6	7.203	3.614	6.228	3.691	A
cluster031_05	73.493949	-66.789671	—	—	—	3.07	6.295	3.19	E
cluster031_06	73.022446	-66.920497	7.74	—	—	—	—	—	E
cluster032_01	82.407852	-72.831364	7.09	3.81	7.275	4.01	5.491	3.649	A
cluster032_03	80.688005	-71.602813	6.93	3.59	—	3.492	6.025	3.678	A
cluster032_04	83.032589	-71.226764	7.66	3.68	—	3.649	6.786	3.818	A
cluster032_05	84.967126	-71.158519	7.24	—	—	3.036	5.556	2.062	C
cluster033_01	83.104049	-68.651123	7.59	4.13	—	4.085	6.752	4.098	C
cluster033_02	84.442004	-69.180642	7.71	4.04	—	4.088	5.426	1.266	F
cluster033_03	83.184353	-69.501588	7.73	4.04	—	3.954	6.844	4.15	BC
cluster033_04	81.620852	-69.298909	7.61	3.67	—	3.625	6.26	3.577	C
cluster033_05	80.90782	-69.648451	7.26	3.7	7.411	3.564	6.495	3.691	A
cluster033_06	80.321819	-69.997282	7.61	3.98	—	3.858	6.28	3.961	BC

Continued on next page

Table A.1 – continued from previous page

Object	RA	DEC	GC8μm	GC24μm	SAGE8μm	SAGE24μm	W3	W4	Class
cluster034_01	73.534534	-66.775387	7.38	4.1	—	4.042	6.612	4.241	A
cluster034_02	73.037257	-66.92705	7.6	—	7.976	—	—	—	E
cluster035_01	82.543033	-69.159402	7.14	4.34	7.215	4.298	6.171	4.352	A
cluster035_02	85.226089	-69.555188	7.62	3.75	7.651	3.715	6.033	3.716	A
cluster035_03	82.596564	-71.098977	7.71	3.9	—	3.714	6.563	3.689	C
cluster036_01	82.019874	-68.996449	7.7	4.87	—	4.976	6.659	4.784	C
cluster036_02	84.776303	-69.512169	7.71	4.79	—	5.228	6.344	2.243	B
cluster036_03	85.01745	-69.636781	7.66	—	—	—	5.677	2.515	E
cluster037_01	77.474539	-68.893522	7.85	1.6	—	2.263	—	—	B
cluster037_02	80.446211	-67.949101	7.87	2.44	8.269	2.572	6.552	2.273	A
cluster037_03	80.513745	-67.963047	8.36	1.84	—	2.751	4.579	0.449	B
cluster037_04	80.520201	-67.966742	8.53	2.09	—	—	—	—	F
cluster037_05	80.813253	-68.004743	9.13	2.27	—	2.467	5.586	1.492	BC
cluster037_06	80.511319	-67.783903	7.77	1.9	—	1.843	6.184	1.958	BC
cluster038_01	71.822903	-69.158411	7.84	2.2	7.897	2.231	6.519	2.387	A
cluster038_02	74.332381	-68.423989	7.91	2.52	—	3.099	5.394	1.413	B
cluster039_01	75.067418	-66.258688	7.95	2.07	8.161	2.08	6.01	2.225	A
cluster039_02	74.676942	-66.14324	8.87	2.94	8.925	2.923	7.313	3.257	A
cluster039_03	74.548741	-66.369804	8.57	3.26	—	3.181	6.891	2.938	BC
cluster039_04	74.424988	-66.442885	7.75	3.33	—	3.205	5.768	2.195	C
cluster039_05	74.455076	-66.483412	7.97	3.01	8.398	3.127	—	—	B
cluster039_06	73.526766	-66.76705	8.11	2.44	—	2.25	6.279	2.458	B
cluster039_07	74.270958	-66.709937	8.18	3.48	—	3.35	7.006	3.585	BC
cluster039_08	74.094197	-66.615796	8.16	2.68	8.404	2.586	6.436	2.82	A
cluster039_09	73.851569	-66.52163	8.3	3.63	8.46	3.574	7.072	3.816	A
cluster040_01	83.072864	-67.698774	7.75	2.79	—	2.681	5.686	1.642	C
cluster040_02	82.013307	-67.423767	7.82	3.12	—	2.961	6.436	2.605	C
cluster040_03	81.50498	-67.503356	7.83	3.17	8.13	3.148	6.592	3.309	A
cluster040_04	81.660617	-67.656441	7.92	3.16	—	3.033	6.56	3.261	BC
cluster041_01	80.353747	-66.070244	7.82	2.69	8.214	2.656	6.758	2.819	A
cluster041_02	79.280226	-65.992631	7.76	3.3	—	3.244	6.958	3.469	A
cluster041_03	80.388335	-65.489101	6.94	1.53	—	1.81	—	—	BC
cluster042_01	82.586598	-71.127378	7.94	2.67	—	3.107	5.868	2.305	B

Continued on next page

Table A.1 – continued from previous page

Object	RA	DEC	GC8μm	GC24μm	SAGE8μm	SAGE24μm	W3	W4	Class
cluster042_02	82.584652	-71.13024	7.78	3.02	—	3.627	5.681	1.956	B
cluster042_03	85.358132	-71.298297	7.99	3.25	—	3.205	6.94	3.363	BC
cluster043_01	79.889422	-69.685187	7.93	2.94	—	2.973	6.839	3.0	BC
cluster043_02	78.76357	-70.564161	7.81	3.59	—	3.43	6.563	3.604	A
cluster043_03	77.144648	-69.423626	7.92	3.45	—	3.382	6.843	3.481	BC
cluster044_01	80.785832	-68.001801	8.75	3.43	8.999	3.062	6.958	2.844	C
cluster044_02	80.53028	-67.972129	8.0	2.81	—	3.435	—	—	BC
cluster044_03	80.487368	-67.950018	10.03	3.44	—	4.147	6.38	2.414	B
cluster044_04	81.338166	-67.493763	7.85	3.43	—	3.595	6.304	3.002	BC
cluster044_05	80.049815	-66.877458	7.47	3.54	—	3.488	6.477	3.441	BC
cluster045_01	80.193963	-67.88194	7.83	3.77	—	3.755	7.152	4.02	A
cluster045_02	78.536061	-67.386182	7.81	3.82	—	3.705	6.869	3.879	A
cluster045_03	77.47762	-68.829771	7.9	3.72	—	3.645	6.939	3.86	BC
cluster046_01	80.048162	-68.631577	7.76	4.04	—	3.921	6.782	4.17	BC
cluster046_02	80.736626	-68.068542	7.77	—	—	3.811	—	—	C
cluster046_03	78.475233	-67.338572	6.94	4.13	7.321	3.928	6.122	4.144	A
cluster047_01	80.570275	-68.067746	8.51	3.94	8.81	3.974	6.692	3.545	B
cluster047_02	80.632159	-68.055325	8.38	3.77	—	3.601	6.856	3.596	C
cluster047_03	80.704702	-68.024741	8.13	4.12	—	—	7.045	3.54	C
cluster047_04	80.615401	-67.903545	8.55	4.18	—	4.122	6.521	3.31	C
cluster047_05	81.623334	-67.69574	7.91	4.58	—	4.477	6.921	4.551	A
cluster047_07	81.423058	-66.257933	7.91	3.79	—	3.652	6.605	3.535	C
cluster048_01	81.521918	-68.602575	7.86	4.4	7.96	4.438	6.551	4.303	A
cluster048_02	80.38843	-69.672192	7.89	—	—	—	—	—	E
cluster048_03	79.820727	-69.63788	7.98	—	—	3.943	6.042	2.519	C
cluster048_04	80.339577	-69.983856	7.85	3.75	—	3.722	6.603	3.608	BC
cluster048_05	78.249215	-69.576905	7.95	4.52	—	4.457	7.224	4.625	BC
cluster048_06	78.326067	-69.359848	7.98	—	—	—	—	—	E
cluster049_01	85.588146	-69.105825	7.99	4.23	8.381	4.312	7.112	4.078	B
cluster049_02	83.978888	-69.65083	7.76	—	—	—	—	—	E
cluster049_03	85.049993	-70.154442	7.97	4.17	—	4.166	7.097	4.27	BC
cluster050_01	75.983866	-67.344103	7.86	—	—	—	—	—	E
cluster050_02	78.689305	-67.201156	7.88	4.31	—	4.283	6.608	4.028	C

Continued on next page

Table A.1 – continued from previous page

Object	RA	DEC	GC8μm	GC24μm	SAGE8μm	SAGE24μm	W3	W4	Class
cluster050_03	79.225213	-67.334745	7.64	4.28	7.715	4.166	6.38	3.846	A
cluster051_01	74.449876	-66.311773	8.63	4.32	—	4.252	7.632	4.403	A
cluster051_02	74.24936	-66.407189	8.2	3.89	8.375	6.02	6.544	3.294	B
cluster051_03	74.161487	-66.412828	8.84	4.46	—	4.573	—	—	F
cluster051_04	74.21591	-66.52583	9.86	4.49	—	4.552	7.374	4.008	A
cluster051_05	74.120902	-66.533132	7.85	3.67	—	3.433	5.84	3.111	BC
cluster051_06	74.10828	-66.532075	8.29	3.8	—	3.751	5.981	3.154	C
cluster051_07	73.916694	-66.573383	9.35	4.56	—	4.626	7.824	4.329	A
cluster051_08	73.905321	-66.573049	8.61	4.18	—	4.052	7.586	4.245	A
cluster052_01	72.539651	-69.485108	7.96	—	—	4.337	6.662	4.121	D
cluster052_02	72.207696	-69.158484	7.93	4.45	—	4.276	6.749	4.055	C
cluster053_01	84.17672	-70.129636	7.97	4.93	—	4.948	6.824	4.92	A
cluster053_02	85.232373	-69.679792	7.94	5.66	—	5.752	7.444	5.889	A
cluster054_01	78.123685	-67.155134	7.71	4.81	8.205	5.112	6.818	5.044	B
cluster054_02	77.625398	-67.142576	7.91	4.67	8.142	4.595	7.119	4.672	A
cluster054_03	75.008431	-66.503183	8.78	4.94	—	4.935	7.841	5.068	A
cluster054_04	74.336312	-66.470659	9.28	5.41	—	5.797	7.849	4.945	C
cluster054_05	73.943313	-66.419186	9.82	5.5	9.865	5.445	7.714	4.885	D
cluster054_06	73.92691	-66.57383	9.66	5.47	9.943	5.789	7.629	4.963	B
cluster054_07	73.923281	-66.576131	9.7	4.9	—	5.082	—	—	B
cluster054_08	74.306121	-66.316683	9.19	5.44	—	5.535	8.243	5.547	A
cluster054_09	75.025877	-66.265769	9.05	5.07	—	5.094	7.493	4.547	D
cluster054_10	74.715107	-66.162377	10.69	5.4	10.828	5.524	8.66	5.397	F
cluster055_01	80.322855	-68.034553	8.73	5.34	—	5.397	7.705	5.281	A
cluster055_02	80.636037	-68.050465	9.04	4.38	—	4.096	7.166	3.471	B
cluster055_03	80.880702	-68.018879	8.44	4.38	—	4.519	6.499	3.98	D
cluster055_04	80.674864	-67.916794	10.18	5.33	—	5.375	8.093	4.886	C
cluster055_05	80.620739	-67.894242	8.97	5.37	—	5.822	8.606	4.449	F
cluster055_06	80.536526	-67.890242	9.17	5.56	9.522	5.561	8.386	5.139	A
cluster055_07	80.424319	-67.889994	9.24	5.35	—	5.338	7.822	4.756	B
cluster055_08	80.479903	-67.791767	9.35	4.96	9.569	4.975	8.39	4.963	A
single001_01	80.582161	-65.721953	5.98	4.12	6.075	4.186	5.271	4.035	A
single002_01	84.269903	-66.368661	7.76	—	—	4.526	—	—	C

BIBLIOGRAPHY

Abdo A. A. et al., 2010a, A&A, 512, A7

Abdo A. A. et al., 2010b, A&A, 523, A46

Acharyya K., Hassel G. E., Herbst E., 2011, ApJ, 732, 73

Acharyya K., Herbst E., 2015, ApJ, 812, 142

Acharyya K., Herbst E., 2016, ApJ, 822, 105

Aikawa Y., Wakelam V., Garrod R. T., Herbst E., 2008, ApJ, 674, 984

Belloche A., Garrod R. T., Müller H. S. P., Menten K. M., 2015, in Astronomical Society of the Pacific Conference Series, Vol. 499, Revolution in Astronomy with ALMA: The Third Year, Iono D., Tatematsu K., Wootten A., Testi L., eds., p. 181

Belloche A., Garrod R. T., Müller H. S. P., Menten K. M., Comito C., Schilke P., 2009, A&A, 499, 215

Bernard J.-P. et al., 2008, AJ, 136, 919

Boogert A. C. A., Ehrenfreund P., 2004, in Astronomical Society of the Pacific Conference Series, Vol. 309, Astrophysics of Dust, Witt A. N., Clayton G. C., Draine B. T., eds., p. 547

Boogert A. C. A. et al., 2008, ApJ, 678, 985

Brooke T. Y., Sellgren K., Geballe T. R., 1999, ApJ, 517, 883

Brown P. D., Charnley S. B., Millar T. J., 1988, MNRAS, 231, 409

Buhl D., Snyder L. E., 1970, Nature, 228, 267

Caldwell D. A., 1997, PhD thesis, RENSSELAER POLYTECHNIC INSTITUTE

Cardelli J. A., Clayton G. C., Mathis J. S., 1989, ApJ, 345, 245

Cheung A. C., Rank D. M., Townes C. H., 1969, Nature, 221, 917

Cheung A. C., Rank D. M., Townes C. H., Thornton D. D., Welch W. J., 1968, Physical Review Letters, 21, 1701

Cheung A. C., Rank D. M., Townes C. H., Thornton D. D., Welch W. J., 1969, Nature, 221, 626

Chiar J. E., Adamson A. J., Kerr T. H., Whittet D. C. B., 1995, ApJ, 455, 234

Chiar J. E., Gerakines P. A., Whittet D. C. B., Pendleton Y. J., Tielens A. G. G. M., Adamson A. J., Boogert A. C. A., 1998, ApJ, 498, 716

Chin Y.-N., Henkel C., Millar T. J., Whiteoak J. B., Marx-Zimmer M., 1998, A&A, 330, 901

Cleeves L. I., Adams F. C., Bergin E. A., 2013, ApJ, 772, 5

Cohen S. A., 1976, Nature, 261, 215

Collings M. P., Anderson M. A., Chen R., Dever J. W., Viti S., Williams D. A., McCoustra M. R. S., 2004, MNRAS, 354, 1133

Collings M. P., Dever J. W., Fraser H. J., McCoustra M. R. S., 2003a, **??**jnlAp&SS, 285, 633

Collings M. P., Dever J. W., Fraser H. J., McCoustra M. R. S., Williams D. A., 2003b, ApJ, 583, 1058

Cook A. M., Whittet D. C. B., Shenoy S. S., Gerakines P. A., White D. W., Chiar J. E., 2011, ApJ, 730, 124

Costagliola F. et al., 2015, A&A, 582, A91

Cuppen H. M., Morata O., Herbst E., 2006, MNRAS, 367, 1757

Cuppen H. M., van Dishoeck E. F., Herbst E., Tielens A. G. G. M., 2009, A&A, 508, 275

Dartois E., Schutte W., Geballe T. R., Demyk K., Ehrenfreund P., D'Hendecourt L., 1999, A&A, 342, L32

D'Hendecourt L. B., Jourdain de Muizon M., 1989, A&A, 223, L5

Draine B. T., Lee H. M., 1984, ApJ, 285, 89

Fayolle E. C., Öberg K. I., Cuppen H. M., Visser R., Linnartz H., 2011, A&A, 529, A74

Fuchs G. W., Cuppen H. M., Ioppolo S., Romanzin C., Bisschop S. E., Andersson S., van Dishoeck E. F., Linnartz H., 2009, A&A, 505, 629

Galametz M. et al., 2013, MNRAS, 431, 1596

Garrod R. T., 2008, A&A, 491, 239

Garrod R. T., 2013, ApJ, 765, 60

Garrod R. T., Belloche A., Müller H. S. P., Menten K. M., 2017, A&A, 601, A48

Garrod R. T., Herbst E., 2006, A&A, 457, 927

Garrod R. T., Pauly T., 2011, ApJ, 735, 15

Garrod R. T., Wakelam V., Herbst E., 2007, A&A, 467, 1103

Garrod R. T., Widicus Weaver S. L., Herbst E., 2008, ApJ, 682, 283

Geppert W. D. et al., 2006, Faraday Discussions, 133, 177

Gerakines P. A. et al., 1999, ApJ, 522, 357

Gibb E. L., Whittet D. C. B., Boogert A. C. A., Tielens A. G. G. M., 2004, ApJS, 151, 35

Gibb E. L. et al., 2000, ApJ, 536, 347

Gillett F. C., Forrest W. J., 1973, ApJ, 179, 483

Gould R. J., Salpeter E. E., 1963, ApJ, 138, 393

Gruendl R. A., Chu Y.-H., 2009, ApJS, 184, 172

Harper M., Weinstein B., Simon C., chebee7i, Swanson-Hysell N., Badger T. G., Greco M., Zuidhof G., 2015, python-ternary: Ternary plots in python

Hasegawa T. I., Herbst E., 1993, MNRAS, 263, 589

Hasegawa T. I., Herbst E., Leung C. M., 1992, ApJS, 82, 167

Heikkilä A., Johansson L. E. B., Olofsson H., 1999, A&A, 344, 817

Helmich F. P., van Dishoeck E. F., 1997, A&AS, 124

Herbst E., Klemperer W., 1973, ApJ, 185, 505

Herbst E., Klemperer W., 1974, ApJ, 188, 255

Hollenbach D., Salpeter E. E., 1971, ApJ, 163, 155

Jones O. C. et al., 2017, MNRAS, 470, 3250

Jørgensen J. K. et al., 2016, A&A, 595, A117

Krügel E., 2003, The physics of interstellar dust. IOP Publishing Ltd.

Kurt C. M., Dufour R. J., 1998, in Revista Mexicana de Astronomia y Astrofisica Conference Series, Vol. 7, Revista Mexicana de Astronomia y Astrofisica Conference Series, Dufour R. J., Torres-Peimbert S., eds., p. 202

Le Teuff Y. H., Millar T. J., Markwick A. J., 2000, A&AS, 146, 157

Lebouteiller V., Barry D. J., Goes C., Sloan G. C., Spoon H. W. W., Weedman D. W., Bernard-Salas J., Houck J. R., 2015, ApJS, 218, 21

Lee H.-H., Herbst E., Pineau des Forets G., Roueff E., Le Bourlot J., 1996, A&A, 311, 690

Madau P., Dickinson M., 2014, ARA&A, 52, 415

Madden S. C., Cormier D., Rémy-Ruyer A., 2016, in IAU Symposium, Vol. 315, From Interstellar Clouds to Star-Forming Galaxies: Universal Processes?, Jablonka P., André P., van der Tak F., eds., pp. 191–198

Madden S. C., Rémy A., Galliano F., Galametz M., Bendo G., Cormier D., Lebouteiller V., Hony S., 2012, in IAU Symposium, Vol. 284, The Spectral Energy Distribution of Galaxies - SED 2011, Tuffs R. J., Popescu C. C., eds., pp. 141–148

Mathis J. S., 1990, ARA&A, 28, 37

Mathis J. S., Rumpl W., Nordsieck K. H., 1977, ApJ, 217, 425

Meixner M. et al., 2006, AJ, 132, 2268

Merrill K. M., Russell R. W., Soifer B. T., 1976, ApJ, 207, 763

Millar T. J., Bennett A., Rawlings J. M. C., Brown P. D., Charnley S. B., 1991, A&AS, 87, 585

Millar T. J., Farquhar P. R. A., Willacy K., 1997, A&AS, 121

Mumma M. J., Disanti M. A., dello Russo N., Fomenkova M., Magee-Sauer K., Kaminski C. D., Xie D. X., 1996, Science, 272, 1310

Noble J. A., Congiu E., Dulieu F., Fraser H. J., 2012, MNRAS, 421, 768

Öberg K. I., Boogert A. C. A., Pontoppidan K. M., Blake G. A., Evans N. J., Lahuis F., van Dishoeck E. F., 2008, ApJ, 678, 1032

Öberg K. I., Boogert A. C. A., Pontoppidan K. M., van den Broek S., van Dishoeck E. F., Bottinelli S., Blake G. A., Evans, II N. J., 2011, ApJ, 740, 109

Öberg K. I., Linnartz H., Visser R., van Dishoeck E. F., 2009, ApJ, 693, 1209

Öberg K. I., van Dishoeck E. F., Linnartz H., 2009, A&A, 496, 281

Oliveira J. M. et al., 2009, ApJ, 707, 1269

Oliveira J. M. et al., 2011, MNRAS, 411, L36

Oliveira J. M. et al., 2013, MNRAS, 428, 3001

Pauly T., Garrod R. T., 2016, ApJ, 817, 146

Peimbert A., 2003, ApJ, 584, 735

Pietrzyński G. et al., 2013, Nature, 495, 76

Pradhan A. C., Murthy J., Pathak A., 2011, ApJ, 743, 80

Roman-Duval J. et al., 2014, ApJ, 797, 86

Ruffle D. P., Herbst E., 2000, MNRAS, 319, 837

Russell S. C., Dopita M. A., 1992, ApJ, 384, 508

Sandford S. A., Allamandola L. J., 1988, Icarus, 76, 201

Schilke P., Groesbeck T. D., Blake G. A., Phillips, T. G., 1997, ApJS, 108, 301

Seale J. P., Looney L. W., Chu Y.-H., Gruendl R. A., Brandl B., Chen C.-H. R., Brandner W., Blake G. A., 2009, ApJ, 699, 150

Shimonishi T., Dartois E., Onaka T., Boulanger F., 2016a, A&A, 585, A107

Shimonishi T., Onaka T., Kato D., Sakon I., Ita Y., Kawamura A., Kaneda H., 2008, ApJL, 686, L99

Shimonishi T., Onaka T., Kato D., Sakon I., Ita Y., Kawamura A., Kaneda H., 2010, A&A, 514, A12

Shimonishi T., Onaka T., Kawamura A., Aikawa Y., 2016b, ApJ, 827, 72

Spitzer L., 1978, Physical processes in the interstellar medium

Tielens A. G. G. M., Hagen W., 1982, A&A, 114, 245

van Loon J. T., Oliveira J. M., Gordon K. D., Sloan G. C., Engelbracht C. W., 2010, AJ, 139, 1553

van Loon J. T. et al., 2005, MNRAS, 364, L71

Vangioni-Flam E., Lequeux J., Maucherat-Joubert M., Rocca-Volmerange B., 1980, A&A, 90, 73

Vasyunin A. I., Semenov D. A., Wiebe D. S., Henning T., 2009, ApJ, 691, 1459

Venemans B. et al., 2017, ArXiv e-prints

Wakelam V. et al., 2010, **??**jnlSpace Sci. Rev., 156, 13

Watanabe N., Kouchi A., 2002, ApJL, 571, L173

Watanabe N., Nagaoka A., Shiraki T., Kouchi A., 2004, ApJ, 616, 638

Watanabe N., Shiraki T., Kouchi A., 2003, ApJL, 588, L121

Watson W. D., Salpeter E. E., 1972, ApJ, 174, 321

Weingartner J. C., Draine B. T., 2001, ApJ, 563, 842

Whitney B. A. et al., 2008, AJ, 136, 18

Whittet D. C. B., Adamson A. J., Duley W. W., Geballe T. R., McFadzean A. D., 1989, MNRAS, 241, 707

Whittet D. C. B., Cook A. M., Chiar J. E., Pendleton Y. J., Shenoy S. S., Gerakines P. A., 2009, ApJ, 695, 94

Whittet D. C. B., Cook A. M., Herbst E., Chiar J. E., Shenoy S. S., 2011, ApJ, 742, 28

Whittet D. C. B., Shenoy S. S., Bergin E. A., Chiar J. E., Gerakines P. A., Gibb E. L., Melnick G. J., Neufeld D. A., 2007, ApJ, 655, 332

Willis E. R., Garrod R. T., 2017, ApJ, 840, 61

Wright E. L. et al., 2010, AJ, 140, 1868

Zucconi A., Walmsley C. M., Galli D., 2001, A&A, 376, 650